Unravelling the role of the chain tilt angle for the macroscopic mechanical material properties of alpha isotactic polypropylene using a multiscale finite element model

van Gurp, Maikel J.A.C.

Award date:
2021

Department of Mechanical Engineering
Mechanics of Materials

Master thesis

Unravelling the role of the chain tilt angle for the macroscopic mechanical material properties of alpha isotactic polypropylene using a multiscale finite element model

---

Maikel van Gurp
1395823
m.j.a.c.v.gurp@student.tue.nl

Supervisors:
dr.ir. J.A.W. van Dommelen
ir. H.N. Chávez Thielemann

Second version

Breda, October 5, 2021

Nomenclature

Abbreviations

RVE	Representative volume element
CIM	Composite inclusion model
EGP	Eindhoven Glassy Polymer
FEM	Finite element model
FE^2	Finite element squared
FP	Fold plane
iPP	Isotactic polypropylene
PBC	Periodic boundary conditions
PE	Polyethylene
PET	Polyethylene terephthalate

Superscripts

a	Amorphous
Ba	Back
Bo	Bottom
c	Crystalline
F	Front
i	Inclusion
L	Left
R	Right
T	Top

Operations

$(\bullet)(\bullet)$	Dyadic product
$(\bullet) \cdot (\bullet)$	Dot product
$(\bullet) : (\bullet)$	Double dot product
$(\underset{\sim}{\bullet})$	Column assembly of a quantity
$(\underline{\bullet})$	Matrix assembly of a quantity
$(\bullet)^{-1}$	Inverse of a matrix or tensor
$(\bullet)^{T}$	Transpose of a matrix, vector or tensor
$(\bullet)^{RT}$	Right transpose of a 4th-order tensor
$(\bullet)^{S}$	Symmetrization of a tensor defined as $\frac{1}{2}[(\bullet) + (\bullet)^T]$

Symbols

A	Surface	$[\mathrm{mm}^2]$
$^4\boldsymbol{C}$	Stiffness tensor	[MPa]

$\underline{C}_{crystal}$	6×6 Stiffness matrix for the crystalline phase	[MPa]
$\underline{C}_{mat}$	6×6 Stiffness matrix	[MPa]
$\underset{\sim}{C}$	Column containing stiffness components	[MPa]
c	Corner node	[-]
$\boldsymbol{E}$	Green-Lagrange strain tensor	[-]
E	Young's modulus	[MPa]
$\boldsymbol{F}$	Deformation gradient tensor	[-]
F	Force	[N]
$\vec{f}$	Reaction force vector	[N]
f_0	Initial volume fraction	[-]
f	Volume fraction	[-]
G	Shear modulus	[MPa]
G_{ij}	Components of matrix that contains derivatives of eigenvalues of $\boldsymbol{U}$	[-]
H	Hardening factor	[-]
$^4\boldsymbol{I}$	Fourth order identity tensor	[-]
$^4\boldsymbol{I}^{RT}$	Fourth order right transposed identity tensor	[-]
$^4\boldsymbol{I}^{S}$	Fourth order symmetrical identity tensor	[-]
$\boldsymbol{I}$	Identity tensor	[-]
$\underline{I}$	Identity matrix	[-]
$\vec{i}$	Displacement direction	[-]
J	Determinant of the deformation gradient tensor	[-]
$^4\boldsymbol{K}$	Material tangent stiffness	[MPa]
$\underline{K}$	Jacobian matrix	[-]
K	Bulk modulus	[MPa]
k	Node number	[-]
$\boldsymbol{L}_p$	Plastic velocity gradient tensor	$[\frac{1}{\mathrm{s}}]$
$\underline{M}_o$	Matrix of orientations	[°]
M	Number of simple eigenvalues	[-]
m	Fitting parameter	[-]
N_S	Number of distinct slip systems	[-]
$\vec{n}$	Normal vector	[-]
$\boldsymbol{P}_0$	Schmid tensor in reference configuration	[-]
$\bar{\boldsymbol{P}}^{\mu\mathrm{RVE}}$	Volume averaged first Piola-Kirchhoff stress tensor	[MPa]
P	Schmid factor	[-]
p	Pressure	[MPa]

q	Equivalent plastic strain	[-]
R	Universal gas constant	$[\frac{\mathrm{J}}{\mathrm{K\ mol}}]$
r	Residual	[-]
$^4\boldsymbol{S}$	Compliance tensor	$[\frac{1}{\mathrm{MPa}}]$
$\boldsymbol{S}$	Second Piola-Kirchhoff stress tensor	[MPa]
$S^{'}$	Thermodynamic state	[-]
$\underline{S}_{mat}$	6×6 Compliance matrix	$[\frac{1}{\mathrm{MPa}}]$
s	Slip resistance (including hardening effects)	[MPa]
s_e	Number of unique eigenvalues	[-]
T	Temperature	[K]
T_r	Reference temperature	[K]
$\boldsymbol{U}$	Right stretch tensor	[-]
U	Activation energy	[J]
$\vec{u}$	Displacement vector	[mm]
V_0	Initial volume	[mm^3]
$\vec{x}^0$	Initial coordinates vector of a material point	[mm]
$\vec{x}_0$	Vector that lays in the interface	[-]
α	Slip system identifier	[-]
β	Angle between loading direction and slip direction	[°]
$\dot{\gamma}$	Slip rate	$[\frac{1}{\mathrm{s}}]$
$\dot{\gamma}_0$	Initial slip rate	$[\frac{1}{\mathrm{s}}]$
Δt	Time step	[s]
$\Delta\gamma$	Slip increment	[-]
δ	Symbol to imply the variational form	[-]
δ_{1M}	Dirac delta	[-]
$\underset{\sim}{\varepsilon}$	Matrix containing Green-Lagrange strain components	[-]
$\bar{\varepsilon}_{11}$	Global applied engineering strain in the spherulite model	[-]
ε_{eng}	Engineering strain	[-]
ε_i^{GL}	Green-Lagrange strain tensor component	[-]
ε_n^a	Interlamellar separation	[-]
ε_{sh}^a	Interlamellar shear	[-]
ε_{vm}^c	Intralamellar deformation (equivalent von Mises strain)	[-]
η	Viscosity	[MPa s]
$\boldsymbol{\Lambda}$	Logarithmic strain tensor	[-]
λ	Eigenvalue	[-]

μ	Pressure coefficient	[MPa]
ν	Poisson ratio	[-]
$\boldsymbol{\sigma}$	Cauchy stress tensor	[MPa]
σ	Cauchy stress component	[MPa]
τ	Resolved shear stress	[MPa]
τ_0	Slip resistance (constant value)	[MPa]
τ_{back}	Resolved back stress	[MPa]
τ_{eff}	Effective resolved shear stress	[MPa]
τ_k	Equivalent deviatoric stress in process k	[MPa]

Abstract

Semi-crystalline polymers are used in various applications. The mechanical response of a semi-crystalline polymer is strongly influenced by its microstructure. This emphasises the need of a model that can predict the mechanical response of a semi-crystalline polymer based on its microstructure. For this purpose a composite inclusion model is being developed for alpha isotactic polypropylene, which has been successfully developed for polyethylene in the past. An important difference between polyethylene and polypropylene is the chain tilt angle. The chain tilt angle has an important but not well-understood influence on the macroscopic mechanical material properties.

The aim of this project is to unravel the role of the chain tilt angle for the macroscopic mechanical material properties of alpha isotactic polypropylene using a multiscale finite element model and to validate the modelling framework of the composite inclusion model. First, the influence of the chain tilt angle on macroscopic mechanical material properties is investigated using the multiscale finite element model. After that, the obtained results are used to validate the modelling framework of the composite inclusion model.

It can be concluded that the chain tilt angle has a small influence on the Young's modulus and microscopic elastic deformation. It is shown that the microscopic elastic deformation observed in the multiscale FEM is in reasonably good agreement with the composite inclusion model, following similar trends, but presenting differences related to the used geometries. The Young's moduli predicted by the multiscale FEM and composite inclusion model are in good agreement. It is also shown that the chain tilt angle has a noticeable effect on the activation of slip systems.

Contents

1 Introduction

Semi-crystalline polymers are used in various high-tech applications. Because of this it is important to understand their mechanical behavior. The macroscopic material properties of a semi-crystalline polymer are strongly influenced by its microstructure. The microstructure consists of several structural features such as crystal type, size, orientation and crystallinity. These structural features influence both the mechanical properties and texture evolution of the microstructure. This emphasises the need for a model that is able to describe micro-structural development (i.e. texture evolution) and to describe macroscopic material behavior based on the microstructure. To create such a model, it is important to understand the characteristics of a semi-crystalline polymer at different scales.

1.1 Microstructure of semi-crystalline polymers

Important structures of a semi-crystalline polymer can be distinguished at a mesoscopic scale and a microscopic scale. The mesoscopic scale lays in between the microscopic and macroscopic scales.

1.1.1 Structure at mesoscopic scale

After cooling from a melt, at certain points, which are called nuclei, crystallization starts. From these nuclei, crystalline lamellae start growing. Lamellae in a solidified melt can be arranged into three different structures depending on the flow. With (almost) no flow, lamellae will be arranged in the radial direction, forming spherulites. With flow they would become aligned resulting in a row structure. As flow keeps increasing, at a certain point, they will be arranged in a so called shish-kebab structure. The spherulitic structure is generally found in e.g. polyethylene terephthalate (PET) and isotactic polypropylene (iPP) [1].

When the crystallization process starts, there is unconstrained amorphous material between all spherulites. At this moment, spherulites do not touch each other and therefore have a spherical shape. As they keep growing, the unconstrained amorphous material between them vanishes and the boundaries of the spherulites start touching each other. Because of this, they become polyhedron shaped which can be observed at the mesoscopic scale, as shown in Figure 1.1, where the thick white lines are interfaces between the spherulites [2].

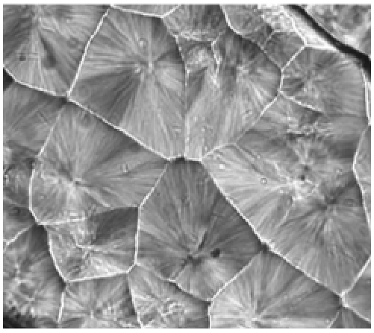

Figure 1.1: Spherulitic structure as observed on the mesoscopic scale, where interfaces between spherulites are identified by the thick white lines [2].

1.1.2 Structure at microscopic scale

By zooming in on the spherulite, the microstructure is observed, which consists of crystalline lamellae and amorphous material, as schematically shown in Figure 1.2a. Amorphous molecular chains have a random orientation, as schematically shown in Figure 1.2b. Therefore, the amorphous material behavior is isotropic. Crystalline molecular chains are strongly oriented, as schematically shown in Figure 1.2c. Therefore, the crystalline material behavior is strongly anisotropic. There is an interface (also called the fold plane) in between the two materials through which the two materials interact with each other. The molecular chains in the crystalline material are tilted at a certain angle with respect to the fold plane normal, which is called the chain tilt angle. In α-iPP this angle is approximately 0°, whereas in PET this angle is approximately 25° and in PE it is 35°.

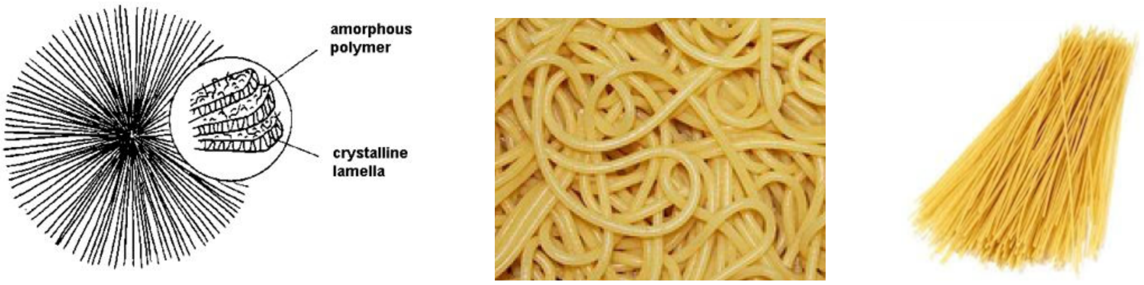

(a) (b) (c)

Figure 1.2: (a) A spherulite in which amorphous material and crystalline lamellae are shown [3]. A schematic analog of the molecular chain orientation in (b) the amorphous material and (c) the crystalline lamellae.

The macroscopic behavior of a semi-crystalline polymer strongly depends on the microstructure, i.e. the material behavior of the crystalline lamellae, amorphous material and the interactions between them, where the chain tilt angle possibly plays an important role on the interactions. Also, texture evolution of the microstructure strongly influences the macroscopic behavior of a semi-crystalline polymer.

1.2 Models to predict macroscopic behavior based on microstructure

Many models have been developed to predict texture evolution of semi-crystalline polymers. To do this, Parks et al. [4] and Lee et al.[5] developed Taylor-type models to predict the viscoplastic behavior. Dahoun et al. [6] used a self-consistent viscoplastic approach to predict texture evolution. In these studies, the amorphous phase was neglected, which physically has an important role.

1.2.1 Composite inclusion model

To take the amorphous material into account, Lee et al. [7, 8] introduced the composite inclusion model in 1993. This model only described viscoplastic material behavior. To describe the elasto-viscoplastic material behavior, van Dommelen et al. [9] extended the composite inclusion model of Lee et al. Here, the behavior of a material point was described by a composite inclusion as shown in Figure 1.3a. An aggregate of composite inclusions (Figure 1.3b) was used to describe the material behavior of the microstructure.

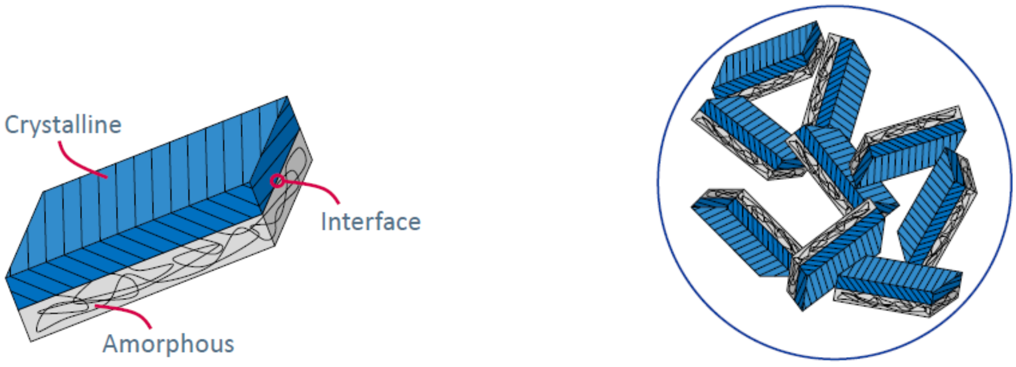

(a) (b)

Figure 1.3: (a) Composite inclusion and (b) an aggregate of composite inclusions [10].

The crystalline lamellae were modelled as anisotropic elastic with plastic deformation occurring through crystallographic slip. The amorphous material was isotropic elasto-viscoplastic where strain hardening was taken into account as well.

To describe macroscopic material behavior based on the aggregate of composite inclusions (which represents the microstructure), local-global interaction laws were created. In these interaction laws, each composite inclusion is represented as a spring. A popular interaction law is the Taylor interaction model [11, 12, 13]. In a Taylor interaction model, all springs are placed parallel to each other, as schematically shown in Figure 1.4a. The behavior of all springs (composite inclusions) together is then considered to be the macroscopic material behavior. So, the local strain equals the global strain. Because of this, these models may lead to unreasonably high stresses due to the anisotropy of the crystalline lamellae. So, a Taylor model satisfies the inter-inclusion compatibility, but not the traction equilibrium.

To solve this issue, another interaction law was developed, the Sachs interaction model [14, 7]. In a Sachs model, springs are placed in series as schematically shown in Figure 1.4b. In this case, the local stress equals the global stress. However, in this model, the inter-inclusion compatibility is not satisfied. The Taylor model predicts an upper bound of the stress, where the Sachs models predicts a lower bound of the stress. Due to the strong anisotropy of crystalline lamellae, the difference between the prediction of the Taylor and Sachs models is large. Therefore, both these models will predict results quite far from reality.

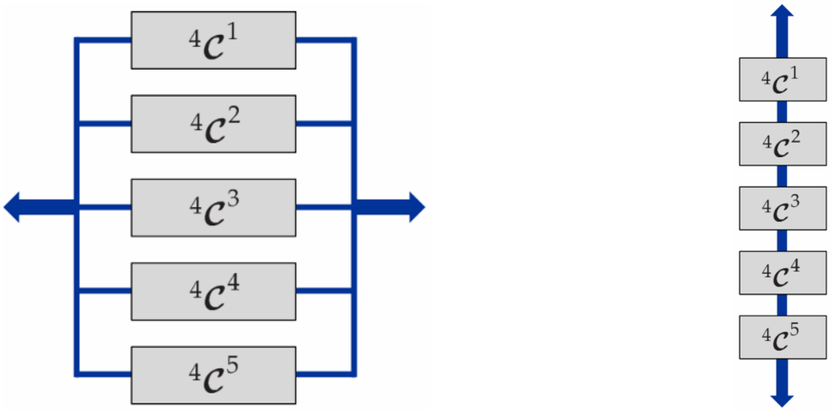

(a) (b)

Figure 1.4: Schematic representation of the local-global (a) Taylor and (b) Sachs interaction laws [15].

Van Dommelen et al. [9] proved that the use of a Taylor/Sachs hybrid interaction law results in physically more realistic predictions as with a Taylor or Sachs interaction law, and therefore used such an interaction law in their model. Van Dommelen et al. [9] showed that with increasing crystallinity, both the initial stiffness and yield stress increase, whereas the post-yield hardening on the other hand is approximately independent of crystallinity. They also observed that when low crystallinities were used, a more Sachs-like interaction law should be used. This is because at low crystallinities the amorphous material, with the lowest stiffness, starts to contribute the most to the material response.

1.2.2 Finite element model

Over time the computing power has increased significantly. Therefore finite element models (FEM) are getting more and more popular. The advantage of FEM with respect to the mean-field method, is that the microstructure can be described in detail.

Van Dommelen et al. [16] created a full-field finite element model of the spherulitic structure, of which the material behavior was described by the mean-field composite inclusion model. Based on this concept, Poluektov et al. [17] developed a two-scale finite-element model. Here, the material behavior of a material point in the spherulite model was represented by another FEM, in the form of a representative volume element (RVE) of the microstructure, using periodic boundary conditions (PBC). The micro RVE was created such that the global material behavior was transversely isotropic. In the spherulite model, Poluektov only used cubic and bcc stacking as shown in Figure 1.5, because it was proven that the irregularity of the stacking is not important [16].

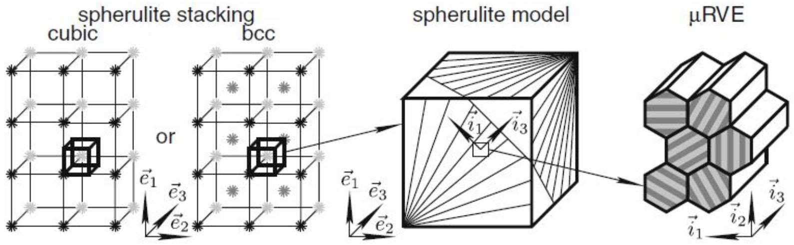

Figure 1.5: Two-level finite element modelling scheme [17].

Poluektov et al. created a link between the two scales by gathering the effective elastic material properties from the micro RVE and used these in each material point of the spherulite model, considering their orientation with respect to their spherulitic center. The obtained effective elastic material properties in the spherulite model were then directly used to solve the macroscopic problem.

Poluektov et al. used the multi-scale finite element model to investigate the behavior of isotropic PET and then validated the modelling framework of the composite inclusion model of van Dommelen et al. [9] for PET with it. It was shown that the prediction on microstructural deformation was similar for both models. It was also shown that changing the aspect ratio of the crystalline lamellae at high crystallinity, almost has no effect on the macroscopic behavior.

1.3 Material models

The multi-scale finite element model created by Poluektov et al. uses elastic material models implemented in MSC Marc 2008. To get more accurate results and enable plasticity simulations, more complex material models are required.

Material model for crystalline phase: To describe the material behavior of the crystalline phase, a crystal plasticity model (CPM) was numerically implemented in the nonlinear finite elements analysis software MSC Marc 2014 by van Nuland and Oude Vrielink [18]. In this model, the elastic material behavior was described by Hooke's law. The plastic material behavior was described by crystallographic slip, taking all physically distinct slip systems into account.

Material model for amorphous phase: Govaert et al. developed a model to describe the behavior of glassy polymers, which is called the Eindhoven Glassy Polymer (EGP) model [19], which is implemented in MSC Marc 2013. This model can be used to accurately describe the material behavior of a polymeric amorphous phase. Their model has a long history of extensions and improvements such as: implementation of relaxation times, strain softening, strain hardening, pressure dependent viscosity and dependence of viscosity on the thermomechanical state. Over time, the modelling of thermo-rheologically complex materials, thermomechanical history and loading-unloading were enabled.

In the EGP-model, deformation behavior is described by inter-molecular interactions and the molecular network in parallel. The inter-molecular interactions are described by a Maxwell element. The molecular network is described by a single spring as shown in Figure 1.6.

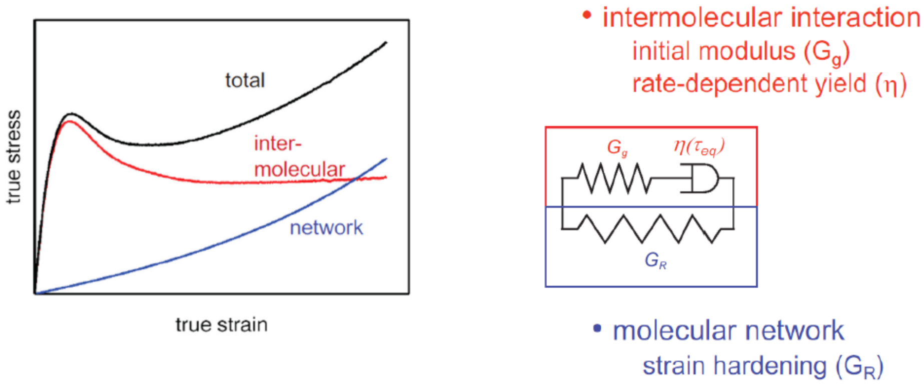

Figure 1.6: The deformation behavior description in the EGP-model schematically shown [20].

1.4 Problem definition

The composite inclusion model is more user-friendly and less time consuming in simulations compared to the multi-scale finite element model. Therefore, it is desired to develop a composite inclusion model that can predict macroscopic material properties based on the microstructure, rather than the multi-scale finite element model. In the past, the composite inclusion model has been successfully developed for PET. Currently it is being developed for α-iPP. A key difference between α-iPP and other semi-crystalline polymers (e.g. PET) is the chain tilt angle, which is approximately 0° for α-iPP. The chain tilt angle has an important but not well understood effect on the macroscopic mechanical material properties of a semi-crystalline polymer such as Young's modulus, Poisson ratio and yield stress (i.e. activation of slip systems), and on the crystalline-amorphous interactions.

The main goal in this thesis is to investigate the influence of the chain tilt angle on macroscopic mechanical material properties of α-iPP using a multi-scale finite element model and use it to validate the modelling framework of the composite inclusion model.

1.5 This thesis

In this thesis, the influence of the chain tilt angle on macroscopic mechanical material properties of α-iPP is studied. In Chapter 2, the composite inclusion model is explained briefly and the multi-scale finite element model [17], which is used to investigate the influence of the chain tilt angle is explained more elaborate. Next, in Chapter 3, the simulation results for elastic macroscopic mechanical material properties of α-iPP are discussed. In Chapter 4 the adjustments made to the multi-scale finite element model to enable elasto-viscoplastic simulations are discussed. Also, the elasto-viscoplastic simulations to obtain the macroscopic mechanical material properties of α-iPP and the results are discussed in this chapter. In Chapter 5, the conclusions and recommendations can be found.

2 Micromechanical simulation models

In this chapter, first, the composite inclusion model is explained. Next, the multi-scale finite element model used to unravel the role of the chain tilt angle on macroscopic mechanical material properties and to validate the composite inclusion model is explained. Also, the used simulations parameters are given in this chapter.

2.1 Introduction

The model that is used in this project is a full-field numerical model [17]. This model was used to describe the material behavior of PET in a previous project. It models microscopic material behavior of a bundle of crystalline lamellae with a representative volume element (RVE) of the microstructure. Effective elastic material properties are then extracted from this micro RVE and used to model the material behavior of a spherulite model (which represents the mesoscopic material behavior). Next, the effective elastic properties of the spherulite model are obtained which equal the macroscopic effective elastic properties. Finally, deformations are applied to the micro RVE based on the microstructural deformation as observed in the spherulite model. Based on these deformations, pole figures are used to investigate the microstructural deformation. The multi-scale finite element model is only suitable for elastic simulations, i.e. all used material models are purely elastic. During this project, results obtained with the multi-scale finite element model are compared to results obtained with the composite inclusion model, which is explained briefly first.

2.2 Composite inclusion model

In this section, the composite inclusion model [21], to which results obtained with the multi-scale finite element model will be compared, is explained briefly. In this project, the composite inclusion model is not used to perform simulations. Figure 2.1a shows a single composite inclusion, which is used to model microstructural material behavior. Figure 2.1b shows an aggregate of composite inclusions, which is used to model macroscopic material behavior.

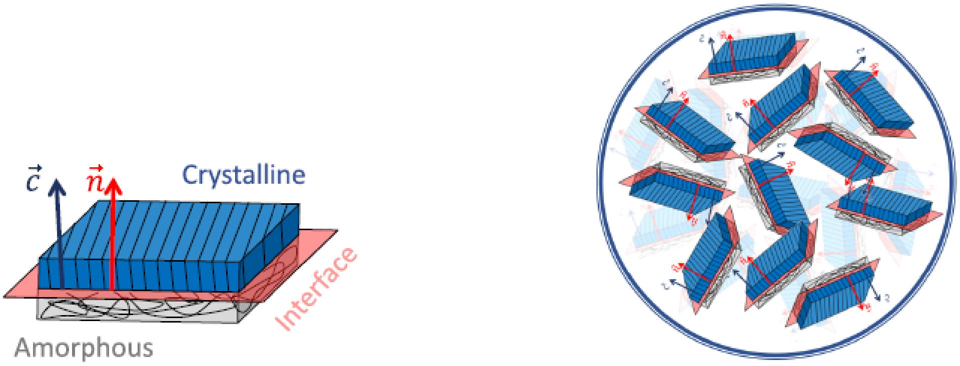

(a) (b)

Figure 2.1: (a) Single composite inclusion with, crystalline and amorphous material, an interface, $\vec{n}$ a vector normal to the interface and $\vec{c}$ the crystalline chain direction. (b) An aggregate of composite inclusions to represent the macroscopic material behavior [21].

2.2.1 Single composite inclusion

A single composite inclusion consists of both an crystalline and amorphous volume fraction:

$$1 = f_0^a + f_0^c, \tag{2.1}$$

where f_0^a and f_0^c are the amorphous and crystalline initial volume fractions respectively. Taking (initial) volume fractions into account, the deformation gradient tensor and Cauchy stresses in each inclusion i are calculated:

$$\boldsymbol{F}^i = f_0^a \boldsymbol{F}^a + f_0^c \boldsymbol{F}^c, \tag{2.2}$$

$$\boldsymbol{\sigma}^i = f^a \boldsymbol{\sigma}^a + f^c \boldsymbol{\sigma}^c, \tag{2.3}$$

where f^a and f^c are the amorphous and crystalline volume fractions respectively, $\boldsymbol{F}$ the deformation gradient tensor and $\boldsymbol{\sigma}$ the Cauchy stress tensor. The two materials are mechanically coupled by two conditions. The first condition is:

$$\boldsymbol{F}^i \cdot \vec{x}_0^i = \boldsymbol{F}^a \cdot \vec{x}_0^i + \boldsymbol{F}^c \cdot \vec{x}_0^i, \tag{2.4}$$

where $\vec{x}_0^i$ is a vector that lays in the interface shown in Figure 2.1a. The second condition is:

$$\boldsymbol{\sigma}^i \cdot \vec{n} = \boldsymbol{\sigma}^a \cdot \vec{n} + \boldsymbol{\sigma}^c \cdot \vec{n}, \tag{2.5}$$

where $\vec{n}$ is the vector normal to the interface as shown in Figure 2.1a.

2.2.2 Amorphous phase

To capture the isotropic elasto-viscoplastic behavior of the amorphous phase, the so-called Eindhoven Glassy Polymer (EGP) model is used. Throughout this report, if the EGP-model is discussed for the multi-scale finite element model, a version of the EGP-model, implemented in MSC Marc is meant. The composite inclusion model makes use of a different EGP-model, one that is not implemented in MSC Marc, but which is fully operational in Matlab 2020.

In the EGP-model, implemented in the composite inclusion model, the amorphous phase is described as schematically shown in Figure 2.2. The stress-strain behavior is captured by strain hardening (G_r), j modes, indicated in green and k processes, indicated in red. A mode is a Maxwell element, which compared to other modes, that belong to the same process, has a different shear modulus and/or relaxation time, but has the same dependence on stress, temperature, pressure and thermal history. A process is a group of modes, where the stress, temperature, pressure and thermal history dependencies differ compared to other processes.

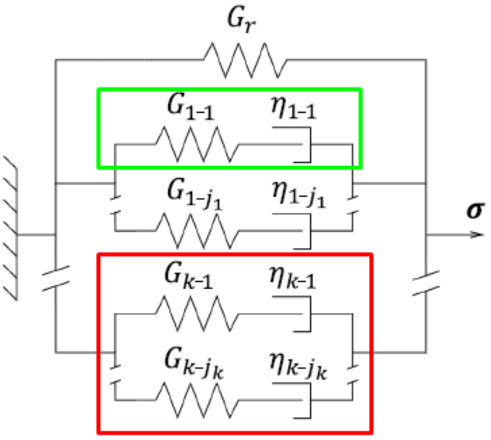

Figure 2.2: Schematic representation of the multi-process, multi-mode EGP-model analog [21].

In each mode j of process k, the viscosity is described by a non-linear relation, depending on the equivalent deviatoric stress τ_k, temperature T, pressure p and thermodynamic state $S_k^{'}$:

$$\eta_{kj} = \eta_{0k,j} \frac{\tau_k/\tau_{0k}}{\sinh\left(\tau_k/\tau_{0k}\right)} \exp\left(\frac{\Delta U_k}{R}\left(\frac{1}{T}-\frac{1}{T_r}\right)\right) \exp\left(\frac{\mu_k p}{\tau_{0k}}\right) \exp\left(S_k^{'}\right), \tag{2.6}$$

where $\eta_{0k,j}$ is the viscosity in the rejuvenated reference state, ΔU_k the activation energy, R the universal gas constant, T_r the reference temperature and μ_k a pressure coefficient. For more information on the non-linear viscosity, see [21].

2.2.3 Crystalline phase

The crystalline structure in semi-crystalline polymers is a stacking of chains with a certain order and repetition. Therefore, the crystalline phase is strongly anisotropic. To capture this material behavior, an anisotropic elasto-viscoplastic material model is used. The elastic part is described by the elastic Cauchy stress tensor, obtained as:

$$\boldsymbol{\sigma}_e = J_e^{-1}\left(\boldsymbol{F}_e \cdot \boldsymbol{S}_e \cdot \boldsymbol{F}_e^T\right), \qquad \text{with} \qquad \boldsymbol{S}_e = {}^4\boldsymbol{C} : \boldsymbol{E}_e, \tag{2.7}$$

where $\boldsymbol{F}_e$ is the elastic deformation gradient tensor, J_e the determinant of $\boldsymbol{F}_e$, $\boldsymbol{S}_e$ the second Piola-Kirchhoff stress tensor, ${}^4\boldsymbol{C}$ the stiffness tensor and $\boldsymbol{E}_e$ the elastic Green-Lagrange strain tensor. For more details, see [21]. The plastic deformation is captured by a viscoplastic rate-dependent model. It can capture fine slip, which is predominant at the initial stages of deformation [22] and is defined as:

$$\boldsymbol{L}_p = \dot{\boldsymbol{F}}_p \cdot \boldsymbol{F}_p^{-1} = \sum_{\pi=1}^{N_s} \dot{\gamma}^\pi \boldsymbol{P}_0^\pi, \qquad \text{with} \qquad \boldsymbol{P}_0^\pi = \vec{s}_0^{\,\pi} \vec{n}_0^{\,\pi}, \tag{2.8}$$

where $\boldsymbol{L}_p$ is the plastic velocity gradient tensor, $\boldsymbol{F}_p$ the plastic velocity gradient tensor, $\dot{\gamma}^\pi$ the slip rate on slip system π, $\boldsymbol{P}_0^\pi$ the Schmid tensor, $\vec{s}_0^{\,\pi}$ the slip direction and $\vec{n}_0^{\,\pi}$ the vector normal to the slip system. For more details see [21].

2.2.4 Hybrid interaction law

At this point, one inclusion and its material behavior is defined. To represent the macroscopic material behavior, an aggregate of inclusions, of which an example is shown in Figure 2.1b, is required. A hybrid interaction law, called the $\hat{\boldsymbol{U}}$-inclusion model [9] is used, which is a combination of the Taylor [11, 12, 13] and Sachs [14, 7] interaction laws. This interaction law is basically a set of equations, which guarantees local-global compatibility. In the $\hat{\boldsymbol{U}}$-inclusion model, six auxiliary deformation-like unknowns are introduced. Then, a Sachs-like interaction law is used. Finally, also the inclusion-averaged rotations are prescribed. For more details see [9].

2.3 RVE of the microstructure

In this section, everything related to the micro RVE, which is used in the multi-scale finite element model is discussed.

2.3.1 Hexagonal domains

The micro RVE is built with hexagonal domains consisting of amorphous material and crystalline lamellae, for example as shown in Figure 2.3a. During this project, crystallinities of 50%, 60% and 70% are used. The hexagonal domains constructed for each crystallinity are shown in Figure 2.3a, 2.3b and 2.3c respectively. Furmanski et al. [23] proved that the yield kinetics of PE do not depend on crystal thickness. Eight-node isoparametric arbitrary hexahedral elements are predominantly used and six-node isoparametric arbitrary pentahedral elements are used only on some non-horizontal boundaries of the hexagonal domains. Both element types use full integration. Along each boundary, 20 mesh elements are present. The width and height of the hexagonal domains are set to 0.2 mm and 0.1732 mm respectively. The thickness of a hexagonal domain is set to 0.01 mm, which is equal to the thickness of two elements.

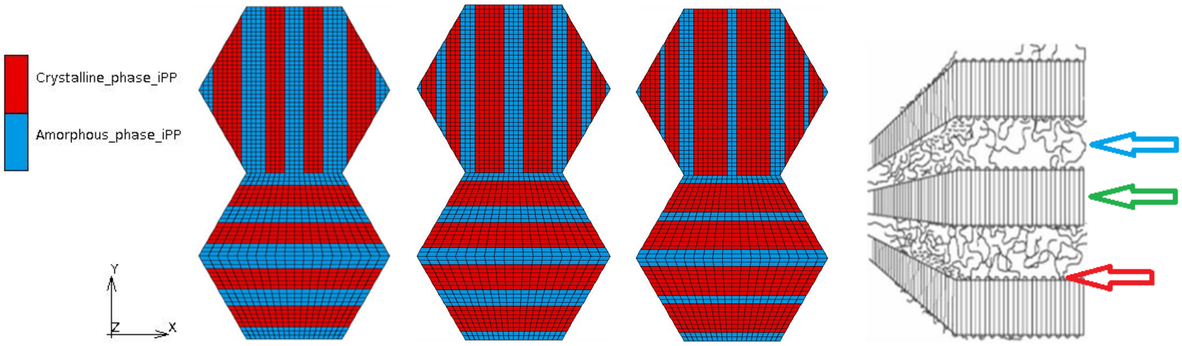

(a) (b) (c) (d)

Figure 2.3: Hexagonal domains used for a crystallinity of (a) 50%, (b) 60%, (c) 70% and (d) a schematic representation of a lamellae stack [24].

In these hexagonal domains, a perfect bond between the crystalline and amorphous material is assumed. This is not physically relevant as shown in Figure 2.3d. Here, the amorphous material is indicated by the blue arrow, crystalline material by the green arrow and the fold plane with the red arrow. It can be seen that at the fold plane, the crystalline chains fold back into the crystalline material. Amorphous molecular chains can go through these folds, making both phases interact with each other. For now, this is too complex to take into account in the mesh. Therefore, a perfect bond between the two phases is assumed in this project.

2.3.2 Material behavior

The amorphous material behavior is described by an elastic isotropic material model available in MSC Marc 2018. The used material properties for the amorphous phase are the same as the material parameters that are used in the composite inclusion model. A Poisson's ratio (ν) of 0.49 and Young's modulus of 575 MPa are used.

The crystalline material behavior is described by an elastic anisotropic material model available in MSC Marc 2018. Tashiro et al. [25] calculated the stiffness for the crystalline phase. They assumed the crystal phase to consist of ideal molecular chains only. In reality the crystalline phase always interacts with the amorphous phase, therefore the stiffness predicted in their work was an over prediction w.r.t. what is required in this project. Kamezawa et al. [26] used a composite model to describe interactions between the amorphous and crystalline phases. In this work, chain folds were not considered. Laschet et al. [2] took folded chains and packing density of the molecular chains into account. This led to the stiffness matrix at room temperature which is used in this project:

$$\underline{C}_{crystal} = \begin{bmatrix} 4340 & 1290 & 1320 & 0 & -120 & 0 \\ 1290 & 2810 & 1230 & 0 & 300 & 0 \\ 1320 & 1230 & 16460 & 0 & -190 & 0 \\ 0 & 0 & 0 & 1410 & 0 & -40 \\ -120 & 300 & -190 & 0 & 1460 & 0 \\ 0 & 0 & 0 & -40 & 0 & 1650 \end{bmatrix} \text{MPa.} \tag{2.9}$$

2.3.3 Crystal lattice

As can be seen, the crystalline phase is strongly anisotropic. Therefore, the orientation of the crystalline phase is important. The stiffness components are defined in a Cartesian coordinate system $\{\vec{e}_1^c, \vec{e}_2^c, \vec{e}_3^c\}$ as shown in Figure 2.4a, in which an example of a monoclinic lattice is shown. It is shown, that in the monoclinic lattice, $\vec{e}_2^c$ is parallel to b, $\vec{e}_3^c$ parallel to c and $\vec{e}_1^c$ is not parallel to a due to the angle β, which $\neq 90°$.

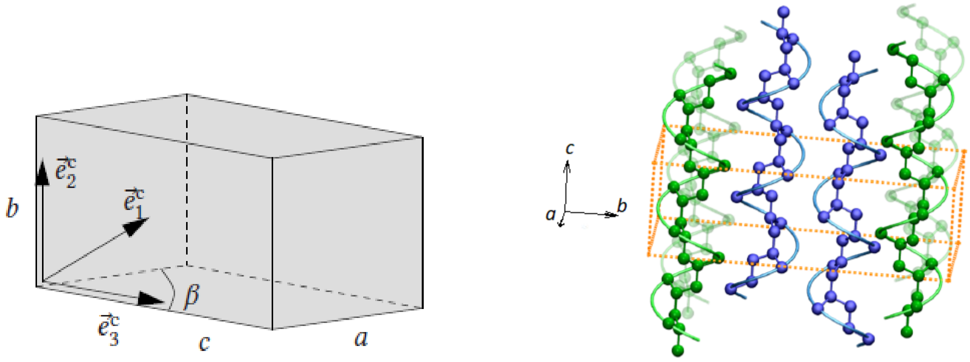

(a)

(b)

Figure 2.4: (a) A schematic representation of a monoclinic lattice in a Cartesian coordinate system $\{\vec{e}^{\,c}_1,\vec{e}^{\,c}_2,\vec{e}^{\,c}_3\}$ [15] and (b) the monoclinic lattice for α-iPP [21].

The monoclinic lattice parameters used during this project for α-iPP are: a = 6.65 nm, b = 20.96 nm, c = 6.50 nm, β = 99.2°, which are determined by Natta et al. [27], leading to the monoclinic lattice for α-iPP as shown in Figure 2.4b [21]. The chain direction, of the crystalline phase is parallel to c as shown in Figure 2.4b, so, the crystalline phase has the highest stiffness in the chain direction (see location (3,3) in Equation 2.9).

The fold planes investigated during this project are: $(10\bar{6})$, (010), (001) and $(1\,\bar{1}\,\bar{6})$. The $(10\bar{6})$ and (001) fold planes are close to each other and the $(10\bar{6})$ fold plane seems to be more physically relevant [28]. The (010) fold plane was observed by [29] based on experimental findings. The $(1\,\bar{1}\,\bar{6})$ fold plane is physically not relevant for alpha-iPP, but it is chosen purely for the investigation of the influence of the chain tilt angle. The fold planes are shown in the monoclinic lattice of α-iPP as shown in Figures 2.5a - 2.5d.

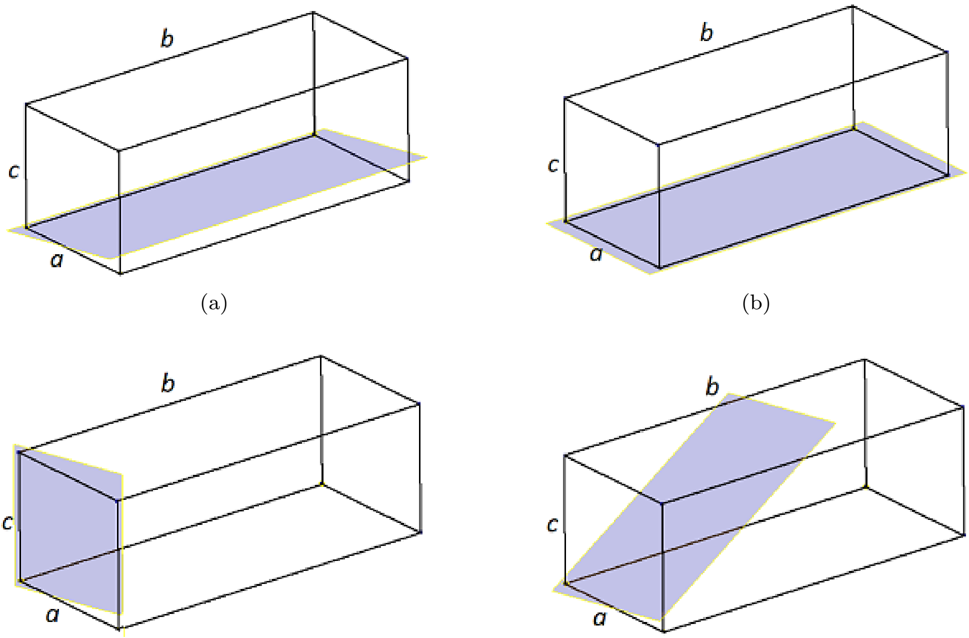

(a)

(b)

(c)

(d)

Figure 2.5: The monoclinic lattice for α-iPP, with the fold plane in blue. With (a) the $(10\bar{6})$ fold plane, (b) the (001) fold plane, (c) the (010) fold plane and (d) the $(1\,\bar{1}\,\bar{6})$ fold plane.

2.3.4 Chain tilt angle

Figure 2.6 schematically shows what a chain tilt angle is. Here, amorphous material is indicated in blue, crystalline material in red, the chain direction in yellow, the normal to the fold plane in grey, the fold plane in orange and alpha is the chain tilt angle.

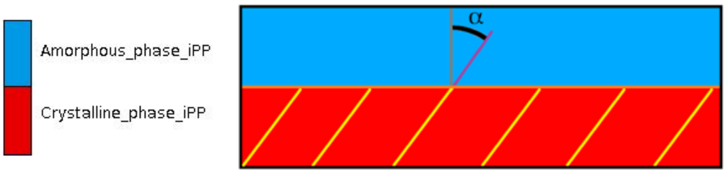

Figure 2.6: Schematic representation of the chain tilt angle in a 2D example. With amorphous material in blue, crystalline material in red, chain direction in yellow, the normal to the fold plane in grey, the fold plane in orange and alpha being the chain tilt angle.

By only defining the fold plane, there is no unique solution for the chain tilt angle. Therefore, the growth direction of the crystalline phase must be defined as well. For the $(10\bar{6})$ fold plane, the growth direction is the intersection between the fold plane and the monoclinic ac-plane [30]. The growth direction in other fold planes was not found in literature, therefore, it is assumed that in other fold planes, the growth direction also is the intersection between the fold plane and the monoclinic ac-plane. For example, for the (001) fold plane which is shown in Figure 2.5b, the growth direction is parallel to the monoclinic a-axis, since the fold plane lays in the monoclinic ab-plane. In the (010) fold plane, the growth direction can not be determined this way, because the ac-plane is the fold plane. Therefore, it is assumed that the growth direction is the same as for the $(10\bar{6})$ fold plane. Furthermore, the growth direction is parallel to the z-direction as shown in Figure 2.3a.

The chain tilt angles, investigated in this project, are shown in Table 1. This table also shows the fold plane, normal to the fold plane and crystal growth direction. The directions of the normal vector and crystal growth are defined in the Cartesian coordinate system $\{\vec{e}^{c}_1,\vec{e}^{c}_2,\vec{e}^{c}_3\}$ as shown in Figure 2.4a.

Table 1: Chain tilt angle, its corresponding fold plane, vector normal to the fold plane and crystal growth direction.

Chain tilt angle [°]	**Fold plane**	**Normal vector $\{\vec{e}^{c}_1,\vec{e}^{c}_2,\vec{e}^{c}_3\}$**	**Growth direction $\{\vec{e}^{c}_1,\vec{e}^{c}_2,\vec{e}^{c}_3\}$**
≈ 0	$(10\bar{6})$	[-0.0031 0 1]	[1 0 0.0031]
9.2	(001)	[0.162 0 1]	[1 0 -0.162]
90	(010)	[0 1 0]	[1 0 0.0031]
≈ 30	$(1\,\bar{1}1\,\bar{6})$	[-0.0031 0.577 1]	[1 0 0.0031]

To get a better understanding of these tilt angles, they are schematically shown in Figure 2.7. Here, crystalline material is shown in red, amorphous material in blue and the chain direction in yellow. The zy plane is the fold plane, thus, the chain tilt angle is the angle between the yellow lines and the x-axis (which is parallel to the normal of the fold plane). Every yellow line is in the xy-plane except for the (001) fold plane. Here the molecular chain direction is tilted 9.2° around the y-axis towards the z-axis. The growth direction is parallel to the z-axis.

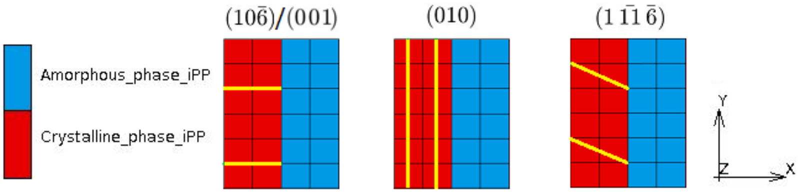

Figure 2.7: Schematic representation of the chain tilt angle, where crystalline material is shown in red, amorphous material in blue and the chain direction in yellow.

2.3.5 Micro RVE

The micro RVE consists of a $n \times n$ stacking of hexagonal domains. The top hexagonal domain is used for rotations of 0°, 60°, 120°, 180°, 240° and 300°, the bottom hexagonal domain is used for rotations of 30°, 90°, 150°, 210°, 270° and 330°. Poluektov et al. proved by a convergence study that a 6×6 stacking, of which an example is shown in Figure 2.8a, is sufficient to obtain transversely isotropic material behavior in the out-of-plane direction if the following three restrictions were applied:

1. Number of hexagonal domains with same orientations is uniform.
2. A hexagonal domain can not border another hexagonal domain with the same orientation.
3. The average position of hexagonal domains with the same orientation must be close to the center of the micro RVE.

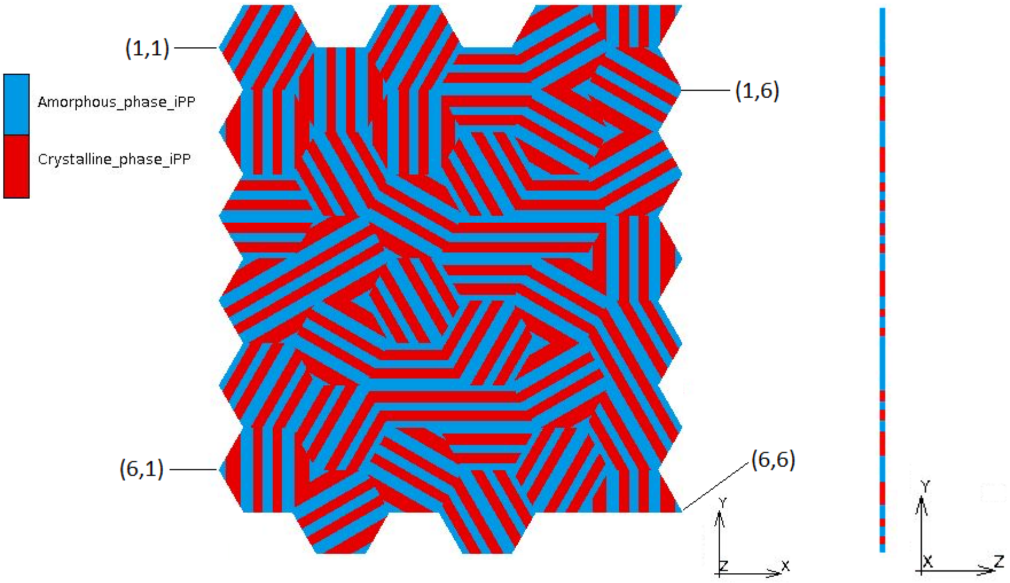

(a) (b)

Figure 2.8: Micro RVE with crystalline material in red and amorphous material in blue. (a) The front view and (b) the side view. The z-direction is parallel to the crystalline growth direction.

The mesh as for example shown in Figure 2.8a is made based on a matrix of orientations $\underline{M}_o$. Such a matrix describes the rotation of each hexagonal domain within the micro RVE. The matrix of orientations that belongs to the micro RVE shown in Figure 2.8a is:

$$\underline{M}_o = \begin{bmatrix} 150 & 0 & 330 & 90 & 300 & 240 \\ 180 & 210 & 180 & 30 & 60 & 120 \\ 270 & 300 & 240 & 90 & 270 & 0 \\ 120 & 60 & 30 & 150 & 240 & 30 \\ 330 & 150 & 90 & 270 & 300 & 210 \\ 0 & 120 & 60 & 210 & 330 & 180 \end{bmatrix} [^\circ]. \tag{2.10}$$

The orientations shown in the matrix at locations (1,1), (1,6), (6,1) and (6,6) are also indicated in Figure 2.8a. An orientation of 0° belongs to a hexagonal domain with crystal lamellae in the vertical direction, as shown in the top hexagonal domain in Figure 2.3a. The rotations shown in the matrix of orientations are defined counter clockwise. For each crystallinity (50%, 60% and 70%), five different matrices of orientations are used. So, in total 15 matrices are used, which are shown in Appendix A.

2.3.6 Periodic boundary conditions

The micro RVE is defined in a local coordinate system with the unit vectors $\vec{x}, \vec{y}, \vec{z}$. PBC are applied to the micro RVE to represent a larger microstructure. The PBC are explained according to Figure 2.9, where the geometry is described by four corner points c_j with $j = \overline{1,4}$. The following PBC are applied:

$$\vec{u}^R - \vec{u}^L = \vec{u}^{c_2} - \vec{u}^{c_1}, \tag{2.11}$$

$$\vec{u}^T - \vec{u}^{Bo} = \vec{u}^{c_3} - \vec{u}^{c_1}, \tag{2.12}$$

$$\vec{u}^F - \vec{u}^{Ba} = \vec{u}^{c_4} - \vec{u}^{c_1}, \tag{2.13}$$

where $\vec{u}$ is the displacement vector.

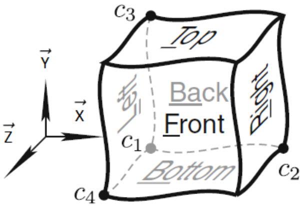

Figure 2.9: Schematic representation of corners (c_j for j = $\overline{1,4}$) that can move freely in a cubic volume when PBC are applied [17].

2.4 Obtaining material properties of the micro RVE

The effective elastic properties are obtained by deforming the micro RVE in six different ways using the nonlinear finite element analysis software MSC Marc 2018. Table 2 in combination with Figure 2.9 explains how the micro RVE is deformed, where corner node # denotes the corner number as shown in Figure 2.9.

Table 2: Applied micro RVE deformations where ε_{eng} is the engineering strain.

Deformation #	**corner node #**	**displacement direction**	**Displacement [mm]**
1	2	$\vec{x}$	$(c_2 - c_1)\varepsilon_{eng}$
2	3	$\vec{x}$	$(c_3 - c_1)\varepsilon_{eng}$
3	4	$\vec{x}$	$(c_4 - c_1)\varepsilon_{eng}$
4	3	$\vec{y}$	$(c_3 - c_1)\varepsilon_{eng}$
5	4	$\vec{y}$	$(c_4 - c_1)\varepsilon_{eng}$
6	4	$\vec{z}$	$(c_4 - c_1)\varepsilon_{eng}$

In every deformation, ε_{eng} is set to 0.01 [-]. Additionally, the nodes c_j that are not displaced are fixed in all three directions. The node that is displaced is fixed in the two remaining directions. So, the shear deformations are simple shear as shown in Figure 2.10a and the extension deformations are uni-axial strain as shown in Figure 2.10b.

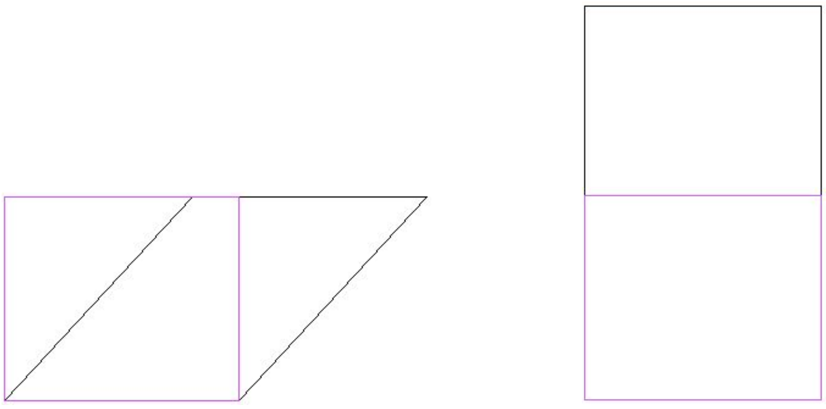

(a) (b)

Figure 2.10: Schematic 2D representation of (a) simple shear and (b) uni-axial strain. In each figure, the undeformed state is shown in purple and the deformed state in black.

Next, the second Piola-Kirchhoff stress tensor $\boldsymbol{S}$ is calculated:

$$\boldsymbol{S} = \boldsymbol{F}^{-1} \cdot \bar{\boldsymbol{P}}^{\mu\mathrm{RVE}}, \tag{2.14}$$

where $\boldsymbol{F}$ is the deformation gradient tensor and $\bar{\boldsymbol{P}}^{\mu\mathrm{RVE}}$ the volume averaged first Piola-Kirchhoff stress tensor. The average first Piola-Kirchhoff stress tensor is calculated following Kouznetsova et al. [31]:

$$\bar{\boldsymbol{P}}^{\mu\mathrm{RVE}} = \frac{1}{V_0} \sum_{j=\overline{2,4}} \vec{f}(c_j)\vec{x}^0(c_j), \tag{2.15}$$

where V_0 is the initial volume of the micro RVE, $\vec{f}(c_j)$ the reaction forces in corner node c_j and $\vec{x}^0$ the initial position of corner node c_j.

The stiffness components are determined by writing Hooke's law in matrix notation:

$$\begin{bmatrix} S_1 \\ \vdots \\ S_6 \end{bmatrix} = \begin{bmatrix} C_{11} & \dots & C_{16} \\ \vdots & \ddots & \vdots \\ C_{61} & \dots & C_{66} \end{bmatrix} \begin{bmatrix} \varepsilon_1^{GL} \\ \vdots \\ \varepsilon_6^{GL} \end{bmatrix}, \tag{2.16}$$

where S_i are second Piola-Kirchhoff stress tensor components, C_{ij} stiffness components and ε_i^{GL} Green-Lagrange strain tensor components. This is rewritten as follows:

$$\begin{bmatrix} S_1 \\ \vdots \\ S_6 \end{bmatrix} = \begin{bmatrix} C_{11}\varepsilon_1^{GL} & \dots & C_{16}\varepsilon_6^{GL} \\ \vdots & \ddots & \vdots \\ C_{61}\varepsilon_1^{GL} & \dots & C_{66}\varepsilon_6^{GL} \end{bmatrix}. \tag{2.17}$$

By splitting the stiffness and strain components and rewriting the stiffness in column form, one ends up with the following equation:

$$\underset{\sim}{S} = \underline{\varepsilon}\,\underset{\sim}{C}, \tag{2.18}$$

where $\underset{\sim}{S}$ is a 6×1 column, $\underline{\varepsilon}$ a 6×21 matrix and $\underset{\sim}{C}$ a 21×1 column. Note that with one deformation of the micro RVE, there will be many zero columns in $\underline{\varepsilon}$. Therefore, six deformations are applied, resulting in $\underset{\sim}{S}$ being a 36×1 column and $\underline{\varepsilon}$ a 36×21 matrix. First, both sides of the equation are pre-multiplied by $\underline{\varepsilon}^T$. Next, $(\underline{\varepsilon}^T \underline{\varepsilon})$ is inversed to isolate $\underset{\sim}{C}$:

$$\underset{\sim}{C} = (\underline{\varepsilon}^T \underline{\varepsilon})^{-1} \underline{\varepsilon}^T \underset{\sim}{S}. \tag{2.19}$$

From these stiffness components, the 6×6 stiffness matrix $\underline{C}_{mat}$ is obtained. Next, the 6×6 compliance matrix $\underline{S}_{mat}$ is calculated:

$$\underline{S}_{mat} = \underline{C}_{mat}^{-1}. \tag{2.20}$$

Finally, the effective elastic properties of the micro RVE are obtained:

$$\underline{S}_{mat} = \begin{bmatrix} \frac{1}{E_x} & -\frac{\nu_{yx}}{E_y} & -\frac{\nu_{zx}}{E_z} & 0 & 0 & 0 \\ -\frac{\nu_{xy}}{E_x} & \frac{1}{E_y} & -\frac{\nu_{zy}}{E_z} & & & \\ -\frac{\nu_{xz}}{E_x} & -\frac{\nu_{yz}}{E_y} & \frac{1}{E_z} & 0 & 0 & 0 \\ 0 & 0 & 0 & \frac{1}{2G_{yz}} & 0 & 0 \\ 0 & 0 & 0 & 0 & \frac{1}{2G_{zx}} & 0 \\ 0 & 0 & 0 & 0 & 0 & \frac{1}{2G_{xy}} \end{bmatrix}. \tag{2.21}$$

2.5 Spherulite model

To model the spherulitic structure, which is observed at the mesoscopic scale, a spherulite model is created in a global spherical coordinate $\{\vec{e}_1,\vec{e}_2,\vec{e}_3\}$. It is assumed that the spherulite fills up the whole volume, i.e. there is no unconstrained amorphous material in between spherulites [17]. A bcc spherulitic stacking is assumed as shown in Figure 2.11. It was proven that the irregularity of the stacking is not important [16]. Due to symmetry, only one eighth of the periodic cubic volume is modelled.

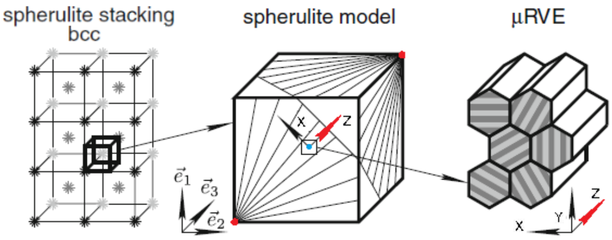

Figure 2.11: Spherulite stacking with the spherulite model, where $\vec{z}$ represents the growth direction of a material point (e.g. the blue dot) and the red dots represent spherulitic centers [17].

The model contains two spherulitic centers, indicated with red dots. From these corners, crystalline lamellae grow in radial direction, indicated by the z-direction. An example of this is given for the material point indicated by the blue dot, of which the growth direction is shown with the red vector $\vec{z}$. So, the orientation of the microstructure depends on the location in the spherulite model.

The obtained effective material properties in the micro RVE are used to describe the material behavior in the spherulite model, considering the orientation of the microstructure in the spherulite model as previously explained. An elastic orthotropic material model, available in MSC Marc 2018 is used for this.

The mesh used for the spherulite model is a cube with length = width = height = 1 mm. Linear isoparametric three-dimensional full integration tetrahedron elements are used. The mesh is shown in Figure 2.12.

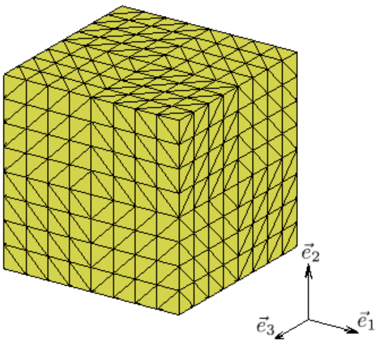

Figure 2.12: Mesh for spherulite model.

2.6 Obtaining material properties of the spherulite model

The spherulite model is globally deformed according to the deformation gradient tensor:

$$\underline{F} = \begin{bmatrix} 1.01 & 0 & 0 \\ 0 & 0.995 & 0 \\ 0 & 0 & 0.995 \end{bmatrix}. \tag{2.22}$$

So, the global applied engineering strain $\bar{\varepsilon}_{11}$, of which its purpose becomes clear in Chapter 2.7, equals 0.01 [-]. The components of the Cauchy stress tensor $\boldsymbol{\sigma}$ are then calculated by dividing force F_{ii} by the surface area A_{ij}:

$$\begin{bmatrix} \sigma_{xx} \\ \sigma_{yy} \\ \sigma_{zz} \end{bmatrix} = \begin{bmatrix} \frac{Fxx}{A_{yz}} \\ \frac{Fyy}{A_{xz}} \\ \frac{Fzz}{A_{xy}} \end{bmatrix}. \tag{2.23}$$

Then, the second Piola-Kirchhoff stress tensor $\boldsymbol{S}$ and Green-Lagrange strain tensor $\boldsymbol{E}$ are calculated as shown in Equation 2.24 and Equation 2.25 respectively:

$$\boldsymbol{S} = J\boldsymbol{F}^{-1} \cdot \boldsymbol{\sigma} \cdot \boldsymbol{F}^{-T}, \tag{2.24}$$

$$\boldsymbol{E} = \frac{1}{2}(\boldsymbol{F}^T \cdot \boldsymbol{F} - \boldsymbol{I}), \tag{2.25}$$

where $\boldsymbol{F}$ is the deformation gradient tensor. Next, the following relation is used:

$$\begin{bmatrix} \varepsilon_1^{GL} \\ \varepsilon_2^{GL} \\ \varepsilon_3^{GL} \\ \varepsilon_4^{GL} \\ \varepsilon_5^{GL} \\ \varepsilon_6^{GL} \end{bmatrix} = \frac{1}{E} \begin{bmatrix} 1 & -\nu & -\nu & 0 & 0 & 0 \\ -\nu & 1 & -\nu & 0 & 0 & 0 \\ -\nu & -\nu & 1 & 0 & 0 & 0 \\ 0 & 0 & 0 & 2+2\nu & 0 & 0 \\ 0 & 0 & 0 & 0 & 2+2\nu & 0 \\ 0 & 0 & 0 & 0 & 0 & 2+2\nu \end{bmatrix} \begin{bmatrix} S_1 \\ S_2 \\ S_3 \\ S_4 \\ S_5 \\ S_6 \end{bmatrix}, \tag{2.26}$$

where $\varepsilon_4^{GL} = \varepsilon_5^{GL} = \varepsilon_6^{GL} = S_4 = S_5 = S_6 = 0$ because of the deformation gradient tensor shown in Equation 2.22. From this, the Young's modulus and Poisson ratio are determined on the mesoscopic scale and equal those of the macroscopic scale, therefore, also the macroscopic problem is solved.

2.7 Procedure to investigate microstructural deformation

In this section, it is first explained how to interpret pole figures (which are used to investigate the deformation behavior of the microstructure). Next, the procedure to obtain pole figures is explained.

A pole figure tells something about the orientation of a vector in a 3D space. For example, consider the vector in Figure 2.13a. The orientation of this vector is plotted on a 2D plane perpendicular to the view direction using equal area projection. This is shown in Figure 2.13b where the 3-direction is the view direction, thus, the direction is plotted on the 1-2 plane. The resulting pole figure is shown in Figure 2.13c.

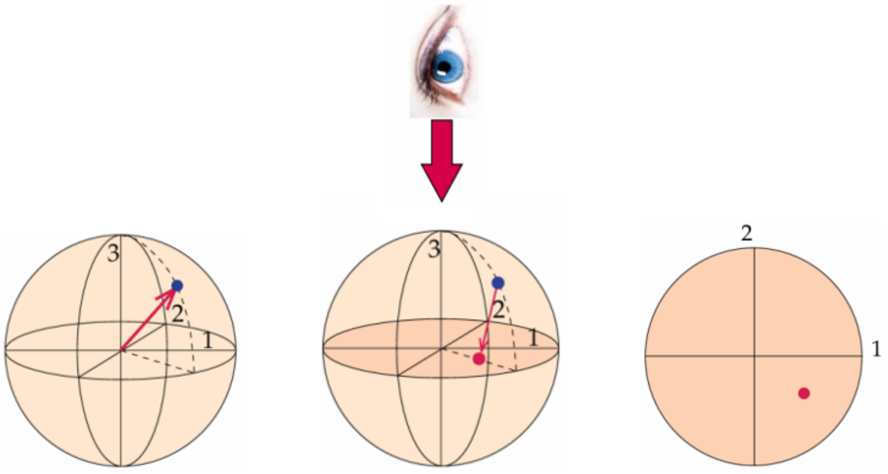

(a) (b) (c)

Figure 2.13: Explanation on how to interpret pole figures. (a) A pole figure is used to indicate the direction of a vector in a 3D space. (b) That direction is then plotted on a 2D plane depending on the view direction. This results in (c) the actual pole figure [15].

An example of pole figures that are used in this project is shown in Figure 2.14. The pole figures used during this project have an $\vec{e}_1$ view direction which is the spherulitic loading direction.

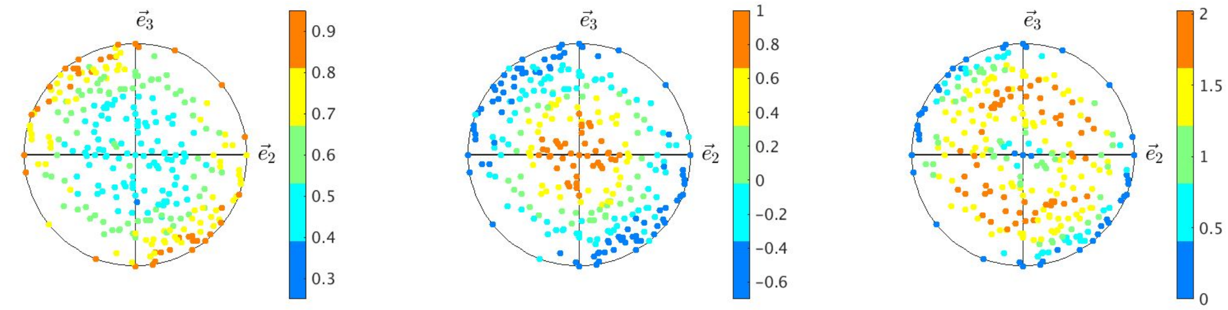

Intralamellar deformation Interlamellar separation Interlamellar shear

Figure 2.14: Pole figure examples, with on the left intralamellar deformation, in the middle interlamellar separation and on the right interlamellar shear. In this project, all deformation values in the pole figures are normalized to the globally applied strain $\bar{\varepsilon}_{11}$ in the spherulite model.

The vector orientations that are plotted in the pole figures represent the orientation of a vector, normal to a fold plane of the micro RVE in the spherulite model (in Chapter 2.5 the orientation of the micro RVE in the spherulite model is explained and in Chapter 2.3.3, fold planes are explained). The procedure to obtain these vectors is explained next. After that, the three deformation types shown in Figure 2.14 are defined.

To obtain these pole figures, first, the spherulite model must be deformed. Next, 25 nodes are randomly selected in the spherulite model, where each node represents a micro RVE with a certain orientation. Each micro RVE consists of 12 differently oriented vectors normal to the fold plane, because of differently oriented hexagonal domains (0°, 30°, ... , 330°). This leads to a total of $25 \times 12 = 300$ differently oriented vectors normal to the fold plane, which are observed in the global spherulitic coordinate system $\{\vec{e}_1, \vec{e}_2, \vec{e}_3\}$. An example of these 300 different oriented normal vectors is shown in Figure 2.14.

In the 25 randomly selected nodes, it is determined how the microstructure is deformed, by determining the Green-Lagrange strain tensor. Next, 25 micro RVEs are deformed according to the observed Green-Lagrange strain tensors, i.e. the microstructural deformation as observed in the spherulite model is reproduced. In these micro RVEs, intralamellar deformation ε^c_{vm}, interlamellar separation ε^a_n and interlamellar shear ε^a_{sh}, as shown in Figure 2.14, are investigated:

$$\varepsilon^c_{vm} = \sqrt{\frac{2}{3}(\varepsilon^2_{c11} + \varepsilon^2_{c22} + \varepsilon^2_{c33} + \frac{\gamma^2_{c23}}{2} + \frac{\gamma^2_{c13}}{2} + \frac{\gamma^2_{c12}}{2})}, \tag{2.27}$$

$$\varepsilon^a_n = \varepsilon_{a11}, \tag{2.28}$$

$$\varepsilon^a_{sh} = \sqrt{\varepsilon^2_{a12} + \varepsilon^2_{a13}}, \tag{2.29}$$

where ε^c_{vm} is the von Mises strain in the crystalline phase, ε_{amn} the average strain components in the amorphous phase and ε_{cmn} and γ_{cmn} are both average strain components in the crystalline phase. These deformations are calculated in a new defined coordinate system, the fold plane coordinate system $\{\vec{i}_1, \vec{i}_2, \vec{i}_3\}$, where $\vec{i}_1$ is normal to the fold plane and $\vec{i}_3$ parallel to the crystalline growth direction, which for example is shown in Figure 2.15a. Figures 2.15a and 2.15b show the movement (indicated with the yellow arrows) between two crystals as described by Equations 2.28 and 2.29 respectively.

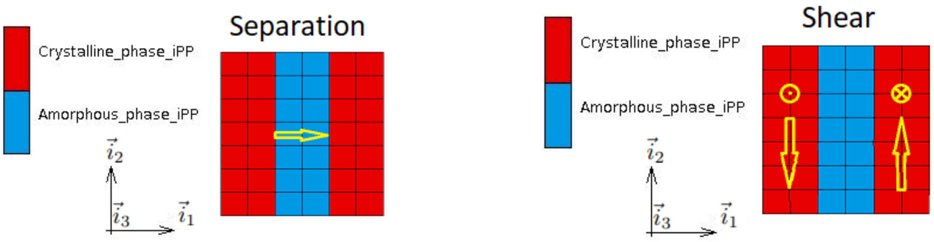

(a) (b)

Figure 2.15: Schematic representation of (a) interlamellar separation and (b) interlamellar shear in the fold plane coordinate system $\{\vec{i}_1, \vec{i}_2, \vec{i}_3\}$, where $\vec{i}_1$ is normal to the fold plane and $\vec{i}_3$ parallel to the crystalline growth direction. The movement of crystalline phases w.r.t. each other is represented by the yellow vectors.

3 Elastic macroscopic mechanical material properties of α-iPP

In this chapter, results obtained with the composite inclusion model and multi-scale finite element model are discussed. First, the influence of the chain tilt angle on the Young's modulus is shown. After that, the influence of the chain tilt angle on microstructural deformation is shown. Finally, the results of the multi-scale finite element model and composite inclusion model are compared.

3.1 Introduction

The main goal of this project is to investigate the influence of the chain tilt angle on macroscopic mechanical material properties of α-iPP and to validate the modelling framework of the composite inclusion model. The influence of the chain tilt angle on the macroscopic elastic mechanical material properties of α-iPP is investigated first by using the multi-scale finite element model [17]. The obtained results are also compared to the obtained results with the composite inclusion model.

3.2 Simulation results

In this section, the simulation results obtained with the multi-scale finite element model are discussed. As mentioned before, three different crystallinities are simulated, with for each five different micro RVEs (as shown in Appendix A), with for each four different fold planes.

3.2.1 Young's moduli

In this section, the obtained macroscopic Young's moduli are discussed, which are shown in Figure 3.1 for each fold plane and different crystallinities.

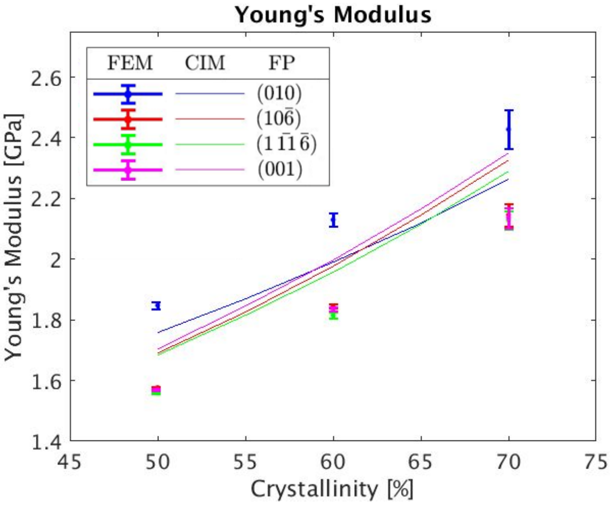

Figure 3.1: Macroscopic Young's modulus for 50%, 60% and 70% crystallinity and for each fold plane. The error bars and curves are the results obtained with the multi-scale finite element model and the composite inclusion model respectively.

First, the multi-scale finite element model results are discussed. After that, the results are compared to the results of the composite inclusion model.

Figure 3.1 shows that the Young's moduli increase with increasing crystallinity. It can be seen that the result for the (001), $(1\,\bar{1}\,\bar{6})$ and $(10\bar{6})$ fold planes are almost identical. The (010) fold plane has a higher Young's modulus. The reason why the material with the (010) fold plane has a higher Young's modulus is explained according to Figure 3.2. In this figure, it can be seen that when crystals of bordering hexagonal domains touch each other under an angle of 0 or 30°, a crystal path occurs. A few crystal paths are indicated by black lines. Assume that the micro RVE shown in Figure 3.2 is loaded in the y-direction, then the crystal paths with a (010) fold plane can interact more efficiently with each other compared to the $(10\bar{6})$ fold plane, because the crystalline chain direction (indicated by the yellow lines) is the stiffest direction of the crystal material.

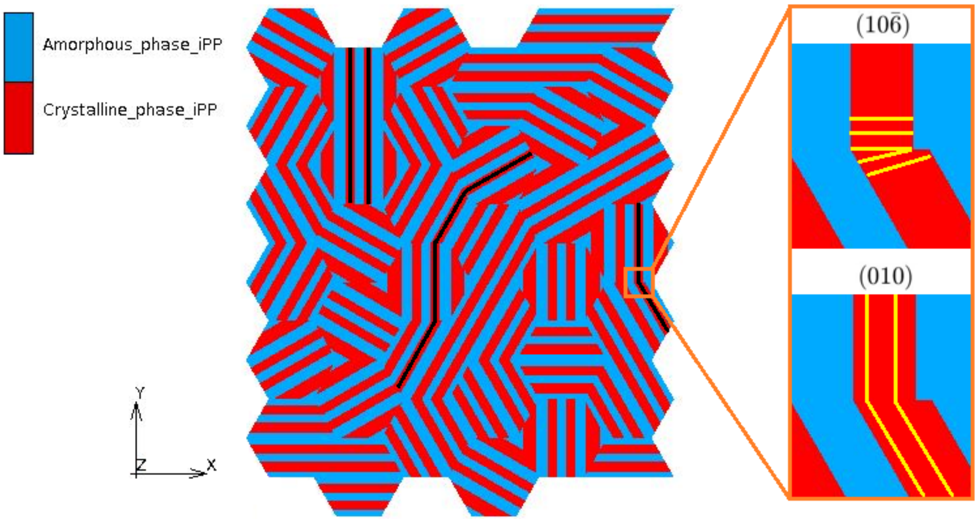

Figure 3.2: Micro RVE with crystal paths indicated by black lines and molecular chain directions in yellow for the (010) and (10$\bar{6}$) fold planes.

This effect of crystal paths is also observed in stress fields and is shown in Figures 3.3a and 3.3b. The stress fields (σ_{yy}) for the micro RVE shown in Figure 3.2 after it is loaded in the y-direction are shown. The Figures 3.3a and 3.3b belong to the (10$\bar{6}$) and (010) fold planes respectively. The crystal paths can be seen more clearly in the right figure. This means that there is a larger stress gradient between the amorphous and crystalline material, i.e. the crystalline material is loaded more efficiently, leading to a higher Young's modulus.

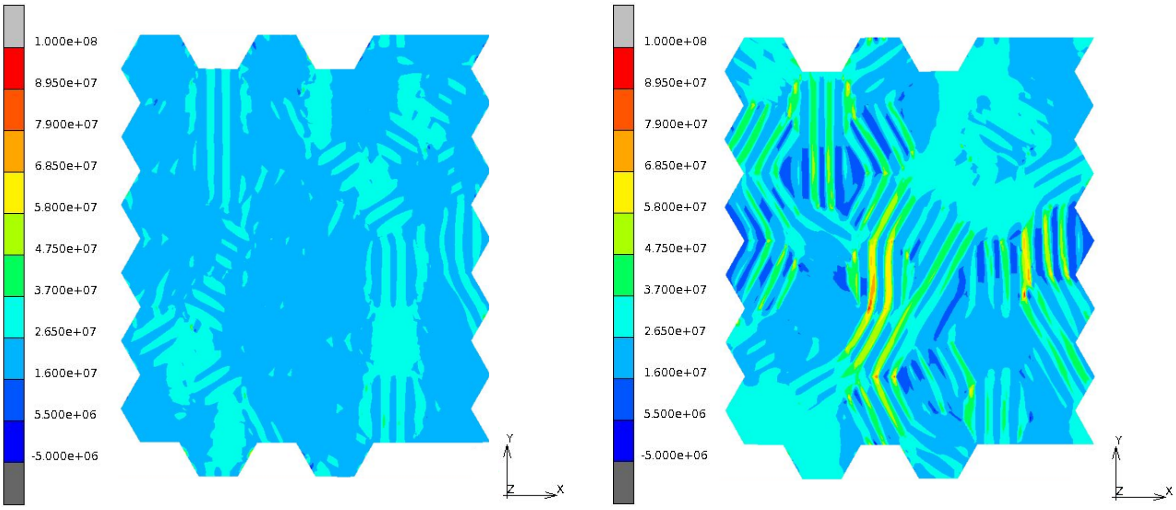

(a)

(b)

Figure 3.3: σ_{yy} field observed in the micro RVE after a vertical load is applied with (a) the (10$\bar{6}$) fold plane and (b) (010) fold plane. The color bar represents the stress in the y-direction.

So, the capability of a crystal to carry load on to another crystal, the "crystal-crystal interaction efficiency", plays an important role on the macroscopic Young's modulus. Therefore, the higher E_2 of the crystalline phase in the fold plane coordinate system as shown in Figure 3.4, the higher the crystal-crystal interaction efficiency. The E_2 component is shown in Table 3 for all fold planes. The capability of a crystal to carry load onto the amorphous phase, the "crystal-amorphous interaction efficiency" is determined by E_1 as shown in Table 3 and the Young's modulus of the amorphous phase.

Table 3: Young's and shear moduli of the crystalline phase for each fold plane in the fold plane coordinate system $\{\vec{i}_1,\vec{i}_2,\vec{i}_3\}$.

Fold plane	$\boldsymbol{E_1}$ [GPa]	$\boldsymbol{E_2}$ [GPa]	$\boldsymbol{E_3}$ [GPa]	$\boldsymbol{G_{23}}$ [GPa]	$\boldsymbol{G_{31}}$ [GPa]	$\boldsymbol{G_{12}}$ [GPa]
$(10\bar{6})$	15.717	2.302	3.671	1.409	1.649	1.406
(001)	13.316	2.302	3.660	1.409	1.718	1.406
(010)	2.302	15.717	3.671	1.649	1.409	1.406
$(1\,\bar{1}1\,\bar{6})$	5.775	2.2289	3.671	1.495	1.545	2.051

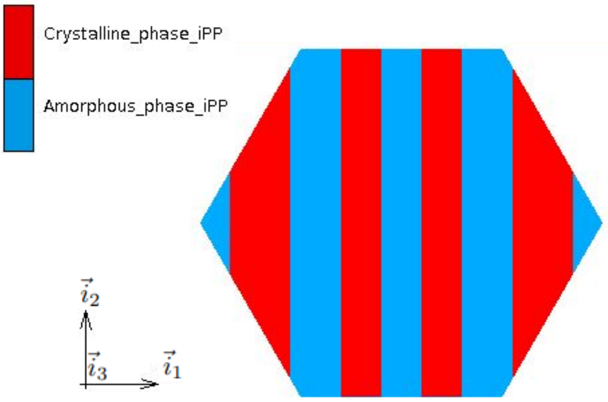

Figure 3.4: Fold plane coordinate system $\{\vec{i}_1,\vec{i}_2,\vec{i}_3\}$, where $\vec{i}_1$ is normal to the fold plane and $\vec{i}_3$ is parallel to the crystalline growth direction. With crystalline lamellae in red and amorphous material in blue.

The reason why the other fold planes lead to the same macroscopic Young's modulus is that the crystal-crystal interaction efficiency is approximately the same as shown in Table 3. It can be seen that the crystal-amorphous interaction efficiency differs for each fold plane. However, because the amorphous material has a much lower Young's modulus, the crystal can not interact efficiently with the amorphous material. Therefore, this does not have a large effect on the macroscopic Young's modulus. The Young's modulus in the crystallographic growth direction and shear moduli are approximately the same for each fold plane as shown in Table 3.

In Figure 3.1, it can be seen that with the composite inclusion model, the (010) fold plane does not have a higher Young's modulus compared to the other fold planes. This can be explained due to the fact that the composite inclusion model does not take crystal paths into account. Overall, the Young's modulus for each fold plane observed in the multi-scale finite element model is in good agreement with the composite inclusion model.

Conclusion: The crystal-crystal interaction efficiency is more important than the crystal-amorphous interaction efficiency for the macroscopic Young's modulus when comparing different fold planes. Loads can be carried more efficiently from one crystal to another with increasing crystal-crystal interaction efficiency. This leads to a higher Young's modulus. A high crystal-amorphous interaction efficiency is less important due to the significantly lower stiffness of the amorphous material. Overall, the Young's modulus for each fold plane observed in the multi-scale finite element model is in good agreement with the composite inclusion model.

3.2.2 Micro-structural deformation of α-iPP

In this section, the deformation behavior of the microstructure of α-iPP is discussed. First, Figures 3.5a - 3.5c are discussed, in which intralamellar deformation, interlamellar separation and interlamellar shear are shown respectively as a function of crystallinity. All values are normalised by the strain applied to the spherulite model $\bar{\varepsilon}_{11}$.

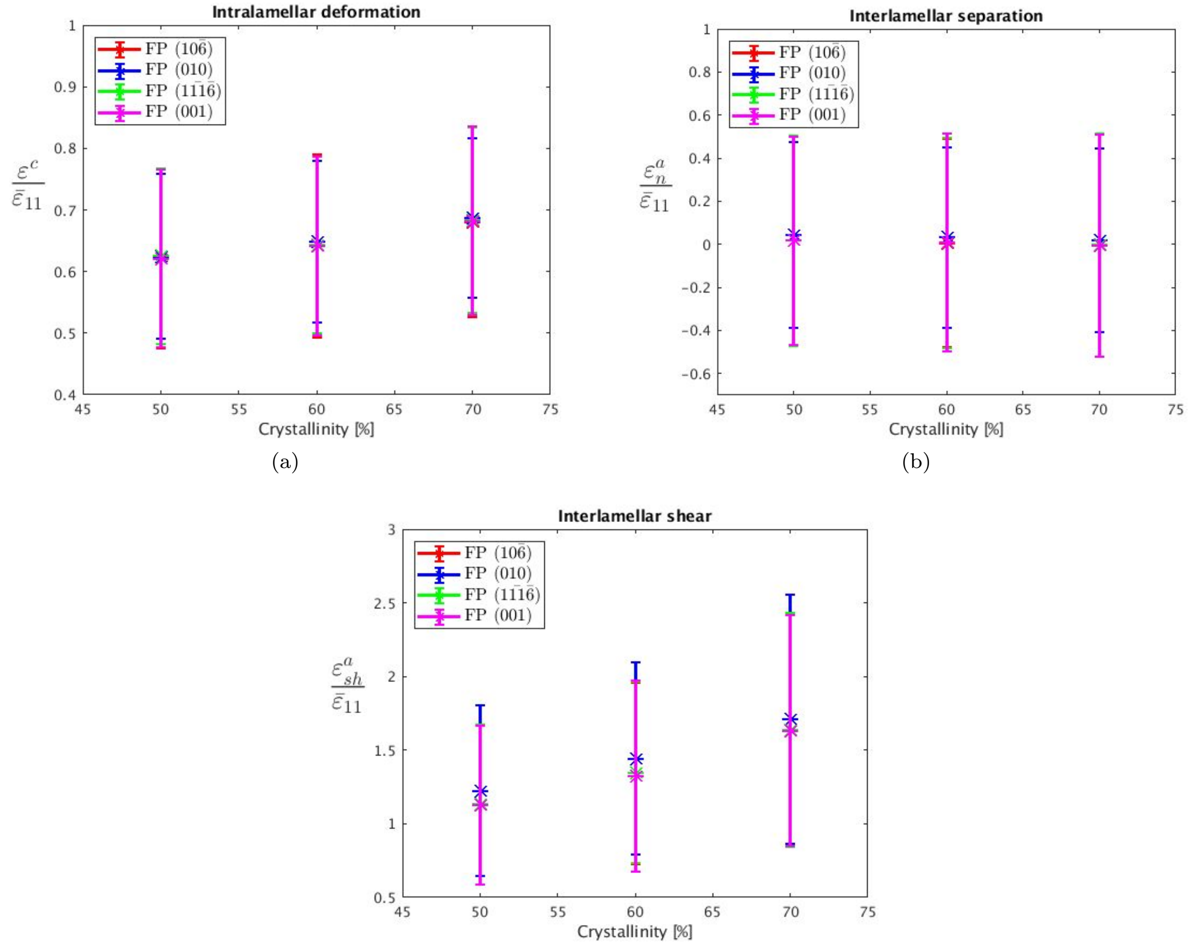

(a) (b)

(c)

Figure 3.5: Standard deviation plots for (a) intralamellar deformation, (b) interlamellar separation and (c) interlamellar shear, where all values are normalised to the applied strain $\bar{\varepsilon}_{11}$ on the spherulite model. In some plots it seems as if the $(10\bar{6})$ fold plane is missing, however, the results of this fold plane are almost identical to those of the (001) fold plane, therefore, they are hard to distinguish.

Intralamellar deformation: It can be seen that the results for all fold planes are almost identical for a certain crystallinity. With increasing crystallinity, the intralamellar deformation slightly increases. This can be easily explained due to the fact that with higher crystallinity, the micro structure gets stiffer. This results in higher stresses to obtain the same deformation which results in more intralamellar deformation.

Interlamellar separation: The first thing that is clearly visible is that the average separation is approximately 0, regardless of the fold plane and crystallinity. This is explained due to the fact that the spherulite model represents isotropic material behavior. It also shows that with increasing crystallinity the magnitudes of separation (with a + sign) do not change. This is counter intuitive because with increasing crystallinity, the stresses to get the same deformation will increase and increasing stresses result in larger strain. It remains unclear why exactly this happens. However, with a test it is shown that with increasing crystallinity the interlamellar separation does not increase. The two micro RVEs that are used are shown in Figures 3.6a and 3.6b. They both have the same orientations. An elongation of 1.1 in the x-direction is applied and both have the $(10\bar{6})$ fold plane.

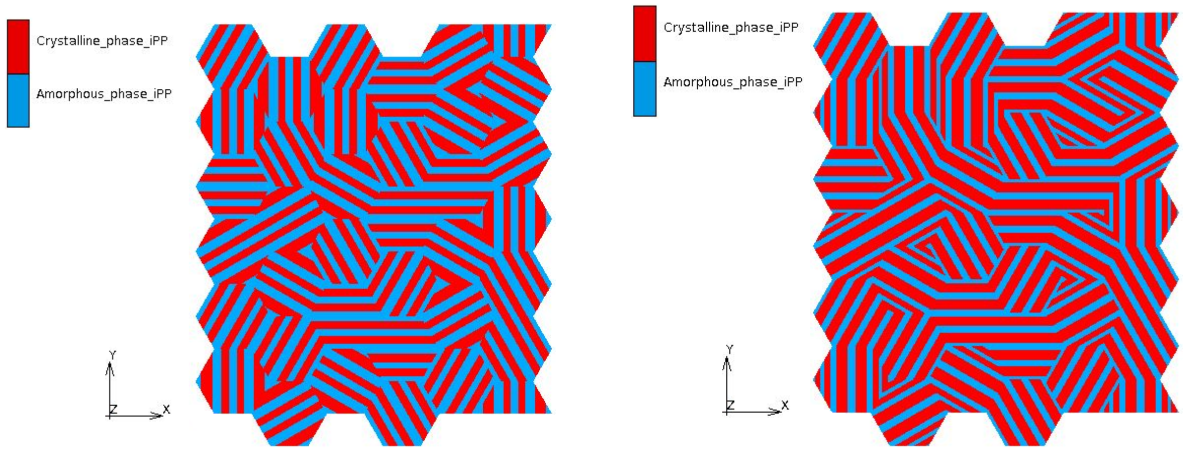

(a) (b)

Figure 3.6: Used meshes to test interlamellar separation as a function of crystallinity. With (a) a micro RVE with 50% crystallinity and (b) the same micro RVE but with 60% crystallinity.

The results are shown in Figure 3.7a and 3.7b. Here it can be seen that the ε_{xx} component between vertical crystals is the same for both micro RVEs. So, it is observed here as well that for increasing crystallinity the interlamellar separation does not increase.

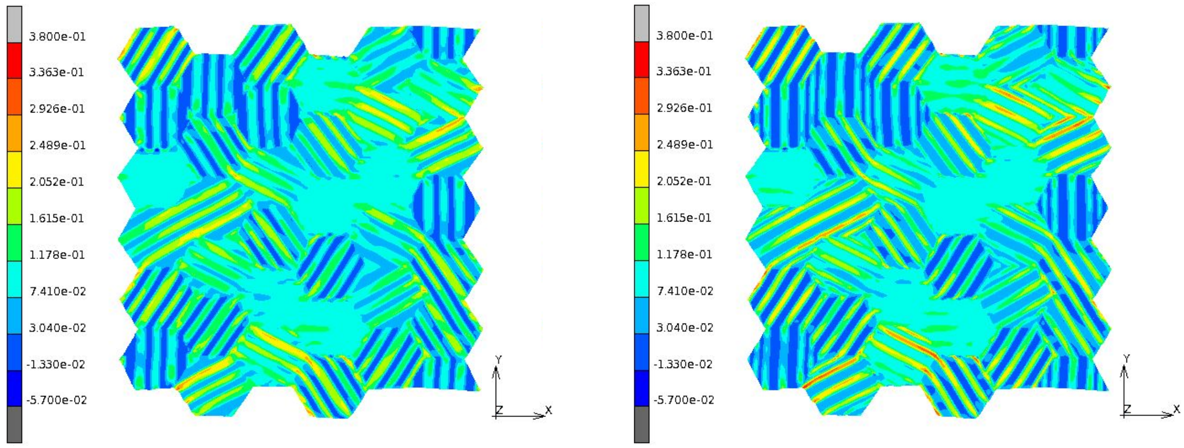

(a) (b)

Figure 3.7: ε_{xx} field observed in the micro RVE after an elongation of 1.1 has been applied in x-direction. With a micro RVE of (a) 50% crystallinity and (b) 60% crystallinity.

It remains uncertain why the magnitude of the positive interlamellar separation does not increase with increasing crystallinity. It most likely has to do something with its surrounding. However, in Figure 3.5b, it is visible that negative separation does increase with increasing crystallinity as one would expect.

Interlamellar shear: From Figure 3.5c it can be concluded that the interlamellar shear is only slightly dependent on the fold plane. Only the (010) fold plane yields larger shear values. It also shows that the interlamellar shear increases with increasing crystallinity. As explained before, increasing crystallinity leads to higher stresses, leading to an increase in interlamellar shear.

3.2.3 Detailed micro-structural deformation of α-iPP

In this section, the deformation of the microstructure is discussed in detail. To do this, four pole figures are shown, which are obtained with the multi-scale finite element model (Figures 3.10 - 3.13) and four that are obtained with the composite inclusion model (Figures 3.14 - 3.17). The center of the pole figures

($\vec{e}_1$-direction) is parallel to the loading direction in the spherulite model. All values in the pole figures are normalised to the globally applied strain $\bar{\varepsilon}_{11}$ in the spherulite model. First, the ones obtained with the multi-scale finite element model will be discussed. After that, they will be compared to those obtained with the composite inclusion model.

The pole figures obtained with the multi-scale finite element model are all obtained through a 50% crystallinity micro RVE with matrix of orientations one (see Appendix A). The multi-scale finite element model pole figures shown here give a good representation of the trend observed in multi-scale finite element model pole figures for 60% and 70% crystallinity (which are shown in Appendix B). Changes in magnitudes due to higher crystallinities are already discussed in Chapter 3.2.2.

Intralamellar deformation: It can be seen, that the trend for the $(10\bar{6})$ and (001) fold planes are similar. Their values are lowest in the center of the pole figure (i.e. with fold plane normals parallel to the globally applied deformation in the spherulite model) and increase towards the outside of the pole figure. This can be explained due to the fact that with normals to the global $\vec{e}_1$-direction, the crystals are mainly interacting with amorphous material. The more the normals are pointed perpendicular w.r.t. the global $\vec{e}_1$-direction, the more the crystals are exposed to shear, resulting in easier deformation of the crystal. When the normals are approximately perpendicular to the globally applied deformation, the crystal-crystal interaction efficiency starts having a large effect resulting in larger crystal deformation.

The pole figures for the (010) and $(1\,1\bar{1}\,\bar{6})$ fold planes show a different trend compared to the other fold planes. The magnitude in the center is higher as its surrounding due to the fact that the (010) and $(1\,1\bar{1}\,\bar{6})$ fold planes have a significantly lower crystal-amorphous interaction efficiency. This is most easily observed for the (010) fold plane because that fold plane has the lowest crystal-amorphous interaction efficiency. The magnitude on the edges for the (010) fold plane is lower compared to the other fold planes due to a significantly higher crystal-crystal interaction efficiency.

Interlamellar separation: For the interlamellar separation it can be observed that the trend is the same for all fold planes. The separation has highest positive values for normals parallel to the spherulite loading direction. It has the highest negative values for normals perpendicular to the loading direction and values are around 0 in between. This is explained according to Figures 3.8a and 3.8b. Here one can immediately see that with normals (yellow vector), parallel to the loading direction (red vectors) maximum positive separation occurs and with normals perpendicular to the loading direction, maximum negative separation occurs.

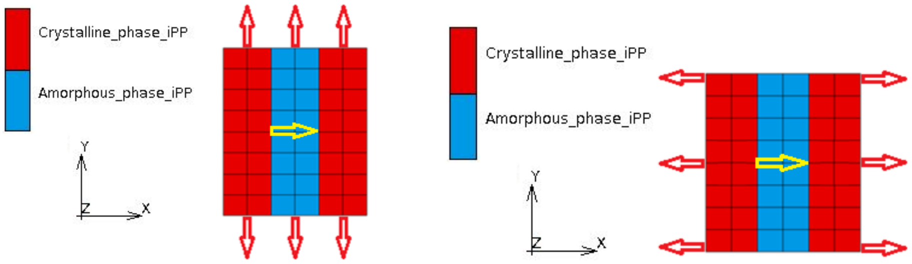

(a) (b)

Figure 3.8: Schematic representation of two load-cases with red arrows indicating the load and the yellow arrow indicating the normal to the fold plane, where (a) has a normal perpendicular to the loading direction, leading to negative separation and (b) a normal parallel to the loading direction, leading to positive separation.

For the (010) fold plane, the magnitudes at the edge of the pole figure have a lower magnitude compared to the other fold planes. This happens due to the fact that in the (010) fold plane, the crystal-crystal interaction efficiency is significantly higher. Therefore, the crystals and thus the amorphous material in between two crystals stretch less when they are loaded as shown on the left side in Figure 3.8a. Therefore, the amorphous material contracts less. The center of the pole figure for the (010) fold plane, has lower interlamellar separation as one would expect due to the lower stiffness in that direction compared to other fold planes. This is the case, however, the difference in magnitude compared to the other fold planes is too small to be visible due to the color bar of the pole figure. This effect is easier observed for the pole figures for higher crystallinities as shown in Appendix 3.2.3.

Interlamellar shear: The trend observed in the interlamellar shear is the same in all pole figures. When the normal of the fold plane is perpendicular or parallel to the loading direction, there is almost no interlamellar shear. Normals oriented differently do have interlamellar shear. If one looks carefully it can be seen that the magnitudes are slightly higher in the (010) fold plane compared to other fold planes. Since the pole figure for interlamellar shear are all similar, it can be concluded that the chain tilt angle has almost no effect on the interlamellar shear.

Finally, it can be clearly seen that microstructural deformation is dominated by interlamellar shear. This is because the multi-scale finite element model uses a spherulite model which has strongly anisotropic material behavior (of the microstructure). This imposes large shear deformation on the microstructure. This is explained according to Figures 3.9a and 3.9b. In Figure 3.9a a spherulitic structure is exposed to a deformation indicated by the red vectors. On the left side of Figure 3.9b, amorphous material in between crystal lamellae before the deformation is shown. On the right side of Figure 3.9b, the amorphous material in between the crystal lamellae after deformation is shown.

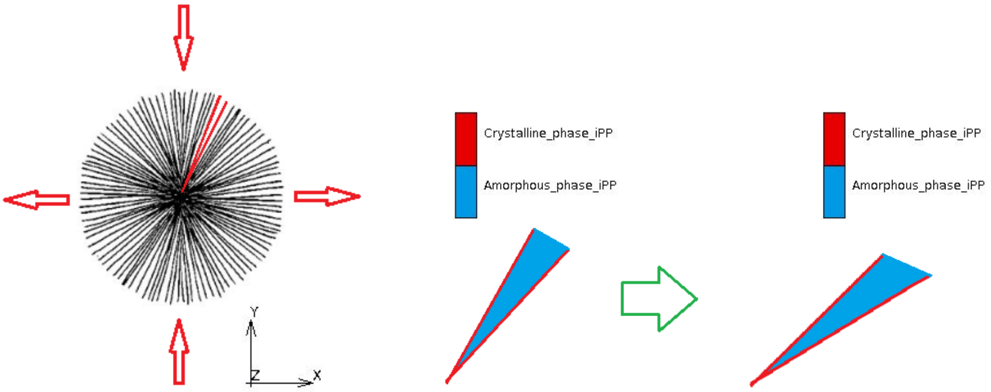

(a) (b)

Figure 3.9: Schematic representation of large interlamellar shear obtained with the multi-scale finite element model. (a) With crystal lamellae in black and an applied deformation (red vectors). (b) Schematic representation of crystal lamellae (red) and amorphous material in between (blue) before deformation on the left side and after deformation on the right side.

Conclusion: From this, it can be concluded that there are no major differences in microstructural deformation for different fold planes. Intralamellar deformation is influenced the most by the chain tilt angle. When comparing fold planes, most differences are observed for the (010) fold plane compared to the other fold planes. This makes sense because the (010) fold plane tilt angle differs the most compared to the other chain tilt angles. With increasing crystallinity, the trends observed in the pole figures for each fold plane do not change but the deformation magnitudes do change.

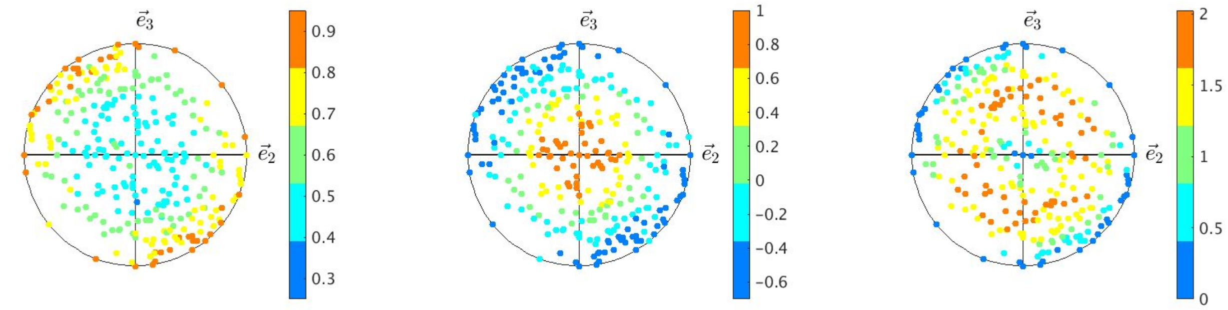

Intralamellar deformation Interlamellar separation Interlamellar shear

Figure 3.10: Pole figure obtained with multi-scale finite element model, matrix of orientations 1, 50% crystallinity and fold plane $(10\bar{6})$.

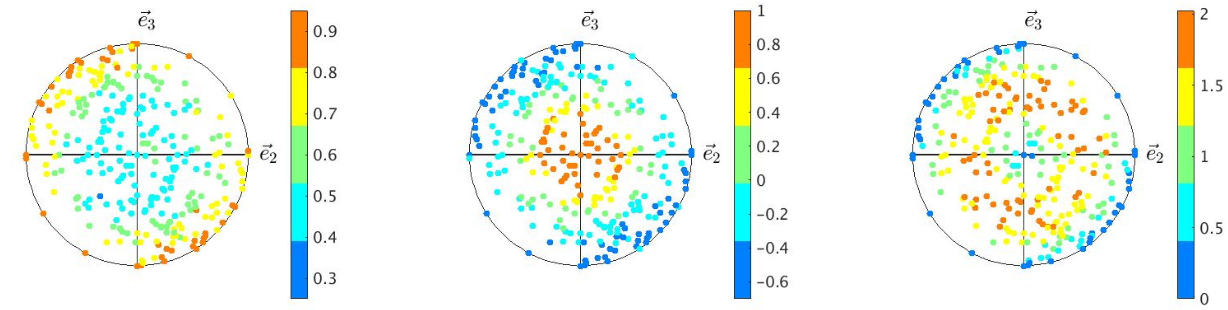

Intralamellar deformation Interlamellar separation Interlamellar shear

Figure 3.11: Pole figure obtained with multi-scale finite element model, matrix of orientations 1, 50% crystallinity and fold plane (001).

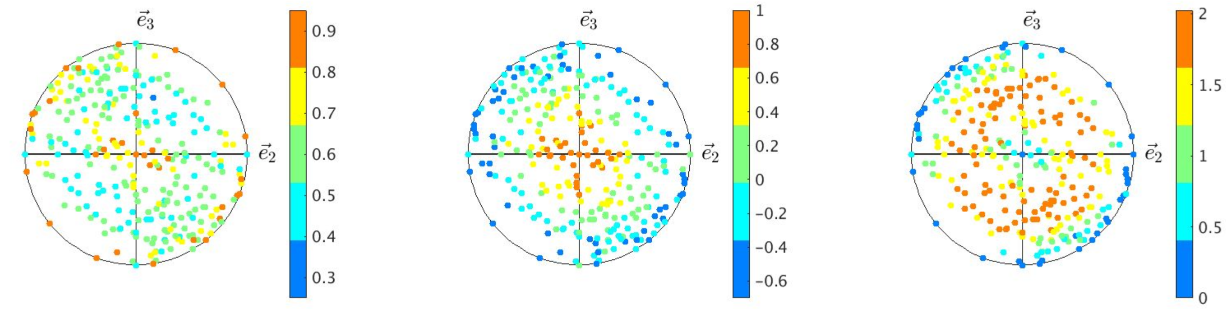

Intralamellar deformation Interlamellar separation Interlamellar shear

Figure 3.12: Pole figure obtained with multi-scale finite element model, matrix of orientations 1, 50% crystallinity and fold plane (010).

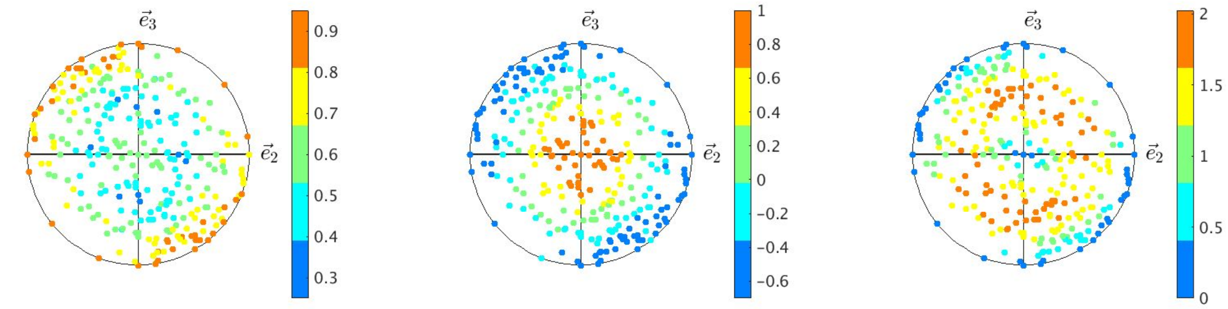

Intralamellar deformation Interlamellar separation Interlamellar shear

Figure 3.13: Pole figure obtained with multi-scale finite element model, matrix of orientations 1, 50% crystallinity and fold plane $(1\,\bar{1}1\,\bar{6})$.

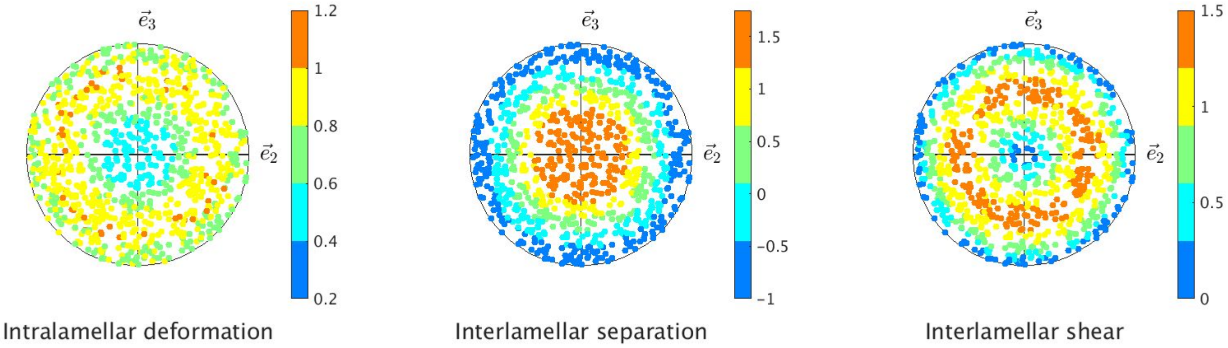

Figure 3.14: Pole figure obtained with composite inclusion model, 50% crystallinity and fold plane $(10\bar{6})$.

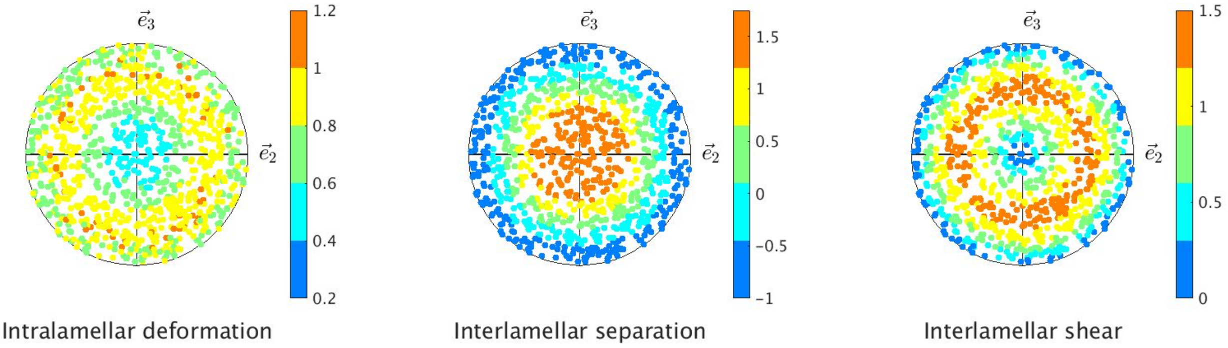

Figure 3.15: Pole figure obtained with composite inclusion model, 50% crystallinity and fold plane (001).

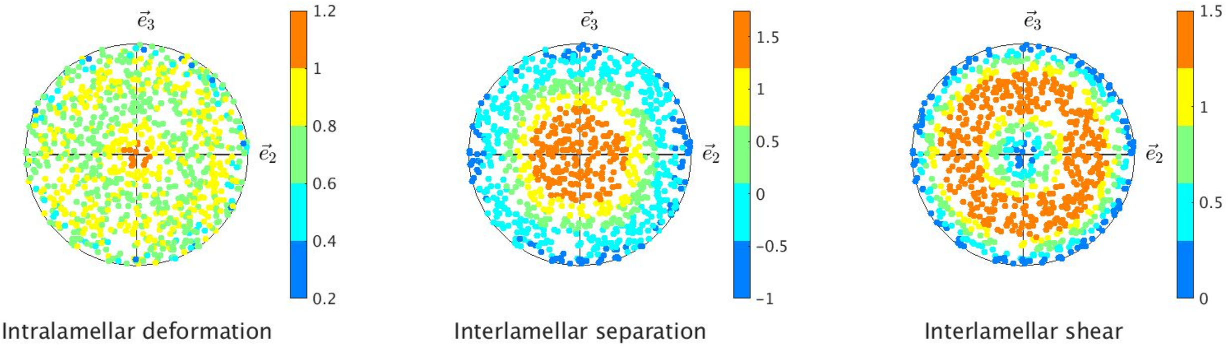

Figure 3.16: Pole figure obtained with composite inclusion model, 50% crystallinity and fold plane (010).

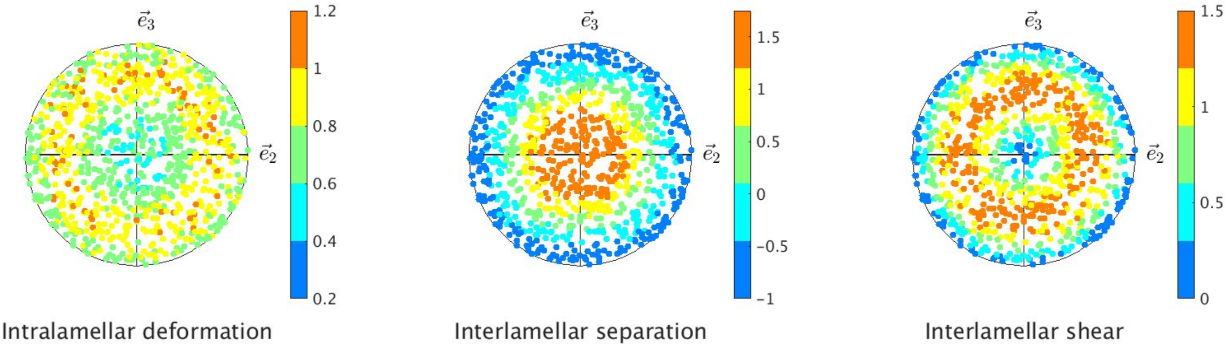

Figure 3.17: Pole figure obtained with composite inclusion model, 50% crystallinity and fold plane $(1\,\bar{1}1\,\bar{6})$.

Comparison between composite inclusion model and multi-scale finite element model: Next, the pole figures shown in Figures 3.10 - 3.13 are compared to the ones in Figures 3.14 - 3.17. First the comparison in trends is discussed. After that the comparison in magnitudes is discussed.

In general, the observed trends for microstructural deformation in each fold plane, for both simulations models, are in good agreement. An important reason for this is the nature of interactions between the crystalline and amorphous phase. The nature of interactions between the crystalline and amorphous phases is explained according to Figure 3.18 and defined by four conditions:

$$\varepsilon_2^c = \varepsilon_2^a \text{ and } \sigma_1^c = \sigma_1^a, \tag{3.1}$$

$$\varepsilon_1^c \neq \varepsilon_1^a \text{ and } \sigma_2^c \neq \sigma_2^a. \tag{3.2}$$

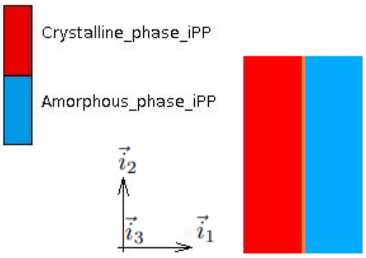

Figure 3.18: Fold plane coordinate system, with amorphous phase in blue, crystal phase in red and the fold plane in orange.

These conditions are satisfied in a natural way in the multi-scale finite element model, where the composite inclusion model numerically enforces them. Note that for the multi-scale finite element model, these conditions only hold on the fold plane. The four conditions given in Equations 3.1 and 3.2, interact with the anisotropy of the crystalline phase, which depends on the fold plane.

It is shown that the trends for interlamellar separation and shear are the same for the multi-scale finite element model and composite inclusion model. In interlamellar deformation, the composite inclusion model has a different prediction on the edges of the pole figure for all fold planes compared to the multi-scale finite element model. However, this is not due to the nature of interactions between the crystalline and amorphous phase, but due to the fact that the composite inclusion model does not take crystal paths into account, where in the multi-scale finite element model crystal paths are the reason for higher values at the edges of the pole figures. The center of the pole figure for the $(1\,\bar{1}1\,\bar{6})$ fold plane in the multi-scale finite element model is higher compared to its surroundings. This is not the case in the composite inclusion model.

There are quite large differences in magnitudes between both models. Especially for interlamellar shear and separation. This is explained due to the fact that the composite inclusion model does not use a spherulite model which imposes a large amount of shear to the microstructure. This results in less interlamellar shear, which on its turn leads to higher intralamellar deformation and interlamellar separation.

Conclusion: It can be concluded that both models predict the trends of microstructural deformation in a similar way. An important reason for this, is the nature of interactions between the crystalline and amorphous phases, which in the multi-scale finite element model are satisfied in a natural way, where in the composite inclusion model, these are numerically enforced. Most differences are observed in intralamellar deformation which can be explained due to the fact that the composite inclusion model does not take crystal paths into account. Magnitude wise, there are larger differences, because the composite inclusion model does not take into account a spherulitic structure which imposes large shear deformation on the microstructure.

4 Elasto-viscoplastic macroscopic mechanical material properties of α-iPP

In this section, the α-iPP elasto-viscoplastic simulations will be discussed. First, the new material models that are used are discussed. Next, the used material parameters are discussed. Finally, the results of the new multi-scale finite element model will be discussed and compared to the results of the composite inclusion model.

4.1 Introduction

To enable elasto-viscoplastic simulations of α-iPP, new material models are implemented in the multi-scale finite element model. The new material model used to describe the crystalline phase is a crystal plasticity model [18]. With this model it is enabled to capture crystallographic slip of the crystalline phase. For the amorphous phase an elastic-plastic isotropic material model available in MSC Marc is used. The spherulite material is described by an elastic-plastic orthotropic material model available in MSC Marc.

4.2 New material models

In this section, the new material models are discussed which are used to model the crystalline phase, amorphous phase and the material of the spherulite model.

4.2.1 Crystalline phase

The crystal plasticity model [18] is used to model the crystalline phase. This model communicates with MSC Marc 2014 via user sub-routine Hypela2 [32]. The crystal plasticity model works in combination with the Total Lagrange procedure in Marc [33]. In the crystal plasticity model, the elastic behavior of the crystalline phase was described by the following linear relation:

$$\boldsymbol{S}_e = {}^4\boldsymbol{C} : \boldsymbol{E}_e, \tag{4.1}$$

where $\boldsymbol{S}_e$ is the symmetric elastic second Piola-Kirchhoff stress tensor, ${}^4\boldsymbol{C}$ the fourth-order stiffness tensor and $\boldsymbol{E}_e$ the symmetric elastic Green-Lagrange strain tensor which is defined as follows:

$$\boldsymbol{E}_e = \frac{1}{2}(\boldsymbol{F}_e^T \cdot \boldsymbol{F}_e - \boldsymbol{I}), \tag{4.2}$$

where $\boldsymbol{I}$ is the identity tensor and $\boldsymbol{F}_e$ the elastic deformation gradient tensor. The plastic behavior of the crystalline phase was described by crystallographic slip, taking all physically distinct slip systems (N_s) into account:

$$\boldsymbol{L}_p = \sum_{\alpha=1}^{N_s} \dot{\gamma}^\alpha \boldsymbol{P}_0^\alpha, \tag{4.3}$$

where $\boldsymbol{L}_p$ is the plastic velocity gradient tensor, $\dot{\gamma}^\alpha$ the slip rate and $\boldsymbol{P}_0^\alpha$ the Schmid tensor in the reference configuration of slip system α. More theoretical details on the crystal plasticity model can be found in [34].

4.2.2 Amorphous phase

It is chosen to implement an elastic-plastic isotropic material model, available in MSC Marc 2014 [35]. However, to accurately describe the amorphous phase, the EGP-model should be used. To combine the crystal plasticity model and EGP-model, the crystal plasticity model must be modified such that it works with the updated Lagrange procedure. In this project, due to time issues, this was not possible. However, during this project, it became clear that the crystal plasticity model also must be modified to the updated Lagrange procedure (due to convergence issues, discussed later on in this chapter), to simulate large strain plasticity. Because the crystal plasticity model must be modified to the updated Lagrange procedure, combining the EGP-model and the crystal plasticity model will be straight forward, therefore, investing time in more complex material models available in MSC Marc is not worth the time.

4.2.3 Spherulite model

The new material model for the spherulite model is the elastic-plastic orthotropic material model which is available in MSC Marc 2014 [35]. It is chosen not to use hardening because of several reasons. First, with the applied strains in this project, hardening will not have a large effect. Second, it is difficult to extract hardening from the micro RVE. Third, later in this chapter it will become clear that the modelling scheme used in this project is not sufficient to obtain physically relevant results, but a FE^2 modelling scheme should be used instead. Therefore, implementing hardening in the spherulite model is not worth the time.

4.3 Simulation parameters

All the material parameters that were used for the simulations in Chapter 3, are used here as well to model the elastic regime. Only additional and adjusted parameters will be discussed here.

4.3.1 Crystalline phase

There are eight physically distinct slip systems N_s in α-iPP [21] as shown in Figure 4.1. These are the most active slip systems for α-iPP [36] and implemented in the crystal plasticity model during this project.

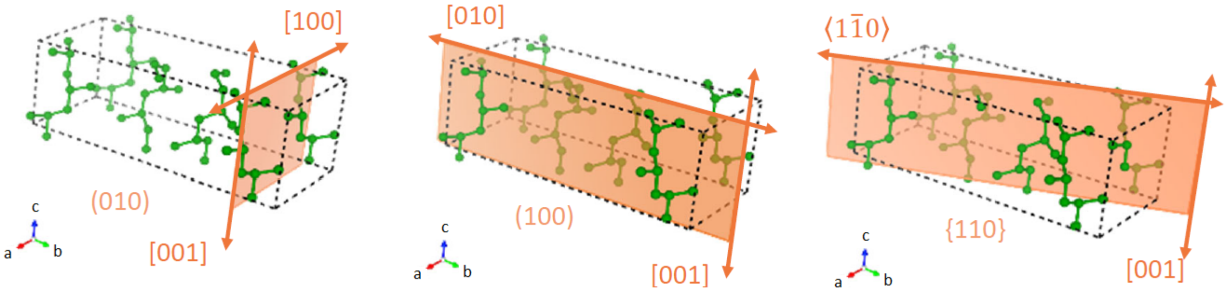

Figure 4.1: Most active slip systems in α-iPP [21].

To accurately capture the slip kinetics, the powerlaw implemented in the crystal plasticity model is replaced by the Eyring slip law:

$$\dot{\gamma}^{\alpha} = \dot{\gamma}_0^{\alpha} \sinh\left(\frac{\tau^{\alpha}}{\tau_0^{\alpha}}\right), \tag{4.4}$$

where $\dot{\gamma}^{\alpha}$ is the slip rate, $\dot{\gamma}_0^{\alpha}$ the initial slip rate, τ^{α} the resolved shear stress, τ_0^{α} the slip resistance and α the slip system. The derivations leading to the Eyring slip law implementation can be found in Appendix D. During this project, no hardening law is used, i.e. τ_0^{α} is a constant. The parameters used in this project to represent the slip kinetics for α-iPP are shown in Table 4.

Table 4: Used parameters for the most active slip systems in α-iPP [21].

Slip plane	**Slip direction**	**Initial slip rate [1/s]**	**Slip resistance [MPa]**
(010)	[100]	2×10^{-10}	1.35
(010)	[001]	9×10^{-8}	1.35
(100)	[010]	1×10^{-8}	1.35
(100)	[001]	1×10^{-8}	1.35
(110)	[001]	4×10^{-11}	1.35
(110)	[1$\bar{1}$0]	4×10^{-12}	1.35
(1$\bar{1}$0)	[001]	4×10^{-11}	1.35
(1$\bar{1}$0)	[110]	4×10^{-12}	1.35

In combination with the Eyring slip law, as shown in Equation 4.4, these parameters represent the slip kinetics for α-iPP [21]. The slip kinetics are shown in Figure 4.2. Here, the thick and thin curves represent the slip kinetics that are used in the composite inclusion model and multi-scale finite element model respectively. They only differ at very small strain rates which is no problem.

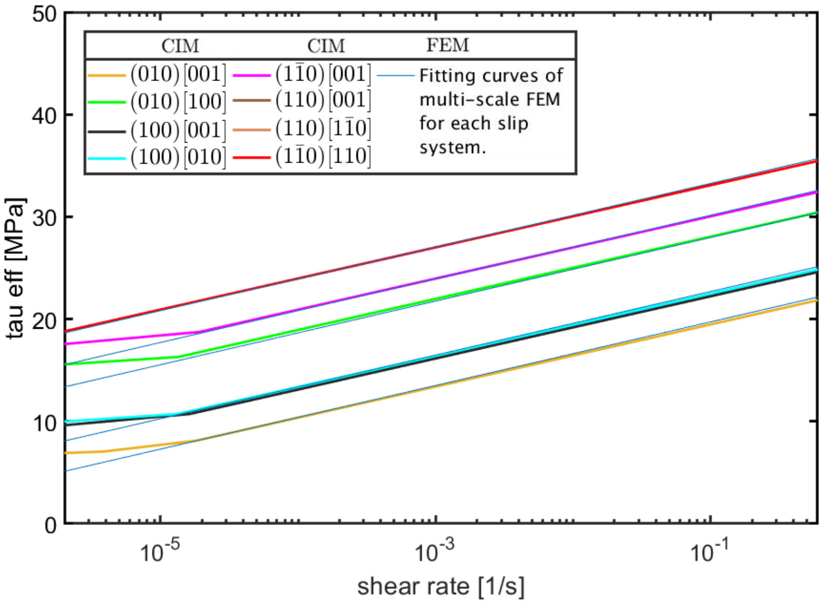

Figure 4.2: Slip kinetics for α-iPP [21]. The thick curves represent the slip kinetics used in the composite inclusion model and the thin curves represent the slip kinetics used in the multi-scale finite element model.

4.3.2 Amorphous phase

For the amorphous material, the yield stress is set to 9 MPa. The strain hardening is described as follows:

$$H = \sqrt{q} + \sqrt[8]{q}\frac{3}{2} + \sqrt[12]{q}\frac{1}{2} + 1, \tag{4.5}$$

where H is the strain hardening and q the equivalent plastic strain. For more information on the strain hardening see page 334 of [35]. These material parameters are not physically relevant, but they are purely chosen to obtain a good representation of the stress-strain curve of the amorphous material, as observed in the EGP model, which is implemented in the composite inclusion model. This is shown in Figure 4.3.

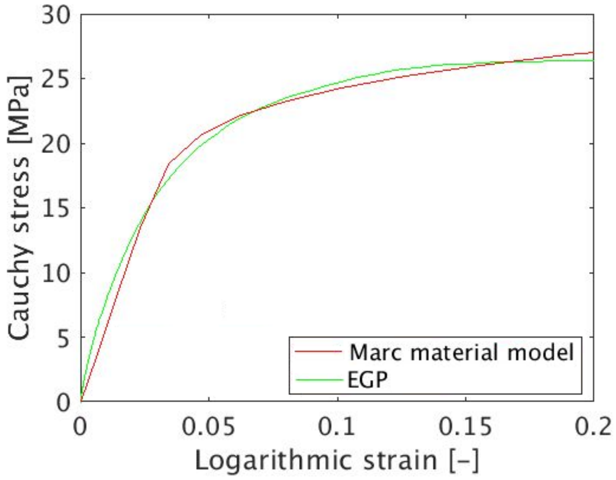

Figure 4.3: Stress-strain curves for pure amorphous material, obtained by an elastic-plastic isotropic material model available in MSC Marc [35], and the EGP model, which is implemented in the composite inclusion model.

4.3.3 Spherulite model

Since the anisotropic Hill yield criterion is used in the elasto-plastic spherulite material model, the σ_{xx}, σ_{yy}, σ_{zz}, σ_{zy}, σ_{zx} and σ_{yx} yield stresses are required. To determine the yield stresses, the micro RVE is deformed accordingly, e.g. to determine these σ_{xx} yield stress, a ε_{xx} strain is applied to the micro RVE, using new boundary conditions as discussed in Chapter 4.3.4. To extract these yield stresses, first, the second Piola-Kirchhoff yield stress is determined by determining the intersection between the elastic and plastic tangents, as shown in Figure 4.4. Next, it is checked if the stress-strain curve has a slope of 0 somewhere. If this is the case, then the stress at that part of the curve will be considered the second Piola-Kirchhoff yield stress, as shown in the bottom right sub-figure of Figure 4.4. The spherulite model works with the updated Lagrange procedure, therefore, MSC Marc considers stresses as Cauchy stresses [33]. Therefore, the second Piola-Kirchhoff yield stress is rewritten to a Cauchy yield stress.

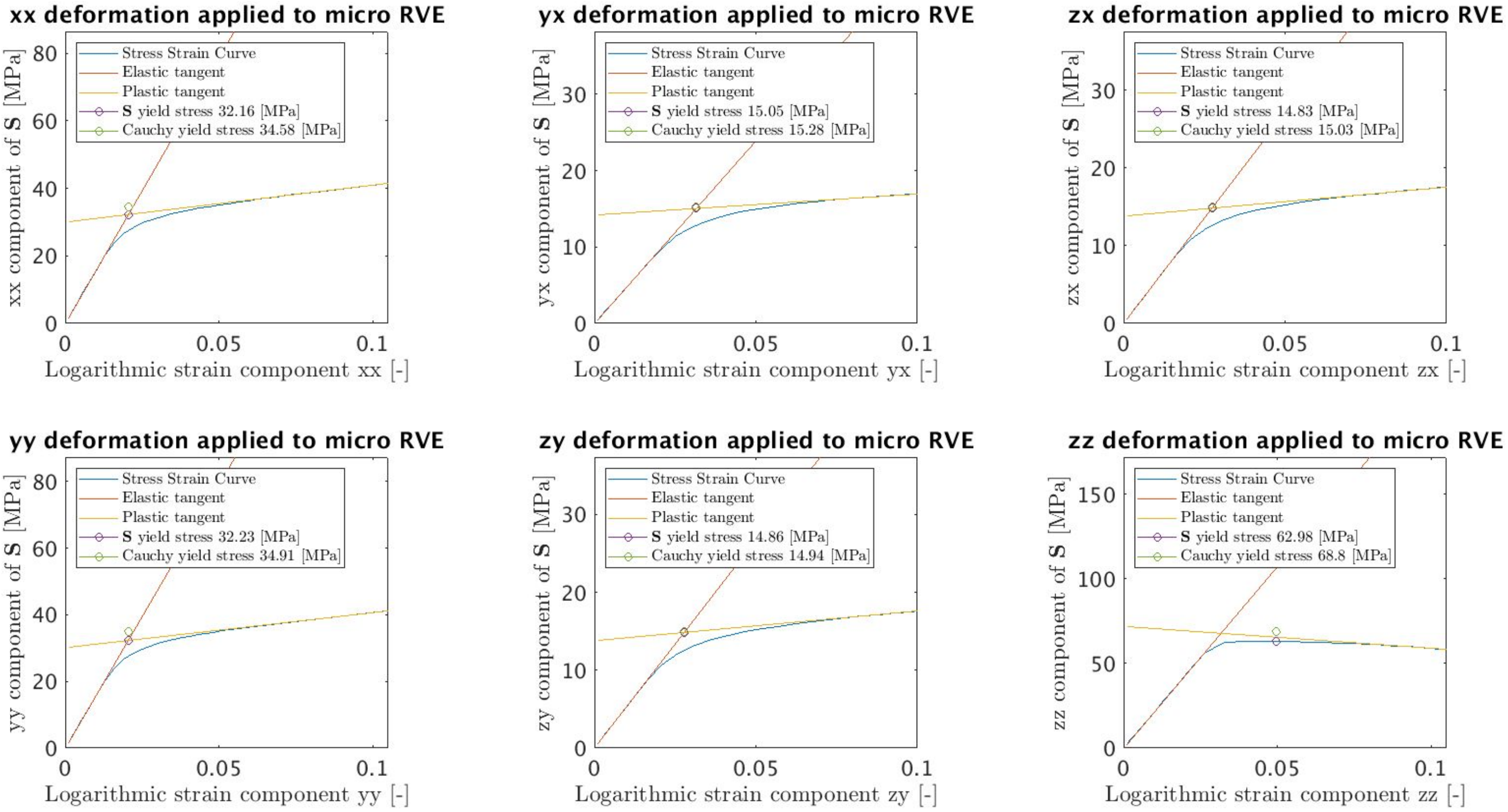

Figure 4.4: Procedure to obtain all six yield stresses required for the anisotropic Hill yield criterion.

4.3.4 New boundary conditions

As mentioned before, the original multi-scale finite element model deforms the micro RVE with uni-axial strain and simple shear. To determine the yield stresses, this is not sufficient. Therefore, the boundary conditions have been adjusted. Simple shear is changed to shear and uni-axial strain is changed to uni-axial stress. These are schematically shown in Figures 4.5a and 4.5b.

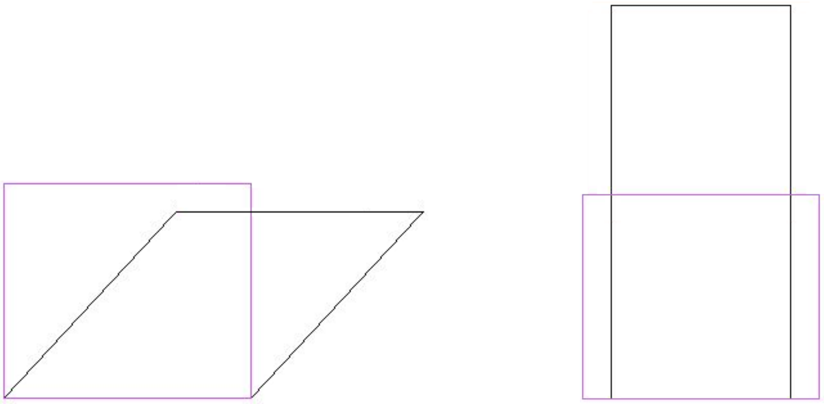

(a) (b)

Figure 4.5: Schematic 2D representation of (a) shear and (b) uni-axial stress, where in each figure the undeformed state is shown in purple and the deformed state in black.

Additionally, the engineering strain ε_{eng} as shown in Table 2 is set to 0.1[-]. Also, the spherulite model is now exposed to uni-axial stress, as shown in Figure 4.5b, where the engineering strain is set to -0.1[-]. So, the spherulite model is now deformed by applying compression. The globally applied strain rate in both the micro RVE and spherulite model is set to 0.02[s^{-1}].

4.4 Simulation results

In this section, the simulation results are discussed. In Appendix C, the obtained yield stresses, in the micro RVE, for all fold planes with a crystallinity of 50% can be found. These yield stresses are used for the anisotropic Hill yield criterion in the elasto-plastic spherulite material model. Due to the convergence problems in the micro RVE, it was not possible to obtain results for 60% and 70% crystallinity. An investigation on the convergence problems is given in Appendix E. The macroscopic stress-strain curves of all fold planes, with a crystallinity of 50%, obtained in both models are shown in Figure 4.6.

First, the multi-scale finite element model results are discussed. After that, they are compared to those of the composite inclusion model. The obtained yield stresses and Young's moduli for each fold plane are shown in Table 5. It can be seen that the Young's modulus is only visibly larger for the (010) fold plane as expected due to the larger crystal-crystal interaction efficiency as explained in Chapter 3.2.1. The yield stresses are obtained in a similar way as the yield stresses in the micro RVE as explained in Chapter 4.3.3. The only difference is that here, the intersection between the elastic and plastic tangent immediately yields the Cauchy yield stress, since the spherulite model runs on the updated Lagrange procedure.

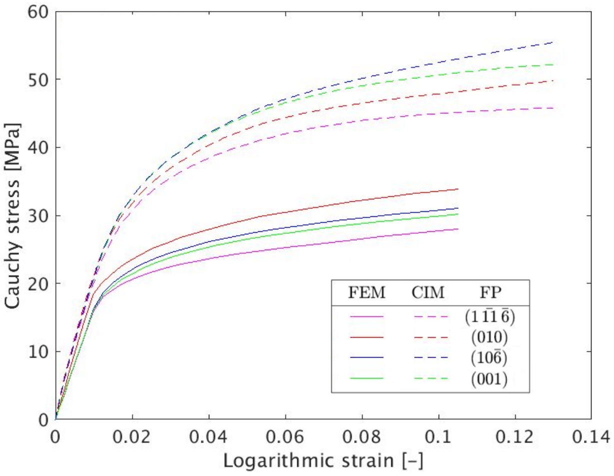

Figure 4.6: Macroscopic stress-strain curves for all fold planes, where the dashed lines are results obtained with the composite inclusion model and the normal lines results obtained with the multi-scale finite element model.

Table 5: Cauchy yield stresses and Young's moduli observed in spherulite model for each fold plane.

Fold plane	**Yield stress [MPa]**	**Young's modulus [GPa]**
$(10\bar{6})$	26	1.64
(010)	28	1.93
(001)	25	1.63
$(1\,\bar{1}\,\bar{6})$	23	1.62

It can be seen that for the yield stresses, the following holds: (010) > $(10\bar{6})$ > (001) > $(1\,\bar{1}\,\bar{6})$. This means that the slip systems are most easily activated for each fold plane in the following order: $(1\,\bar{1}\,\bar{6})$ > (001) > $(10\bar{6})$ > (010).

The reason why this might happen is explained according to Figure 4.7.

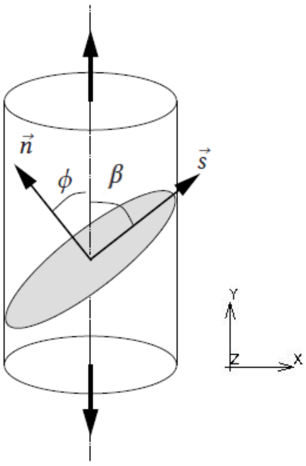

Figure 4.7: A slip system where $\vec{s}$ is the slip direction, $\vec{n}$ the slip plane normal, ϕ angle between the normal and loading direction (y-direction) and β the angle between slip direction and loading direction [37].

Here, the resolved shear stress is calculated as follows:

$$\tau = \sigma P, \tag{4.6}$$

where τ is the resolved shear stress, σ the uni-axial stress and P the Schmid factor:

$$p = \cos\phi\cos\beta, \tag{4.7}$$

where ϕ is the angle between the normal to the slip plane and the loading direction and β the angle between the slip direction and loading direction as shown in Figure 4.7. Slip occurs if τ reaches a critical value. If the slip direction is either parallel or perpendicular to the loading direction, the Schmid factor equals 0, because, if $\phi = 90°$, then $\beta = 0°$ and if $\phi = 0°$, then $\beta = 90°$. This results in a resolved shear stress that equals 0, i.e. no slip will occur regardless of the stress (σ).

So, the Schmid factor plays an important role for the activation of a slip system. Also, as explained in the previous chapter, most of the stress is carried from one crystal to the other via crystal paths. The direction of crystal-crystal loading with respect to the chain direction is schematically shown in Figure 4.8. Here, the loading direction is indicated by the red vectors, the yellow lines represent the chain direction, the material in red and blue represent the crystalline and amorphous phase respectively. The crystal-crystal loading direction is perpendicular to the chain direction in the $(10\bar{6})$ and (001) fold planes, parallel to the (010) fold plane chain direction and has an angle of ≈ 60° with respect to the chain direction in the $(1\,\bar{1}1\,\bar{6})$ fold plane.

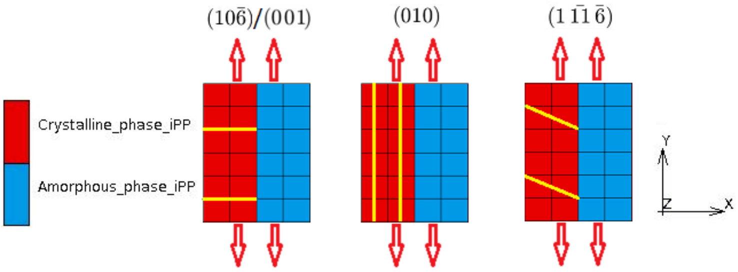

Figure 4.8: Schematic representation of perfect crystal-crystal interaction for each fold plane, where the red vectors are the loading direction, yellow lines the molecular chain direction, crystal material in red and amorphous material in blue.

The angles between the crystal-crystal loading direction and chain direction are known. Also, the angles between the chain direction and slip direction can be determined using Figure 4.1 in combination with the used monoclinic lattice parameters given in Chapter 2.3. Knowing these angles, the Schmid factors for each slip system in all fold planes can be determined. The results for each slip system in each fold plane are shown in Table 6.

Table 6: Schmid factor for each slip system in each fold plane, considering crystal-crystal loading.

Slip system	$\mathbf{(10\bar{6})}$	**(001)**	**(010)**	$\mathbf{(1\bar{1}1\bar{6})}$
(010)[100]	0.16	0.16	0.16	0.49
(010)[001]	0	0	0	0.43
(100)[010]	0	0	0	0.43
(100)[001]	0	0	0	0.43
(110)[001]	0	0	0	0.43
$(110)[1\bar{1}0]$	≈0.26	≈0.26	≈0.05	≈0.23
$(1\bar{1}0)[001]$	0	0	0	0.43
$(1\bar{1}0)[110]$	≈0.26	≈0.26	≈0.05	≈0.23

The lower the Schmid factor, the harder it is to activate a slip system as shown in Equation 4.6. When the Schmid factor equals 0, the slip system can not be activated. In Table 6, it is shown that the Schmid factors for each fold plane are ordered as follows:

$$(010) < (10\bar{6}) = (001) < (1\bar{1}1\bar{6}), \tag{4.8}$$

where (010) has the lowest values. This is probably one of the reasons why (010) has the highest yield stress and $(1\,\bar{1}1\,\bar{6})$ the lowest yield stress as shown in Table 5. To be sure that this is one of the reasons, the activation of slip systems has to be investigated more extensively, using pole figures. Unfortunately that was not possible during this project due to convergence problems as explained in Appendix E.

Conclusion: The chain tilt angle has a noticeable effect on the activation of slip systems. One of the reasons is probably the Schmid factors resulting from crystal-crystal loading. However, to be sure a more elaborate investigation using pole figures has to be done.

Comparison to composite inclusion model: It can be immediately seen that the stress-strain curves for all fold planes in the composite inclusion model are significantly different compared to those of the multi-scale finite element model. The following reasons might contribute to this:

1. The fact that in the multi-scale finite element model, the microstructural deformation is interlamellar shear dominated (as shown in Chapter 3), which also has the lowest yield stress. In the composite inclusion model, interlamellar shear is less dominant.
2. An artefact because the yield stresses in the multi-scale finite element model are obtained in the total Lagrange procedure, using Green-Lagrange strain and second Piola Kirchhoff stress. The composite inclusion model works with Cauchy stress and logarithmic strains, which Marc uses with the updated Lagrange procedure. The updated Lagrange and total Lagrange procedures in Marc yield different results as shown in Appendix E.
3. A material model that can not accurately capture the complex material behavior of the micro RVE is used for the spherulite model. Complex material model(s) are used just to determine the Young's moduli and yield stresses, where the composite inclusion model uses complex material models to get the complete macroscopic stress-strain curve.
4. An inaccurate material model is used for the amorphous phase.

Due to these facts it is not possible to draw hard conclusions for the comparison between the composite inclusion model and multi-scale finite element model. To make a good comparison between both models, first, the crystal plasticity model has to be rewritten to the updated Lagrange procedure. This will compensate for reason two that is previously mentioned. Also, this will enable the combination of the EGP-model and crystal plasticity model, compensating reason four that is previously mentioned. The status on modifying the crystal plasticity model to the updated Lagrange procedure is given in Appendix F. After that, the micro RVE and spherulite model should be directly linked, i.e. create an FE^2-model. This will enable the spherulite model to constantly accurately capture complex material behavior of the microstructure, i.e. compensating point three previously mentioned. After that, the activation of slip systems based on different fold planes, can be investigated more elaborately and accurately, using pole figures, in which the slip rate $\dot{\gamma}$ in each slip system is plotted. Unfortunately this was not possible during this project due to convergence problems as explained in Appendix E. If this is all done, the modelling framework of the composite inclusion model can be validated.

5 Conclusion and recommendations

The main objective in this thesis is to investigate the influence of the chain tilt angle on macroscopic mechanical material properties for α-iPP and to validate the modelling framework of the composite inclusion model. To achieve this, an existing multi-scale finite element model is used to investigate the influence of the chain tilt angle in the elastic regime. To investigate the influence of the tilt angle in the plastic regime, the material models in the multi-scale finite element model, are replaced by other material models.

5.1 Conclusions

1. The Young's modulus depends more on crystal-crystal interaction efficiency than on crystal-amorphous interaction efficiency. If the stiffest direction of the crystal interacts with amorphous material, the crystal can not carry as much load on to its surroundings. When the stiffest direction interacts with other crystals, the crystal can carry on the load more efficiently to its surroundings, resulting in a higher Young's modulus.
2. Deformation of the microstructure of α-iPP is dominated by interlamellar shear. This happens because the microstructure in the spherulite model is strongly anisotropic in radial direction. This exposes the microstructure to large shear deformation.
3. The chain tilt angle has almost no effect on interlamellar separation and interlamellar shear. The chain tilt angle has a larger effect on intralamellar deformation, where the trend for the (010) and $(1\,\bar{1}\,\bar{6})$ fold planes is different compared to the $(10\bar{6})$ and (001) fold planes due to a different crystal-amorphous interaction efficiency. Most differences are explained due to the different crystal-crystal interaction efficiency in each fold plane.
4. Simulating large strain plasticity with the Total Lagrange procedure gives convergence issues. It is shown by a convergence study that convergence of the simulations will improve when the multiscale finite element model runs on the Updated Lagrange procedure.
5. The chain tilt angle influences the Schmid factors, and therefore, the chain tilt angle has a noticeable effect on the activation of slip systems. To draw further conclusions on why this happens, a more elaborate investigation must be performed.
6. The multi-scale finite element model and composite inclusion model have similar results for the Young's moduli. They also have similar results for the trends in microstructural deformation in the elastic regime. An important reason for this is the nature of interactions between the crystalline and amorphous phases, which in the multi-scale finite element model are satisfied in a natural way, where in the composite inclusion model, these are numerically enforced. Only the results at the edges of the pole figures for intralamellar deformation is different for both models. This is due to the fact that the composite inclusion model does not take crystal paths into account. Also, the magnitudes of microstructural deformations differ for both models. This is due to the fact that the composite inclusion model works with an aggregate of randomly oriented composite inclusions instead of a spherulitic structure which is used in the multi-scale finite element model.

5.2 Recommendations

1. Modify the crystal plasticity model such that it can work with the Updated Lagrange procedure in MSC Marc. This will make sure simulations either do not crash or crash at a later stage in the loadcase. This will also enable the combination of the crystal plasticity model and EGP-model, giving more accurate results in the micro RVE. Also, this will enable improving elements used in the spherulite model (see recommendation 5).
2. Combine the EGP-model and the crystal plasticity model. If the crystal plasticity model is rewritten such that it works with the Updated Lagrange procedure, it is straightforward to combine these two material models. This will result in more accurate simulations of the microstructure.
3. The crystalline stiffness tensor used in this work is obtained making many assumptions. It is beneficial to use one obtained in a more thorough way in future work. For example, Chávez Thielemann is currently working on such a stiffness tensor.

4. Right now, the spherulite model is based on a elasto-plastic material model available in MSC Marc. Only the yield stresses and Young's moduli are determined by complex material model(s). Because of this, the spherulite model is not able to yield physically relevant results. Change the multi-scale finite element model to an FE^2 model where each material point is directly connected to the micro RVE. This should enable the spherulite model to get more accurately physically relevant results.

5. The eight-node, isoparametric, arbitrary hexahedral elements, used in the micro RVE, can suffer from locking. To prevent this in the future, replace these elements by 20-node, isoparametric, arbitrary hexahedral elements, using reduced integration. If the crystal plasticity model is modified to the updated Lagrange method, replace the linear isoparametric, tetrahedron elements, used in the spherulite model, by isoparametric five-node, low-order tetrahedron elements to get more accurate results.

6. After the previously mentioned improvements are implemented in the multi-scale finite element model, use it to investigate the microstructural deformation in the plastic regime. This will give a better insight on the activation of slip systems based on the chain tilt angle. To do this, create pole figures where the strain rate in each slip system is plotted. Also, the multi-scale finite element model can then be used to validate the modelling framework of the composite inclusion model in the plastic regime.

References

[1] D. Graham-Rowe. Nat photon. *Nature Photonics*, 1(5):248, 2007.

[2] G. Laschet, M. Spekowius, R. Spina, and C. Hopmann. Multiscale simulation to predict microstructure dependent effective elastic properties of an injection molded polypropylene component. *Mechanics of Materials*, 105:123–137, 2017.

[3] L.H. Sperling. *Introduction to physical polymer science.* John Wiley & Sons, 2005.

[4] D.M. Parks and S. Ahzi. Polycrystalline plastic deformation and texture evolution for crystals lacking five independent slip systems. *Journal of the Mechanics and Physics of Solids*, 38(5):701–724, 1990.

[5] B.J. Lee, S. Ahzi, and R.J. Asaro. On the plasticity of low symmetry crystals lacking five independent slip systems. *Mechanics of Materials*, 20(1):1–8, 1995.

[6] A. Dahoun, G.R. Canova, A. Molinari, M.J. Philippe, and C.H. G'sell. The modelling of large strain textures and stress-strain relations of polyethylene. *Texture, Stress, and Microstructure*, 14:347–354, 1991.

[7] B.J. Lee, D.M. Parks, and S. Ahzi. Micromechanical modeling of large plastic deformation and texture evolution in semi-crystalline polymers. *Journal of the Mechanics and Physics of Solids*, 41(10):1651–1687, 1993.

[8] B.J. Lee, A.S. Argon, D.M. Parks, S. Ahzi, and Z. Bartczak. Simulation of large strain plastic deformation and texture evolution in high density polyethylene. *Polymer*, 34(17):3555–3575, 1993.

[9] J.A.W. van Dommelen, D.M. Parks, M.C. Boyce, W.A.M. Brekelmans, and F.P.T. Baaijens. Micromechanical modeling of the elasto-viscoplastic behavior of semi-crystalline polymers. *Journal of the Mechanics and Physics of Solids*, 51(3):519–541, 2003.

[10] M. Mirkhalaf, J.A.W. van Dommelen, L.E. Govaert, J. Furmanski, and M.G.D. Geers. Micromechanical modeling of anisotropic behavior of oriented semicrystalline polymers. *Journal of Polymer Science Part B: Polymer Physics*, 57(7):378–391, 2019.

[11] G.I. Taylor. Plastic strain in metals: Journal of the institute of metals, v. 62. 1938.

[12] J.W. Hutchinson. Bounds and self-consistent estimates for creep of polycrystalline materials. *Proceedings of the Royal Society of London. A. Mathematical and Physical Sciences*, 348(1652):101–127, 1976.

[13] R.J. Asaro and A. Needleman. Overview no. 42 texture development and strain hardening in rate dependent polycrystals. *Acta metallurgica*, 33(6):923–953, 1985.

[14] G. Sachs. Zur ableitung einer fließbedingung. zeitschrift des vereines deutscher ingenieure. 72:734–736, 1928.

[15] J.A.W. van Dommelen. Lectures of computational and experimental micromechanics, 2019.

[16] J.A.W. Van Dommelen, D.M. Parks, M.C. Boyce, W.A.M. Brekelmans, and F.P.T. Baaijens. Micromechanical modeling of intraspherulitic deformation of semicrystalline polymers. *Polymer*, 44(19):6089–6101, 2003.

[17] M. Poluektov, J.A.W. van Dommelen, L.E. Govaert, I. Yakimets, and M.G.D. Geers. Micromechanical modelling of poly (ethylene terephthalate) using a layered two-phase approach. *Journal of Materials Science*, 48(10):3769–3781, 2013.

[18] T. van Nuland and M. Oude Vrielink. *Beaver documentation*, 2020.

[19] L.E. Govaert and E.T.J. Klompen. *The EGP model for dummies*, 2015.

[20] L.E. Govaert, T.A.P. Engels, G.W.M. Peters, and H.E.H. Meijer. Predicting mechanical performance of polymers directly from processing history.

[21] H.N. Chávez Thielemann, H.J.M. Caelers, L.E. Govaert, and J.A.W. van Dommelen. Micromechanical modeling of the elasto-viscoplastic behavior of α-ipp (in preparation).

[22] PB Bowden and RJ Young. Deformation mechanisms in crystalline polymers. *Journal of Materials Science*, 9(12):2034–2051, 1974.

[23] J. Furmanski, J. Schaefer, L.E. Govaert, and J.A.W. van Dommelen. Does crystal thickness dictate yield kinetics in polyethylene? 2018.

[24] R.H. Boyd and W.B. Liau. Mechanical moduli of spherulitic lamellar semicrystalline polymers. *Macromolecules*, 19(8):2246–2249, 1986.

[25] K. Tashiro, M. Kobayashi, and H. Tadokoro. Vibrational spectra and theoretical three-dimensional elastic constants of isotactic polypropylene crystal: an important role of anharmonic vibrations. *Polymer journal*, 24(9):899–916, 1992.

[26] M. Kamezawa, K. Yamada, and M. Takayanagi. Preparation of ultrahigh modulus isotactic polypropylene by means of zone drawing. *Journal of Applied Polymer Science*, 24(5):1227–1236, 1979.

[27] G. Natta and P. Corradini. Structure and properties of isotactic polypropylene. *Il Nuovo Cimento (1955-1965)*, 15(1):40–51, 1960.

[28] B. Lotz and J.C. Wittmann. The molecular origin of lamellar branching in the α (monoclinic) form of isotactic polypropylene. *Journal of Polymer Science Part B: Polymer Physics*, 24(7):1541–1558, 1986.

[29] J.A. Sauer, D.R. Morrow, and G.C. Richardson. Morphology of solution-grown polypropylene crystal aggregates. *Journal of Applied Physics*, 36(10):3017–3021, 1965.

[30] AJ Lovinger. Microstructure and unit-cell orientation in α-polypropylene. *Journal of Polymer Science: Polymer Physics Edition*, 21(1):97–110, 1983.

[31] V.G. Kouznetsova, M.G.D. Geers, and W.A.M. Brekelmans. Multi-scale second-order computational homogenization of multi-phase materials: a nested finite element solution strategy. *Computer methods in applied Mechanics and Engineering*, 193(48-51):5525–5550, 2004.

[32] MSC Marc. *MSC Marc 2020 Manual D*, 2020.

[33] MSC Marc. *MSC Marc 2020 Manual B*, 2020.

[34] R.J. Asaro. Crystal plasticity. 1983.

[35] MSC Marc. *MSC Marc 2020 Manual A*, 2020.

[36] H.N. Chávez Thielemann. Kickoff presentation. 2020.

[37] J.A.W. van Dommelen. Lecture notes computational micro mechanics.

[38] V.G. Kouznetsova. Advanced computational continuum mechanics part ii. pages 37–38.

[39] M.G.M. Itskov. *Tensor Algebra and Tensor Analysis for Engineers*. Springer Nature Switzerland AG 2019, 2019.

A Matrix of orientations

In this appendix, the matrices of orientations which are used during the project are shown. These matrices describe the orientation of a hexagonal domain in the micro RVE. First, the five matrices for a crystallinity of 50% are shown, next for 60%, and finally for 70%.

50% crystallinity:

$$[1]\begin{bmatrix} 150 & 0 & 330 & 90 & 300 & 240 \\ 180 & 210 & 180 & 30 & 60 & 120 \\ 270 & 300 & 240 & 90 & 270 & 0 \\ 120 & 60 & 30 & 150 & 240 & 30 \\ 330 & 150 & 90 & 270 & 300 & 210 \\ 0 & 120 & 60 & 210 & 330 & 180 \end{bmatrix}[^\circ],\ [2]\begin{bmatrix} 210 & 150 & 300 & 90 & 330 & 60 \\ 180 & 30 & 180 & 120 & 240 & 150 \\ 240 & 60 & 210 & 270 & 0 & 60 \\ 0 & 270 & 90 & 330 & 150 & 240 \\ 300 & 120 & 0 & 210 & 30 & 120 \\ 330 & 270 & 90 & 30 & 300 & 180 \end{bmatrix}[^\circ],$$

$$[3]\begin{bmatrix} 120 & 270 & 60 & 210 & 300 & 330 \\ 180 & 240 & 150 & 120 & 270 & 0 \\ 30 & 180 & 60 & 330 & 30 & 90 \\ 0 & 30 & 90 & 300 & 240 & 150 \\ 90 & 300 & 210 & 60 & 210 & 180 \\ 330 & 0 & 150 & 120 & 240 & 270 \end{bmatrix}[^\circ],\ [4]\begin{bmatrix} 240 & 0 & 300 & 270 & 90 & 60 \\ 150 & 180 & 30 & 120 & 240 & 120 \\ 210 & 60 & 330 & 150 & 300 & 0 \\ 330 & 240 & 0 & 330 & 180 & 210 \\ 120 & 300 & 150 & 30 & 90 & 30 \\ 90 & 270 & 210 & 60 & 180 & 270 \end{bmatrix}[^\circ],$$

$$[5]\begin{bmatrix} 330 & 240 & 210 & 120 & 30 & 300 \\ 180 & 90 & 330 & 270 & 180 & 210 \\ 240 & 30 & 120 & 0 & 150 & 60 \\ 150 & 60 & 300 & 210 & 90 & 0 \\ 270 & 30 & 240 & 120 & 150 & 330 \\ 300 & 90 & 0 & 60 & 270 & 180 \end{bmatrix}[^\circ].$$

60% crystallinity:

$$[6]\begin{bmatrix} 300 & 0 & 90 & 180 & 300 & 90 \\ 210 & 330 & 210 & 330 & 30 & 240 \\ 150 & 120 & 30 & 270 & 150 & 60 \\ 240 & 270 & 60 & 150 & 120 & 300 \\ 0 & 120 & 30 & 270 & 180 & 90 \\ 60 & 180 & 330 & 210 & 240 & 0 \end{bmatrix}[^\circ],\ [7]\begin{bmatrix} 150 & 0 & 330 & 90 & 300 & 240 \\ 180 & 210 & 180 & 30 & 60 & 120 \\ 270 & 300 & 240 & 90 & 270 & 0 \\ 120 & 60 & 30 & 150 & 240 & 30 \\ 330 & 150 & 90 & 270 & 300 & 210 \\ 0 & 120 & 60 & 210 & 330 & 180 \end{bmatrix}[^\circ],$$

$$[8]\begin{bmatrix} 270 & 60 & 150 & 180 & 270 & 150 \\ 0 & 300 & 120 & 210 & 90 & 330 \\ 30 & 240 & 90 & 120 & 300 & 0 \\ 330 & 300 & 210 & 60 & 240 & 30 \\ 240 & 30 & 180 & 90 & 180 & 270 \\ 150 & 330 & 120 & 60 & 210 & 0 \end{bmatrix}[^\circ],\ [9]\begin{bmatrix} 270 & 330 & 240 & 180 & 330 & 60 \\ 90 & 300 & 90 & 300 & 0 & 210 \\ 150 & 270 & 240 & 210 & 120 & 30 \\ 120 & 180 & 30 & 150 & 270 & 150 \\ 30 & 210 & 330 & 240 & 120 & 180 \\ 60 & 0 & 60 & 0 & 300 & 90 \end{bmatrix}[^\circ],$$

$$[10]\begin{bmatrix} 300 & 90 & 240 & 210 & 60 & 270 \\ 180 & 150 & 180 & 0 & 30 & 120 \\ 330 & 60 & 240 & 30 & 60 & 90 \\ 120 & 30 & 0 & 300 & 150 & 330 \\ 270 & 0 & 270 & 240 & 210 & 120 \\ 330 & 150 & 210 & 90 & 300 & 180 \end{bmatrix}[^\circ].$$

70% crystallinity:

$$[11]\begin{bmatrix} 60 & 180 & 150 & 90 & 60 & 330 \\ 210 & 0 & 30 & 270 & 300 & 0 \\ 150 & 120 & 240 & 300 & 30 & 270 \\ 300 & 210 & 150 & 240 & 90 & 120 \\ 270 & 120 & 0 & 30 & 210 & 240 \\ 330 & 90 & 60 & 180 & 330 & 180 \end{bmatrix}[^\circ],\ [12]\begin{bmatrix} 270 & 180 & 120 & 0 & 300 & 210 \\ 0 & 210 & 60 & 90 & 150 & 330 \\ 300 & 240 & 120 & 270 & 240 & 30 \\ 330 & 30 & 90 & 120 & 180 & 270 \\ 150 & 240 & 60 & 90 & 60 & 300 \\ 330 & 30 & 210 & 180 & 150 & 0 \end{bmatrix}[^\circ],$$

$$[13]\begin{bmatrix} 270 & 90 & 300 & 120 & 30 & 60 \\ 0 & 210 & 330 & 240 & 150 & 180 \\ 30 & 120 & 90 & 270 & 300 & 330 \\ 0 & 300 & 240 & 210 & 30 & 210 \\ 180 & 240 & 150 & 330 & 270 & 0 \\ 60 & 150 & 60 & 90 & 120 & 180 \end{bmatrix}[^\circ],\ [14]\begin{bmatrix} 30 & 120 & 330 & 240 & 300 & 330 \\ 270 & 0 & 60 & 270 & 150 & 0 \\ 180 & 150 & 210 & 120 & 90 & 30 \\ 90 & 300 & 240 & 180 & 210 & 180 \\ 330 & 210 & 120 & 60 & 90 & 60 \\ 240 & 300 & 30 & 150 & 0 & 270 \end{bmatrix}[^\circ],$$

$$[15]\begin{bmatrix} 330 & 90 & 210 & 120 & 330 & 0 \\ 180 & 30 & 180 & 270 & 300 & 60 \\ 120 & 90 & 300 & 240 & 150 & 0 \\ 150 & 240 & 270 & 210 & 60 & 90 \\ 60 & 270 & 300 & 30 & 240 & 120 \\ 0 & 30 & 330 & 150 & 210 & 180 \end{bmatrix}[^\circ].$$

B Obtained pole figures in elastic regime

In this appendix, the pole figure results are shown which are obtained with purely elastic simulations. Figures B.1 - B.4 are obtained with the multi-scale finite element model, with a crystallinity of 60% and matrix of orientations seven (see Appendix A). Figures B.5 - B.8 are obtained with the composite inclusion model for 60% crystallinity. Figures B.9 - B.12 are obtained with the multi-scale finite element model, with a crystallinity of 70% and matrix of orientations 11. Figures B.13 - B.16 are obtained with the composite inclusion model for 70% crystallinity.

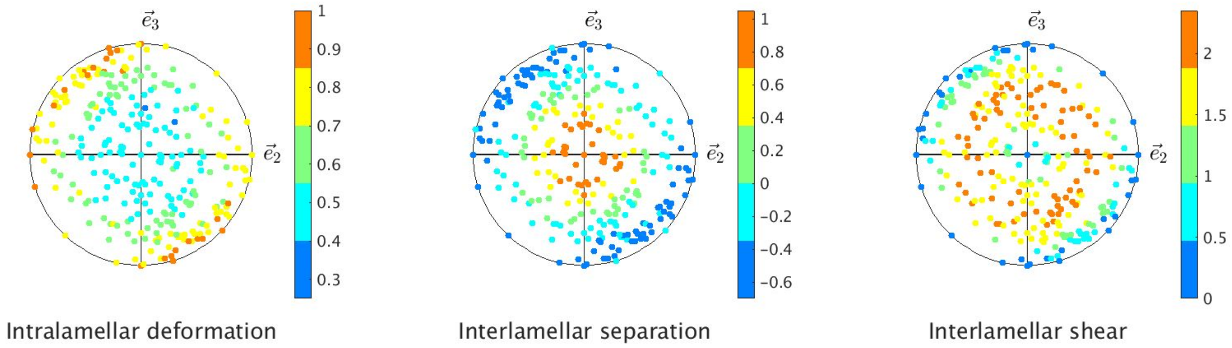

Intralamellar deformation Interlamellar separation Interlamellar shear

Figure B.1: Pole figure obtained with multi-scale finite element model, matrix of orientations 6, 60% crystallinity and fold plane $(10\bar{6})$.

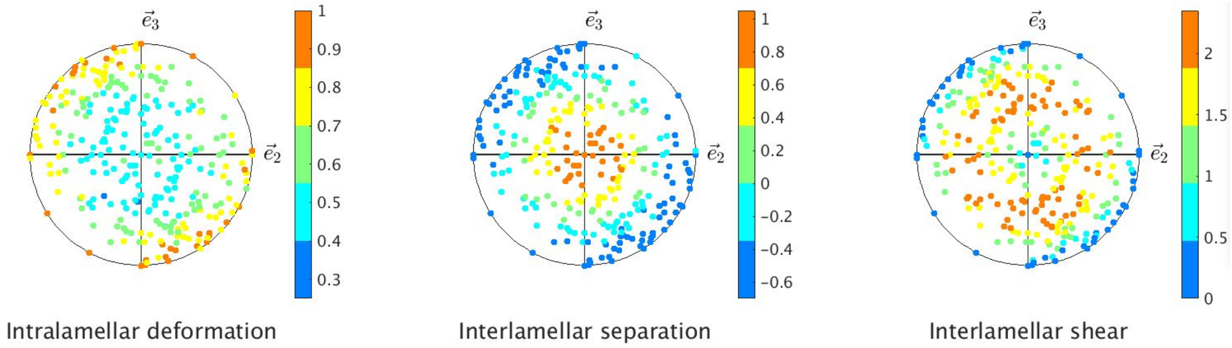

Intralamellar deformation Interlamellar separation Interlamellar shear

Figure B.2: Pole figure obtained with multi-scale finite element model, matrix of orientations 6, 60% crystallinity and fold plane (001).

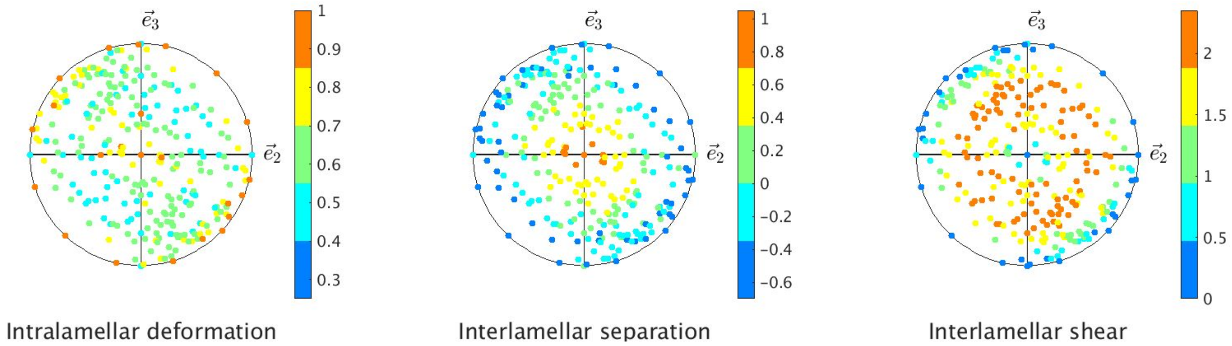

Intralamellar deformation Interlamellar separation Interlamellar shear

Figure B.3: Pole figure obtained with multi-scale finite element model, matrix of orientations 6, 60% crystallinity and fold plane (010).

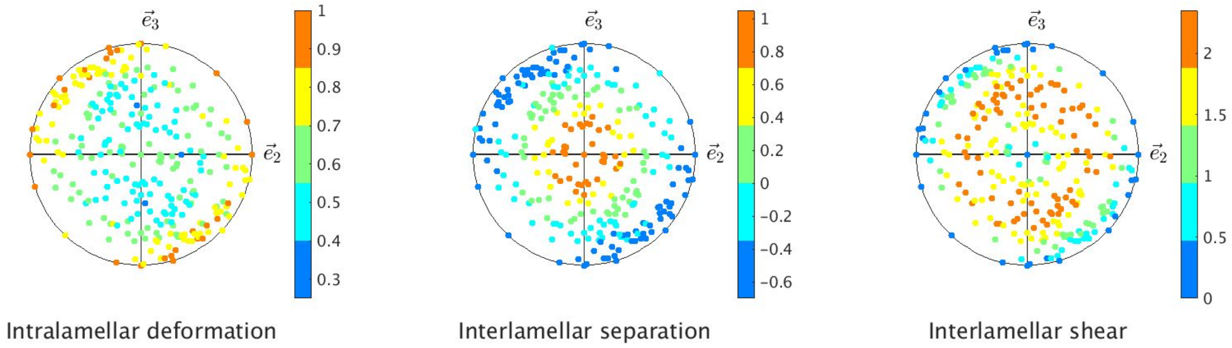

Intralamellar deformation Interlamellar separation Interlamellar shear

Figure B.4: Pole figure obtained with multi-scale finite element model, matrix of orientations 6, 60% crystallinity and fold plane $(1\,\bar{1}\bar{1}\,\bar{6})$.

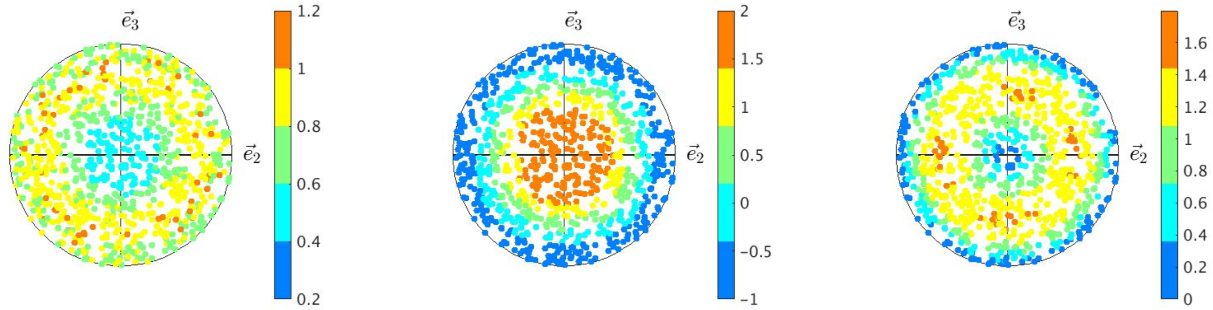

Intralamellar deformation Interlamellar separation Interlamellar shear

Figure B.5: Pole figure obtained with composite inclusion model, 60% crystallinity and fold plane $(10\bar{6})$.

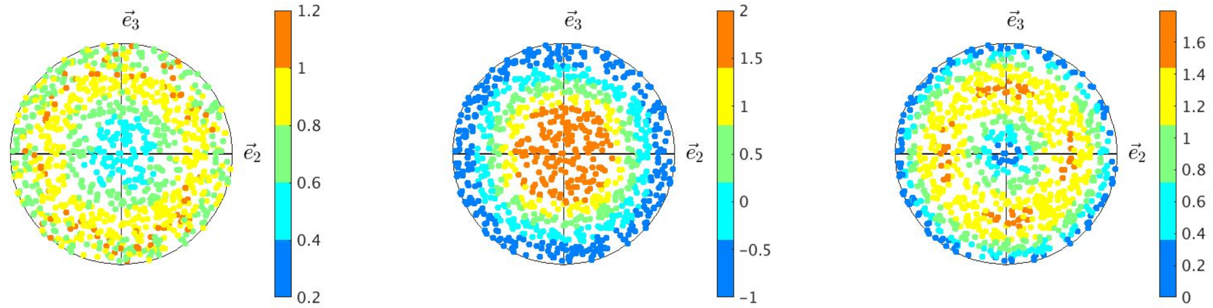

Intralamellar deformation Interlamellar separation Interlamellar shear

Figure B.6: Pole figure obtained with composite inclusion model, 60% crystallinity and fold plane (001).

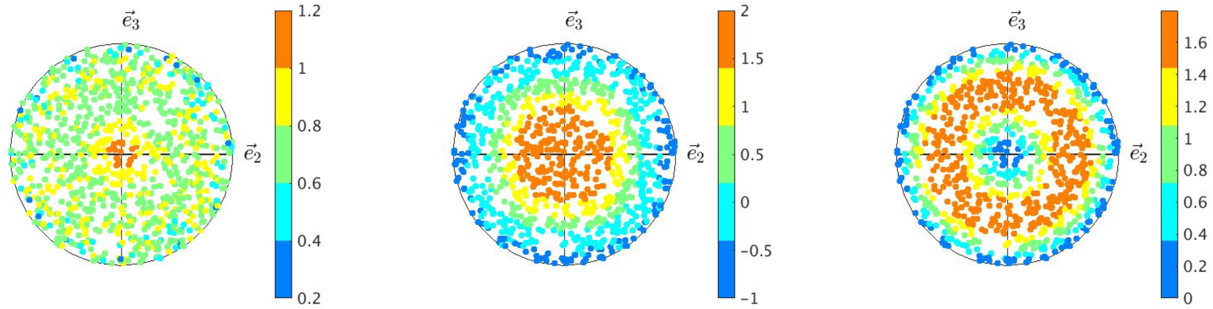

Intralamellar deformation Interlamellar separation Interlamellar shear

Figure B.7: Pole figure obtained with composite inclusion model, 60% crystallinity and fold plane (010).

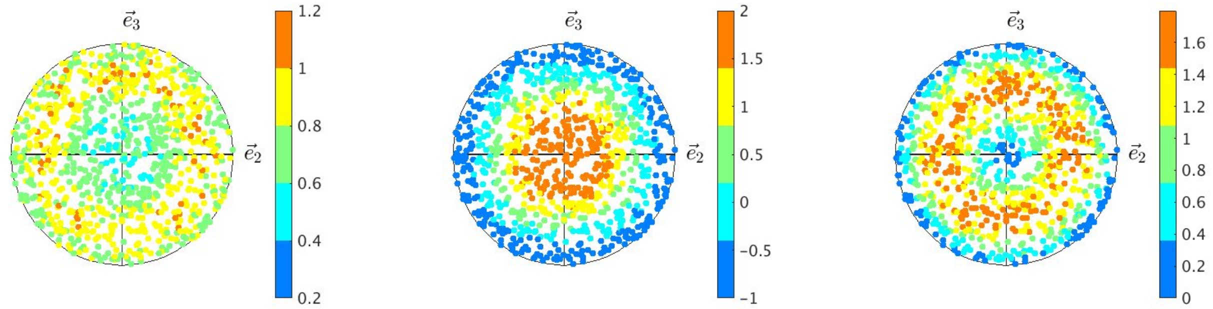

Intralamellar deformation Interlamellar separation Interlamellar shear

Figure B.8: Pole figure obtained with composite inclusion model, 60% crystallinity and fold plane $(1\,\bar{1}\,\bar{6})$.

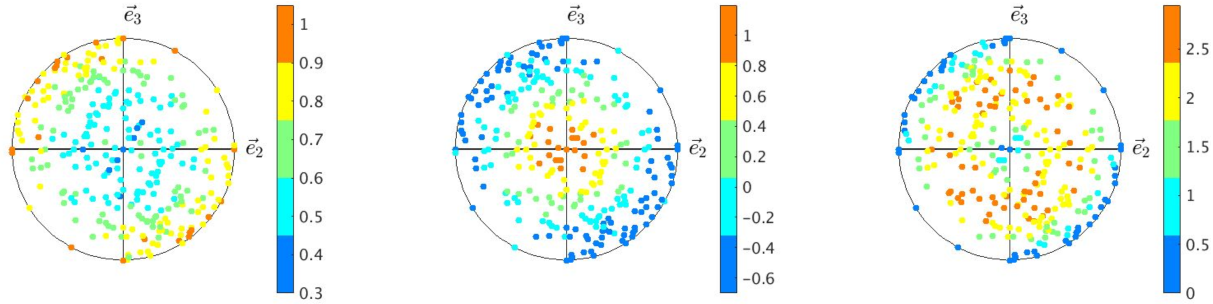

Intralamellar deformation Interlamellar separation Interlamellar shear

Figure B.9: Pole figure obtained with multi-scale finite element model, matrix of orientations 11, 70% crystallinity and fold plane (10$\bar{6}$).

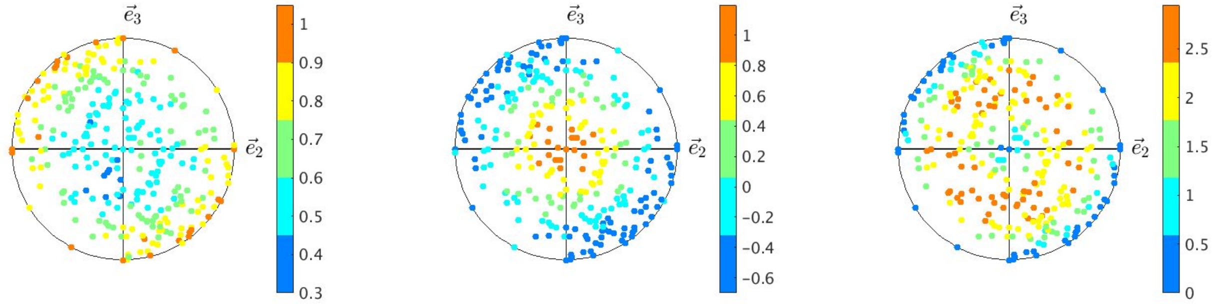

Intralamellar deformation Interlamellar separation Interlamellar shear

Figure B.10: Pole figure obtained with multi-scale finite element model, matrix of orientations 11, 70% crystallinity and fold plane (001).

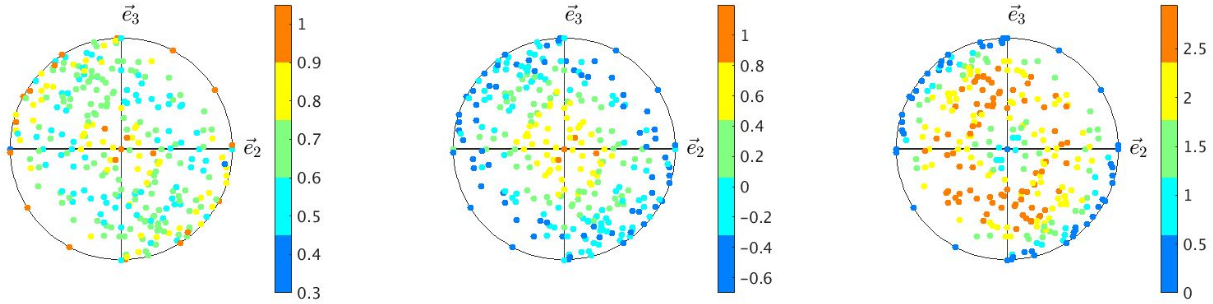

Intralamellar deformation Interlamellar separation Interlamellar shear

Figure B.11: Pole figure obtained with multi-scale finite element model, matrix of orientations 11, 70% crystallinity and fold plane (010).

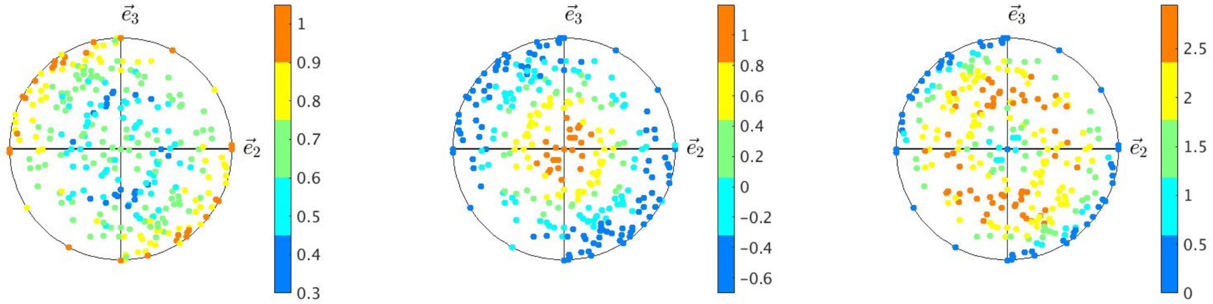

Intralamellar deformation Interlamellar separation Interlamellar shear

Figure B.12: Pole figure obtained with multi-scale finite element model, matrix of orientations 11, 70% crystallinity and fold plane (1 $\bar{1}$ $\bar{6}$).

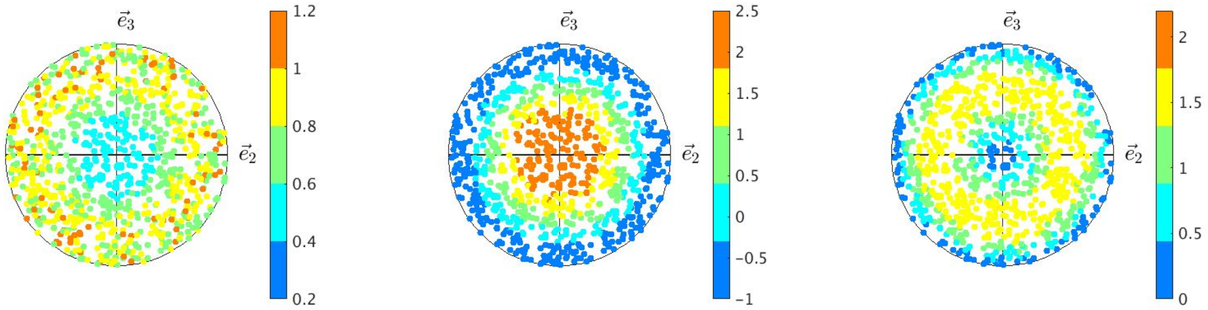

Intralamellar deformation Interlamellar separation Interlamellar shear

Figure B.13: Pole figure obtained with composite inclusion model, 70% crystallinity and fold plane $(10\bar{6})$.

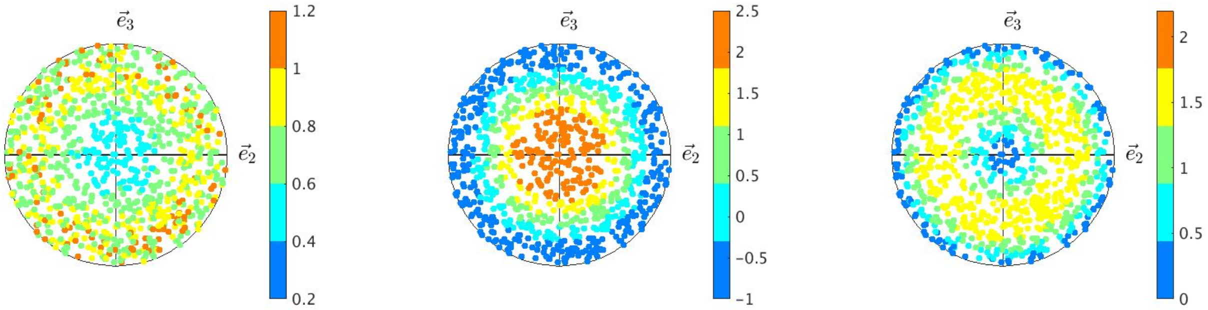

Intralamellar deformation Interlamellar separation Interlamellar shear

Figure B.14: Pole figure obtained with composite inclusion model, 70% crystallinity and fold plane (001).

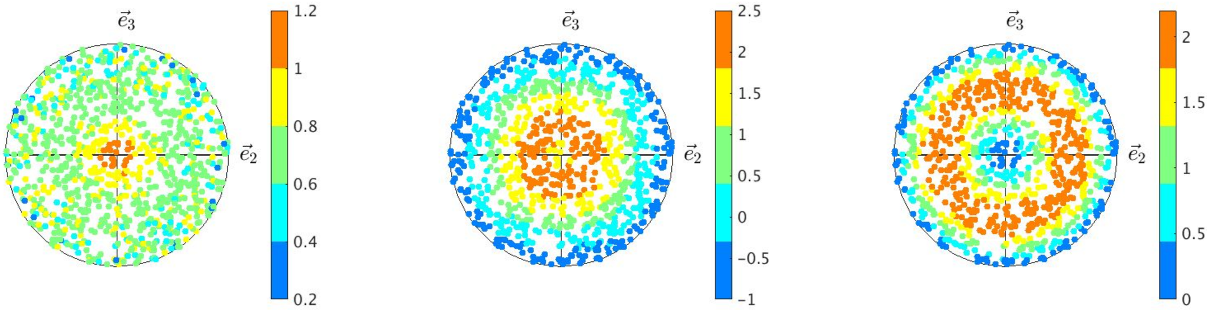

Intralamellar deformation Interlamellar separation Interlamellar shear

Figure B.15: Pole figure obtained with composite inclusion model, 70% crystallinity and fold plane (010).

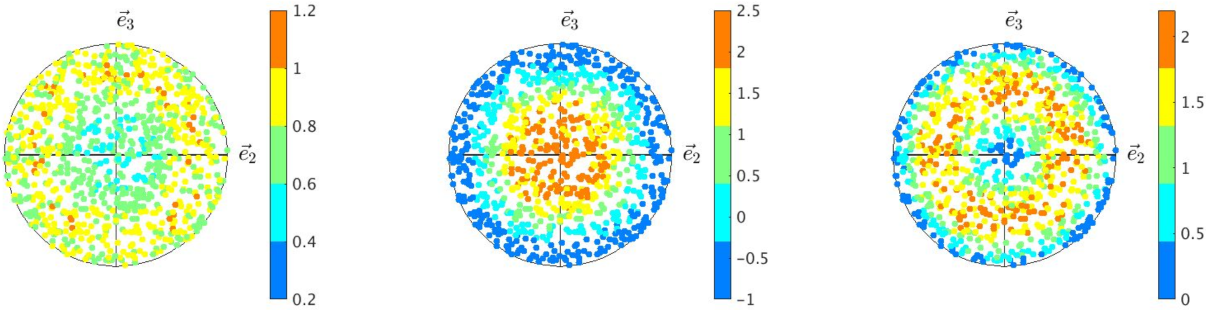

Intralamellar deformation Interlamellar separation Interlamellar shear

Figure B.16: Pole figure obtained with composite inclusion model, 70% crystallinity and fold plane $(1\ \bar{1}1\ \bar{6})$.

C Elasto-viscoplastic results

In this appendix, obtained elasto-viscoplastic results during the project are shown.

Table 7 shows the obtained yield stresses for a micro RVE with matrix of orientations one, 50% crystallinity and for all fold planes. These are the yield stresses that are used in the spherulite model for the Hill yield criterion. They are determined as shown in Figures C.1 - C.4.

Table 7: Obtained yield stresses for each fold plane.

Fold plane	$\boldsymbol{\sigma_{xx}}$ [MPa]	$\boldsymbol{\sigma_{yy}}$ [MPa]	$\boldsymbol{\sigma_{zz}}$ [MPa]	$\boldsymbol{\sigma_{yz}}$ [MPa]	$\boldsymbol{\sigma_{xz}}$ [MPa]	$\boldsymbol{\sigma_{xy}}$ [MPa]
$(10\bar{6})$	46.07	45.08	71.44	14.6	14.74	17.95
(001)	44.43	45.13	68.35	14.69	14.84	16.2
(010)	50.33	60.34	76.08	14.6	14.74	17.71
$(1\,\bar{1}1\,\bar{6})$	34.58	34.91	68.8	14.94	15.03	15.28

For the $(10\bar{6})$ fold plane in Figure C.1, the load cases with xx, yx and yy deformation crashed. However, the simulations proceeded far enough to determine the yield stresses. The same holds for the (001) fold plane as shown in Figure C.2. The (010) fold plane, as shown in Figure C.3 crashed for the xx, yx, yy and zz load cases, where the xx, yy and zz load cases proceeded far enough to determine the yield stresses. The determined σ_{yx} yield stress is questionable. However, it is assumed that in the worst case scenario there is no large error in this calculated yield stress. The $(1\,\bar{1}1\,\bar{6})$ fold plane, as shown in Figure C.4 did not have any load cases that crashed.

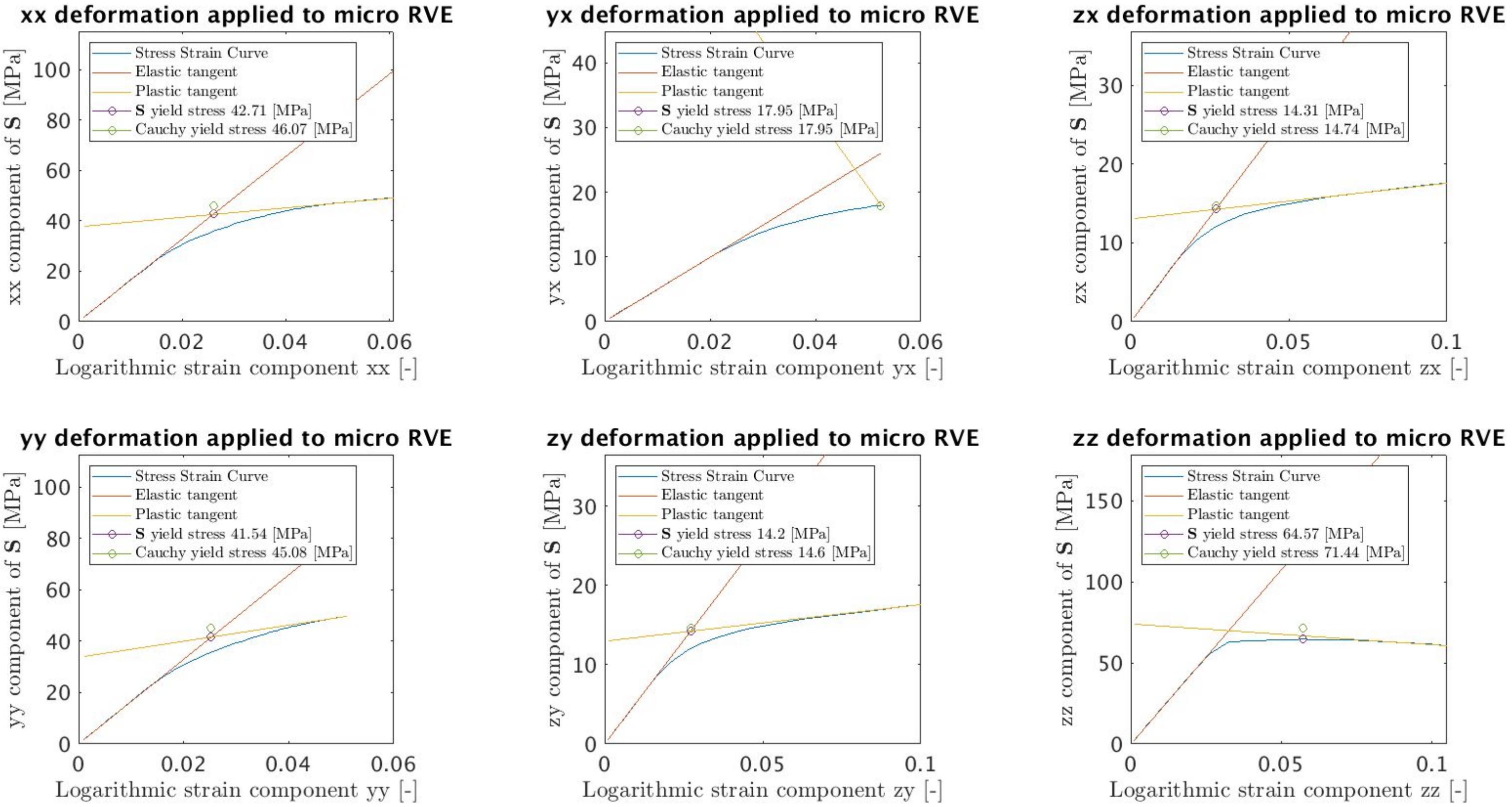

Figure C.1: Obtained yield stresses for the $(10\bar{6})$ fold plane.

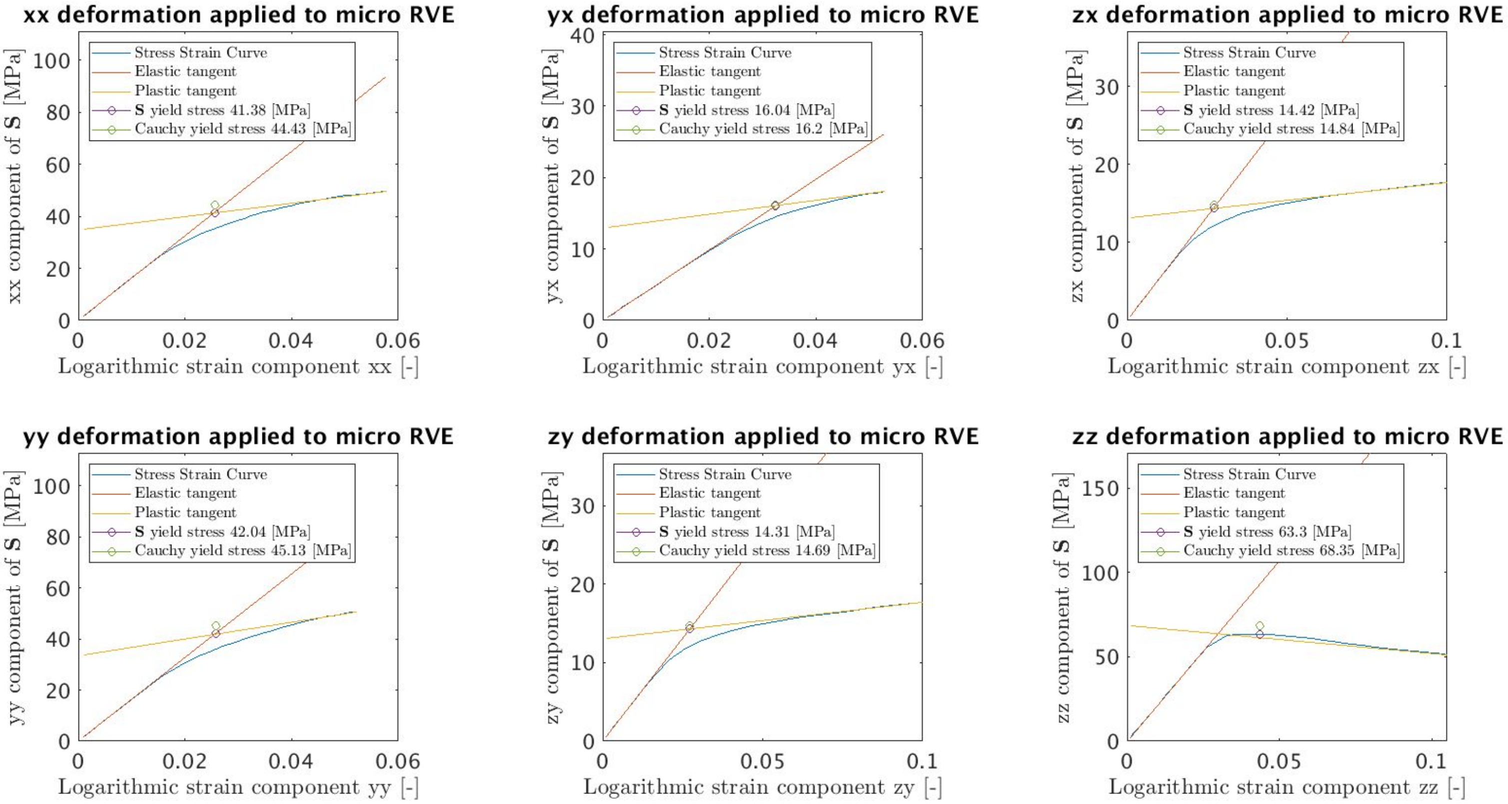

Figure C.2: Obtained yield stresses for the (001) fold plane.

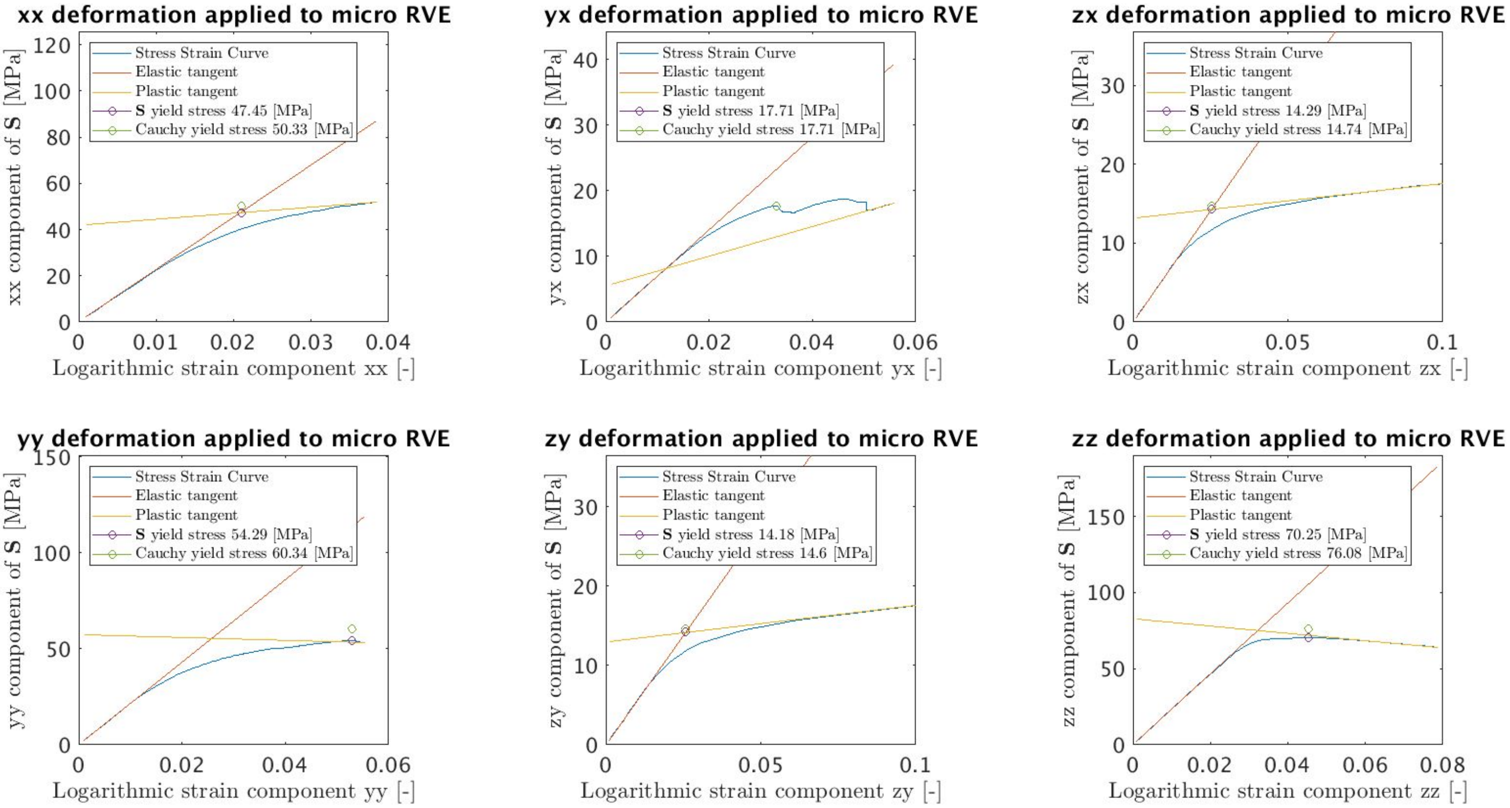

Figure C.3: Obtained yield stresses for the (010) fold plane.

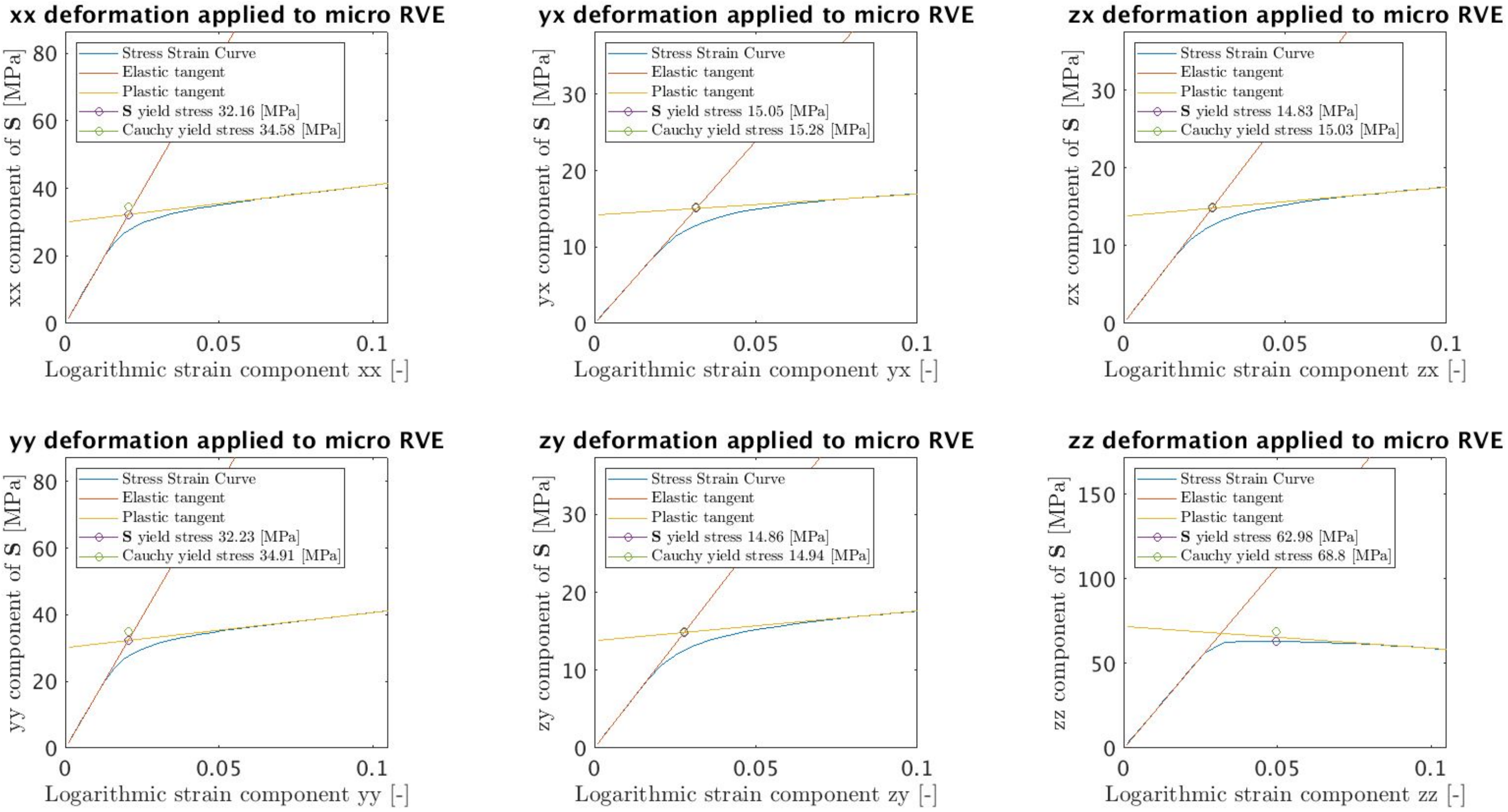

Figure C.4: Obtained yield stresses for the $(1\,\bar{1}\bar{1}\,\bar{6})$ fold plane.

D Eyring slip law

In this appendix, the derivations to replace the power law, which describes the slip kinetics, by an Eyring slip law are discussed. For additional information have a look at [18]. The power-law implemented in the crystal plasticity model [18] by default is:

$$\dot{\gamma}^\alpha = \dot{\gamma}_0 \left(\frac{\left| \tau^\alpha_{eff} \right|}{s^\alpha} \right)^{\frac{1}{m}} sign(\tau^\alpha_{eff}), \tag{D.1}$$

where $\dot{\gamma}^\alpha$ is the slip rate, $\dot{\gamma}_0$ the initial slip rate, τ^α_{eff} the effective resolved shear stress, s^α the slip resistance (including hardening), α the slip system and m a fitting parameter. The effective resolver shear stress is defined as follows:

$$\tau^\alpha_{eff} = \tau^\alpha - \tau^\alpha_{back}, \tag{D.2}$$

where τ^α is the resolved shear stress and τ^α_{back} the resolved back stress. In this project the resolved back stress is zero due to the chosen crystal plasticity model simulation settings (no strain gradient crystal plasticity), i.e. $\tau^\alpha_{eff} = \tau^\alpha$.

In this project, the power-law shown in Equation D.1 is replaced by the Eyring slip law:

$$\dot{\gamma}^\alpha = \dot{\gamma}^\alpha_0 sinh \left(\frac{\tau^\alpha}{\tau^\alpha_0} \right), \tag{D.3}$$

where τ^α_0 is the slip resistance excluding hardening, i.e. no hardening is taken into account.

To calculate the residual, the power-law as shown in Equation D.1 is used as shown in red:

$$r^\alpha = \Delta\gamma^\alpha - \frac{\Delta t}{2} \left(\dot{\gamma}^\alpha(t_n) + \dot{\gamma}_0 \left(\frac{\left| \tau^\alpha_{eff} \right|}{s^\alpha} \right)^{\frac{1}{m}} sign(\tau^\alpha_{eff}) \right), \tag{D.4}$$

where $\Delta\gamma^\alpha$ is the slip increment and Δt the timestep. In here, the power-law could be directly replaced by the Eyring slip shown in Equation D.3.

To calculate the variational form of the residual, the derivative of the power-law with respect to γ is used, with the power-law derivative shown in red:

$$\delta r^\alpha = \delta\Delta\gamma^\alpha - \frac{\Delta t}{2} \left(\frac{1}{(s^\alpha)^2} \frac{\dot{\gamma}_0}{m} \left(\frac{\left| \tau^\alpha_{eff} \right|}{s^\alpha} \right)^{\frac{1}{m}-1} \right) \left(s^\alpha \delta\tau^\alpha_{eff} - \tau^\alpha_{eff} \delta s^\alpha \right). \tag{D.5}$$

The red part of Equation D.5 is replaced by the derivative of the Eyring slip law with respect to γ, leading to the following, where the part in red is the derivative of Eyring slip law as shown in Equation D.3:

$$\delta r^\alpha = \delta\Delta\gamma^\alpha - \frac{\Delta t}{2} \left(\frac{\dot{\gamma}_0}{(s^\alpha)^2} cosh \left(\frac{\tau^\alpha}{\tau^\alpha_0} \right) \right) \left(s^\alpha \delta\tau^\alpha_{eff} - \tau^\alpha_{eff} \delta s^\alpha \right). \tag{D.6}$$

Finally, the derivative of the power-law is used in the calculation of the Jacobian matrix $\underline{K}$, as shown in red:

$$\underline{K} = \frac{\partial r}{\partial\Delta\gamma} = \underline{I} + \frac{\Delta t}{2} \left(\frac{1}{(s^a)^2} \frac{\dot{\gamma}_0}{m} \left(\frac{\left| \tau^\alpha_{eff} \right|}{s^\alpha} \right)^{\frac{1}{m}-1} \right) \left(\tau^\alpha_{eff} \frac{\partial s^\alpha}{\partial\Delta\gamma} - s^\alpha \frac{\partial\tau^\alpha_{eff}}{\partial\Delta\gamma} \right), \tag{D.7}$$

where $\underline{I}$ is the identity matrix. The red part in Equation D.7 is replaced by the red part of Equation D.6, which is the derivative of the Eyring slip law.

E Investigation on convergence problems

In this appendix, the investigation on the convergence problems in the elasto-viscoplastic simulations is discussed. First, a convergence study is discussed, which is used to isolate the problem. Next, the Total & Updated Lagrange solution procedures are compared to get a better idea on why there are convergence problems.

When the crystal plasticity model was implemented in the multi-scale finite element model, the final simulations were performed. It turned out that only the $(1\,\bar{1}1\,\bar{6})$ fold plane was able to perform 100% of the loadcase for all six deformations. In certain simulations of the other fold planes, at a certain progress of the loadcase, Marc can no longer find a converged solution. Therefore, Marc keeps decreasing the timestep, until the timestep becomes too small and then stops the simulation. It was observed that the convergence behavior was different in test cases with less elements. Therefore, test cases are used with the same mesh that is used in simulations to obtain final results. These test cases are discussed next.

E.1 Convergence study

First, the convergence study is discussed. Here it is discussed which test cases are used to determine the convergence problem. First, the convergence of these test cases is shown in Figures E.1a - E.1c and after that they are discussed.

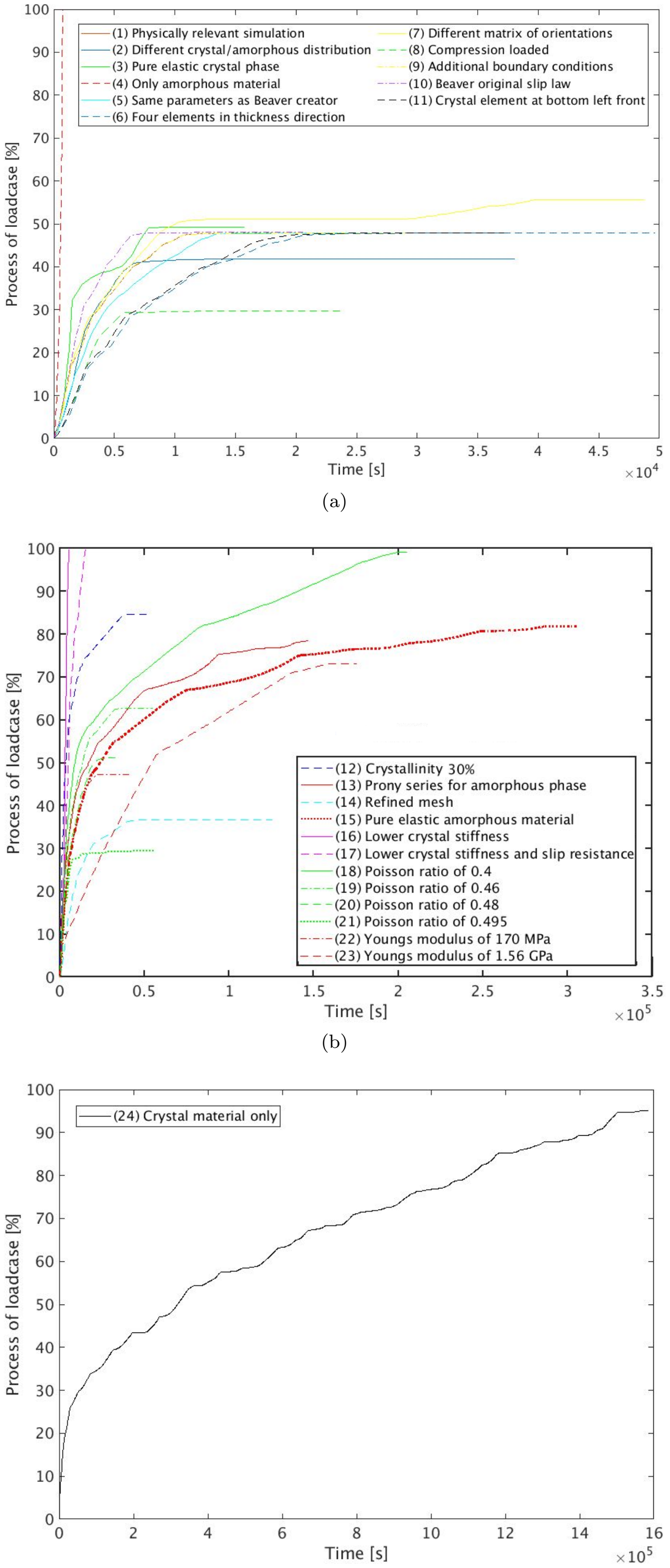

(a)

(b)

(c)

Figure E.1: Convergence study of a micro RVE, with 50% crystallinity and the $(10\bar{6})$ fold plane, where deformation in x-direction is applied. With (a) test cases 1-11, (b) test cases 12-23 and (c) test case 24.

It is difficult to see, but the Physically relevant simulation, from which final results should have been obtained, crashes at approximately 48% of the loadcase as shown in Figure E.1a. So, test cases are performed to see what causes the simulations to crash at higher/lower % of the loadcase. First, each loadcase is explained more elaborate.

1. (1): This is the simulation with which the final results should have been obtained with Mesh 1 as shown in Figure E.2. All other test cases also make use of this mesh, unless mentioned otherwise.
2. (2): Mesh 3 as shown in Figure E.2 is used.
3. (3): The crystalline phase is purely elastic.
4. (4): Only amorphous material is used.
5. (5): Certain parameters in the job.dat file are set identical to a file of the Beaver creator(s).
6. (6): Four instead of two elements are used in thickness direction.
7. (7): Mesh 2 as shown in Figure E.2 is used.
8. (8): Compression in x-direction instead of tension.
9. (9): The node at the bottom left corner in the mid plane is also fixed in x and y-direction.
10. (10): The originally implemented slip law of Beaver is used.
11. (11): The element at the bottom left front corner is changed to a crystal element.
12. (12): 30% crystallinity instead of 50%.
13. (13): Amorphous material behavior is based on the Prony series (i.e. a different material model).
14. (14): A finer mesh (four times more elements) is used.
15. (15): Amorphous material is purely elastic.
16. (16): Crystal stiffness is reduced by a factor of 10.
17. (17): Crystal stiffness is reduced by a factor of 10, $\dot{\gamma}_0$ increased by factor of 10.000 to increase amount of slip.
18. (18): Poisson ratio of 0.4 instead of 0.486.
19. (19): Poisson ratio of 0.46 instead of 0.486.
20. (20): Poisson ratio of 0.48 instead of 0.486.
21. (21): Poisson ratio of 0.495 instead of 0.486.
22. (22): Young's modulus of 170 MPa.
23. (23): Young's modulus of 1.56 GPa.
24. (24): Only crystalline material.

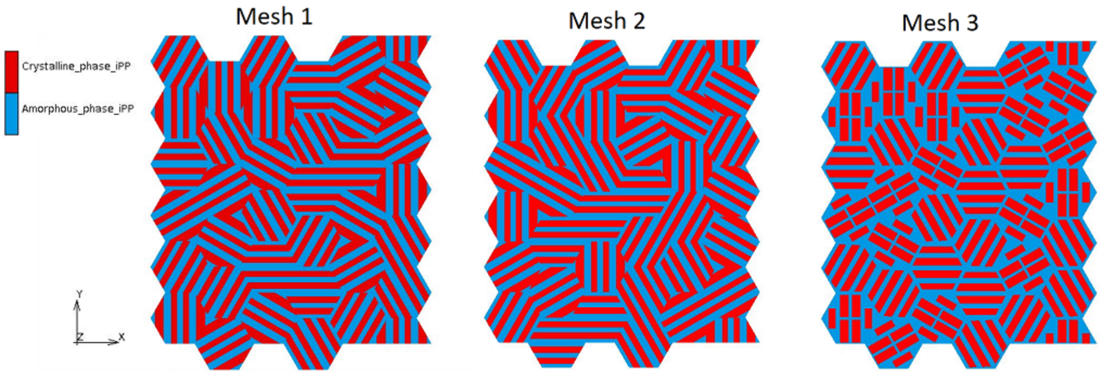

Figure E.2: Three different meshes which are used for the convergence study. Mesh one is used in all test cases, unless mentioned otherwise.

Not all test cases will be discussed. Only a couple will be discussed to explain what is causing the convergence problems.

Test cases 1 (physically relevant), 4 (only amorphous material) and 24 (only crystal material) together show that there is an issue due to the combination of the amorphous and crystalline material models. Test case one crashes at 48%, test case 4 does not crash and test case 24 crashes at 94%. However, the reason test case 24 crashes is due to the convergence of the slip systems in the crystal plasticity model, instead of Marc reducing the timestep. This will be no problem for α-iPP simulations because the crystal phase will be loaded less due to the presence of the amorphous phase which is less stiff.

So, there is an issue when the two different material models are combined. Next, Figure E.1b holds the most important conclusions on what most likely is the problem. The most obvious one is that the lower the Poisson ratio, the later the simulations crashes (see test case 18, 19, 20 and 21). Test cases 22 and 23 show that that increasing the Young's Modulus for the amorphous phase is also favorable. Increasing the Young's modulus leads to less contractions due to the Poisson ratio. Reducing the stiffness of the crystalline material (test cases 16 and 17) is also favorable. As the crystal material deforms more, the amorphous material deforms less i.e. there is again less traction due to the Poisson ratio. So, there is a strong indication that material contractions are the problem. This will be explained more elaborate in the next section.

E.2 Total Lagrange procedure vs Updated Lagrange procedure

Marc mentions that one should use the Updated Lagrange procedure for large strain plasticity (which is the case in this project), but not that one must use it. Also, it mentions that both the updated Lagrange & Total Lagrange procedures should yield the exact same results if implemented correctly.

However, Marc uses Cauchy stress and Logarithmic strains when the updated Lagrange procedure is used. When the total Lagrange procedure is used, Marc uses Second Piola-Kirchhoff stress and Green-Lagrange strain. This means that when one uses the total Lagrange procedure, there is a lot of volumetric strain, depending on the Poisson ratio. When the updated Lagrange procedure is used, there is almost no volumetric strain. This is shown in Figure E.3, for a Poisson ratio of 0.486 [-].

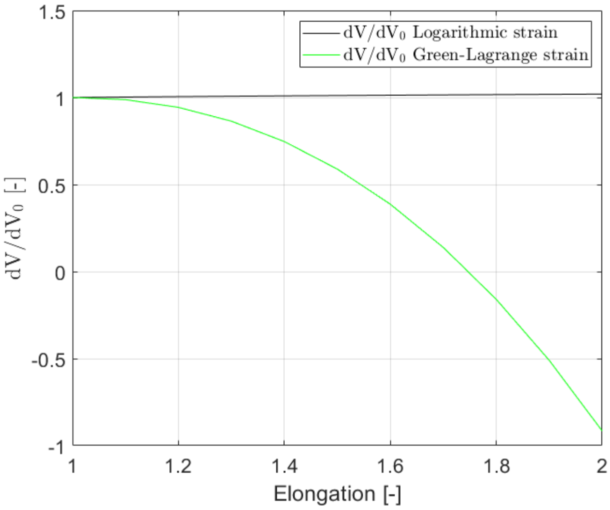

Figure E.3: Volumetric strain as a function of elongation, with a Poisson ratio of 0.486. With in green, the total Lagrange procedure, i.e. Green-Lagrange strain and in black, the updated Lagrange, i.e. Logarithmic strain.

So, with the total Lagrange and updated Lagrange procedures in Marc, different results are obtained. This has been confirmed in a simple test case with a single element, where with large strain, the volume of the element in the total Lagrange procedure became 0, as shown in Figure E.4a, which did not happen with the updated Lagrange procedure, as shown in Figure E.4b. Also, it is not possible to rewrite Cauchy stress to second Piola-Kirchhoff stress, or the other way around. Earlier, it is shown that the problems most likely occur due to material contractions. As shown in Figures E.4a and E.4b, the updated Lagrange procedure leads to less contraction. This implies the need of the updated Lagrange procedure instead of total Lagrange procedure, on which the crystal plasticity model works, to simulate large strain plasticity.

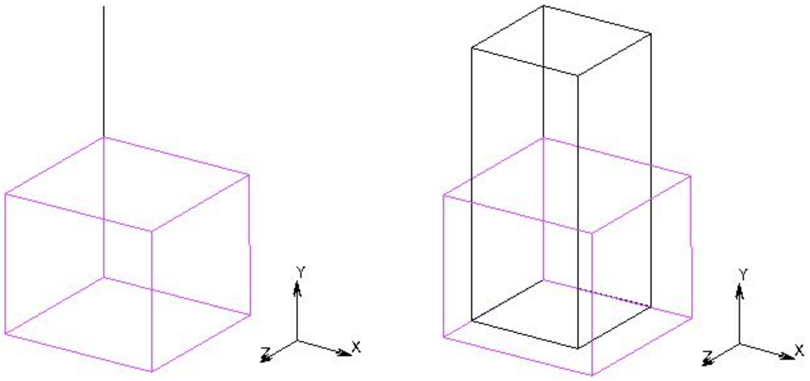

(a) (b)

Figure E.4: Two identical test cases with a single element. The only difference is that in (a) the total Lagrange procedure is used and in (b) the updated Lagrange procedure. In purple and black the undeformed the deformed states are shown respectively.

This means that the crystal plasticity model must be modified such that it also works on the updated Lagrange procedure. However, this is complicated and the status on this is shown in Appendix F.

F Combining the crystal plasticity model and EGP-model

In this appendix, the status of changing the crystal plasticity model (CPM) from the total Lagrange procedure to the Updated Lagrange procedure is discussed. It was tried to change the crystal plasticity model to the updated Lagrange procedure to enable the combination of the crystal plasticity model and EGP-model in Marc. Later in the project, it became clear that the multi-scale finite element model suffered from convergence problems on the total Lagrange procedure, when simulating large strain plasticity. Therefore, the crystal plasticity model has to be modified such that it works with the updated Lagrange procedure. Due to time issues it was not possible to finish this during this project.

Both models work on the Hypela2 user-subroutine. To combine the models, a modified version of Hypela2, named MD_Hypela2 can be used. In this modified version, additional input parameters are used [32]. However, these extra parameters can be ignored, such that the exact same results as with the Hypela2 user-subroutine are obtained. The only catch here is that the extra parameter called "nstats" must be given a different name because the crystal plasticity model uses that parameter name as well, making them clash. By using both these user-subroutines, both the crystal plasticity model and EGPM can be used together in an easy way.

For the updated Lagrange method, Marc works with the Cauchy stress and Logarithmic strain. For the total Lagrange method Marc works with the second Piola-Kirchhoff stress and Green-Lagrange strain. This has to be taken into account with the input and output of (MD_)Hypela2.

Rewriting input parameters

Hypela2 gets a different deformation gradient tensor $\boldsymbol{F}$ as input depending on the solution procedure (updated Lagrange or total Lagrange). However, this is because the results between both procedures differ because Marc uses different stresses and strains in both solution procedures. So, $\boldsymbol{F}$ should not be adjusted.

Rewriting output parameters

The required output from the user-subroutines are:

1. Stress-strain law to be formed
2. Change in stress due to temperature effects
3. Stress

Where the change in stress due to temperature effects can be ignored, because during this project this is not taken into account.

Rewriting stress output

Rewriting the stress from second Piola-Kirchhoff stress to Cauchy stress is straight forward:

$$\boldsymbol{\sigma} = \frac{\boldsymbol{F}\boldsymbol{S}\boldsymbol{F}^T}{J}, \tag{F.1}$$

where $\boldsymbol{\sigma}$ is the Cauchy stress, $\boldsymbol{F}$ the deformation gradient tensor, $\boldsymbol{S}$ the second Piola-Kirchhoff stress tensor and J the determinant of $\boldsymbol{F}$. The new stress calculation is validated in a single element test case. By fixing all degrees of freedom, this element is once deformed by simple shear and once by uni-axial strain. The stress results are then compared to the same test cases, but with a Marc material model, which described the material behavior in the same way. Since both models have the same stress output, it is known that the stress calculation is correctly adjusted.

Rewriting stress-strain law output

The most difficult part is to rewrite the stress-strain law. Here, Marc requires the material tangent stiffness tensor (Marc automatically takes into account the geometrical tangent stiffness). In the crystal plasticity model [18] the material tangent stiffness is defined as follows:

$$
{}^{4}\boldsymbol{K} = \frac{\partial \boldsymbol{S}}{\partial \boldsymbol{E}}, \tag{F.2}
$$

where ${}^{4}\boldsymbol{K}$ is the material tangent stiffness tensor, $\boldsymbol{S}$ the second Piola-Kirchhoff stress tensor and $\boldsymbol{E}$ the Green-Lagrange strain tensor. When the solution procedure is changed to the updated Lagrange procedure, the material tangent stiffness changes [33]:

$$
{}^{4}\boldsymbol{K} = \frac{\partial \boldsymbol{\sigma}}{\partial \boldsymbol{\Lambda}}, \tag{F.3}
$$

where $\boldsymbol{\sigma}$ is the Cauchy stress tensor and $\boldsymbol{\Lambda}$ is the logarithmic strain tensor which is defined as $\boldsymbol{\Lambda} = ln(\boldsymbol{U})$, where $\boldsymbol{U}$ is the right stretch tensor. To simplify the derivation Equation F.3 is split:

$$
{}^{4}\boldsymbol{K} = \frac{\partial \boldsymbol{\sigma}}{\partial \boldsymbol{F}^{T}} : \frac{\partial \boldsymbol{F}}{\partial ln(\boldsymbol{U})}. \tag{F.4}
$$

First, the first intermediate term ($\frac{\partial \boldsymbol{\sigma}}{\partial \boldsymbol{F}^{T}}$) will be discussed. After that, the second intermediate term ($\frac{\partial \boldsymbol{F}}{\partial ln(\boldsymbol{U})}$) will be discussed. But first, for a better understanding of the derivations, Equations F.5 - F.7 are defined first.

$$
{}^{4}\boldsymbol{I} : \boldsymbol{Z} = \boldsymbol{Z} : {}^{4}\boldsymbol{I} = \boldsymbol{Z}, \tag{F.5}
$$

$$
{}^{4}\boldsymbol{I}^{RT} : \boldsymbol{Z} = \boldsymbol{Z}^{T}, \tag{F.6}
$$

$$
{}^{4}\boldsymbol{I}^{S} : \boldsymbol{Z} = \frac{1}{2}\left({}^{4}\boldsymbol{I} + {}^{4}\boldsymbol{I}^{RT}\right) : \boldsymbol{Z} = \frac{1}{2}\left(\boldsymbol{Z} + \boldsymbol{Z}^{T}\right) = \boldsymbol{Z}^{S}, \tag{F.7}
$$

where ${}^{4}\boldsymbol{I}$ is the fourth order identity tensor, ${}^{4}\boldsymbol{I}^{RT}$ the fourth order right transposed identity tensor and ${}^{4}\boldsymbol{I}^{S}$ the fourth order symmetrical identity tensor.

Cauchy stress derived w.r.t. deformation gradient tensor

The derivative of the Cauchy stress $\boldsymbol{\sigma}$ w.r.t. the deformation gradient tensor $\boldsymbol{F}$ is given as:

$$
\frac{d\boldsymbol{\sigma}}{d\boldsymbol{F}^{T}} = \frac{\partial \boldsymbol{\sigma}}{\partial \boldsymbol{S}^{T}} : \frac{\partial \boldsymbol{S}}{\partial \boldsymbol{F}^{T}} + \frac{\partial \boldsymbol{\sigma}}{\partial J}\frac{\partial J}{\partial \boldsymbol{F}^{T}} + \frac{\partial \boldsymbol{\sigma}}{\partial \boldsymbol{F}^{T}} : \frac{\partial \boldsymbol{F}}{\partial \boldsymbol{F}^{T}}. \tag{F.8}
$$

Which consists of three terms due to the product rule because both the second Piola-Kirchhoff stress tensor ($\boldsymbol{S}$) and determinant of the deformation gradient tensor (J) also depend on the deformation gradient tensor. Next, all six intermediate terms of Equation F.8 are derived from left to right.

Derivative of Cauchy stress w.r.t. the Second Piola-Kirchhoff stress

In this section, the $\frac{\partial \boldsymbol{\sigma}}{\partial \boldsymbol{S}^{T}}$ term is derived:

$$
\begin{aligned}
\delta\boldsymbol{\sigma} &= \frac{\boldsymbol{F}\cdot\delta\boldsymbol{S}\cdot\boldsymbol{F}^{T}}{J} \\
&= \frac{\boldsymbol{F}\cdot{}^{4}\boldsymbol{I}^{RT} : \left(\boldsymbol{F}\cdot\delta\boldsymbol{S}^{T}\right)}{J} \\
&= \frac{\boldsymbol{F}\cdot{}^{4}\boldsymbol{I}^{RT}\cdot\boldsymbol{F} : \delta\boldsymbol{S}^{T}}{J}.
\end{aligned} \tag{F.9}
$$

Which leads to the following result:

$$
\frac{\partial \boldsymbol{\sigma}}{\partial \boldsymbol{S}^{T}} = \frac{\boldsymbol{F}\cdot{}^{4}\boldsymbol{I}^{RT}\cdot\boldsymbol{F}}{J}. \tag{F.10}
$$

Derivative of second Piola-Kirchhoff stress w.r.t. the deformation gradient tensor

The derivation of $\frac{\partial \boldsymbol{S}}{\partial \boldsymbol{F}^{T}}$ can be found in Chapter 5.2 of [18]. Since this was initially implemented in the crystal plasticity model, this term could be used directly.

Derivative of Cauchy stress w.r.t. the determinant of the deformation gradient tensor

In this section, the $\frac{\partial \boldsymbol{\sigma}}{\partial J}$ term is derived. Since J is a scalar, the derivative of the Cauchy stress to J is straight forward:

$$\frac{\partial \boldsymbol{\sigma}}{\partial J} = \frac{\boldsymbol{F} \cdot \boldsymbol{S} \cdot \boldsymbol{F}^T}{-J^2}. \tag{F.11}$$

Derivative of determinant of the deformation gradient tensor w.r.t. the deformation gradient tensor

The derivation of $\frac{\partial J}{\partial \boldsymbol{F}^T}$ can be found in the lecture notes of the course 4MM10 (Advanced Computational Continuum Mechanics) [38], with the resulting variational form:

$$\delta J = J\boldsymbol{F}^{-T} : \delta \boldsymbol{F}^T. \tag{F.12}$$

Resulting in:

$$\frac{J}{\partial \boldsymbol{F}^T} = J\boldsymbol{F}^{-T}. \tag{F.13}$$

Derivative of Cauchy stress w.r.t. the deformation gradient tensor

In this section, the $\frac{\partial \boldsymbol{\sigma}}{\partial \boldsymbol{F}^T}$ term is derived:

$$\begin{aligned} \delta \boldsymbol{\sigma} &= \frac{\delta \boldsymbol{F} \cdot \boldsymbol{S} \cdot \boldsymbol{F}^T + \boldsymbol{F} \cdot \boldsymbol{S} \cdot \delta \boldsymbol{F}^T}{J} \\ &= \frac{{}^4\boldsymbol{I}^{RT} : \left(\boldsymbol{F} \cdot \boldsymbol{S}^T \cdot \delta \boldsymbol{F}^T\right) + {}^4\boldsymbol{I} : \left(\boldsymbol{F} \cdot \boldsymbol{S} \cdot \delta \boldsymbol{F}^T\right)}{J} \\ &= \frac{{}^4\boldsymbol{I}^{RT} \cdot \boldsymbol{F} \cdot \boldsymbol{S}^T : \delta \boldsymbol{F}^T + {}^4\boldsymbol{I} \cdot \boldsymbol{F} \cdot \boldsymbol{S} : \delta \boldsymbol{F}^T}{J} \\ &= \frac{\left({}^4\boldsymbol{I}^{RT} \cdot \boldsymbol{F} \cdot \boldsymbol{S}^T + {}^4\boldsymbol{I} \cdot \boldsymbol{F} \cdot \boldsymbol{S}\right) : \delta \boldsymbol{F}^T}{J}. \end{aligned} \tag{F.14}$$

Resulting in:

$$\frac{\partial \boldsymbol{\sigma}}{\partial \boldsymbol{F}^T} = \frac{{}^4\boldsymbol{I}^{RT} \cdot \boldsymbol{F} \cdot \boldsymbol{S}^T + {}^4\boldsymbol{I} \cdot \boldsymbol{F} \cdot \boldsymbol{S}}{J}. \tag{F.15}$$

Derivative the deformation gradient tensor w.r.t. the deformation gradient tensor

In this section, the $\frac{\partial \boldsymbol{F}}{\partial \boldsymbol{F}^T}$ term is derived:

$$\begin{aligned} \delta \boldsymbol{F} &= \delta \boldsymbol{F} \\ &= {}^4\boldsymbol{I}^{RT} : \delta \boldsymbol{F}^T. \end{aligned} \tag{F.16}$$

Resulting in:

$$\frac{\partial \boldsymbol{F}}{\partial \boldsymbol{F}^T} = {}^4\boldsymbol{I}^{RT}. \tag{F.17}$$

Deformation gradient tensor derived w.r.t. the logarithmic strain tensor

In this section, the $\frac{\partial \boldsymbol{F}}{\partial ln(\boldsymbol{U})}$ term is derived which is split:

$$\frac{\partial \boldsymbol{F}}{\partial ln(\boldsymbol{U})} = \frac{\partial \boldsymbol{F}}{\partial \boldsymbol{U}} : \frac{\partial \boldsymbol{U}}{\partial ln(\boldsymbol{U})}, \tag{F.18}$$

where $\boldsymbol{U} = \boldsymbol{U}^T$ is used. $\frac{\partial \boldsymbol{F}}{\partial \boldsymbol{U}}$ is derived in the crystal plasticity model documentation (page 9-10) leading to the following result:

$$\frac{\partial \boldsymbol{F}}{\partial \boldsymbol{U}} = \boldsymbol{R} \cdot {}^4\boldsymbol{I}^S, \tag{F.19}$$

where the rotation tensor $\boldsymbol{R}$ is considered a constant and the fourth order symmetric identity tensor ${}^4\boldsymbol{I}^S$ is used because $\boldsymbol{U}$ is a symmetric tensor [39]. Next, following [39], the derivation of the final term $\frac{\partial \boldsymbol{U}}{\partial ln(\boldsymbol{U})}$ is shown:

$$\frac{\partial \boldsymbol{U}}{\partial ln(\boldsymbol{U})} = \sum_{i,j=1}^{s_e} G_{ij} \boldsymbol{P}_i \otimes \boldsymbol{P}_j, \tag{F.20}$$

where s_e is the number of unique eigenvalues, $\boldsymbol{P}$ the eigenprojection tensor of $\boldsymbol{U}$ and G a matrix containing the derivatives of the eigenvalues of $\boldsymbol{U}$. More specifically, G and $\boldsymbol{P}$ are shown next:

$$G_{ij} = \begin{cases} g'(\lambda_i) & \text{if i = j} \\ \frac{g(\lambda_i)-g(\lambda_j)}{\lambda_i-\lambda_j} & \text{if i} \neq \text{j} \end{cases}, \tag{F.21}$$

$$\boldsymbol{P}_i = \delta_{1M} \boldsymbol{I} \prod_{j=1, j\neq i}^{M} \frac{\boldsymbol{U} - \lambda_j \boldsymbol{I}}{\lambda_i - \lambda_j}, i = 1, 2, ..., M, \tag{F.22}$$

where λ is the eigenvalue of $\boldsymbol{U}$, δ_{1M} the Dirac delta which equals one if M equals one and M is the number of simple eigenvalues.

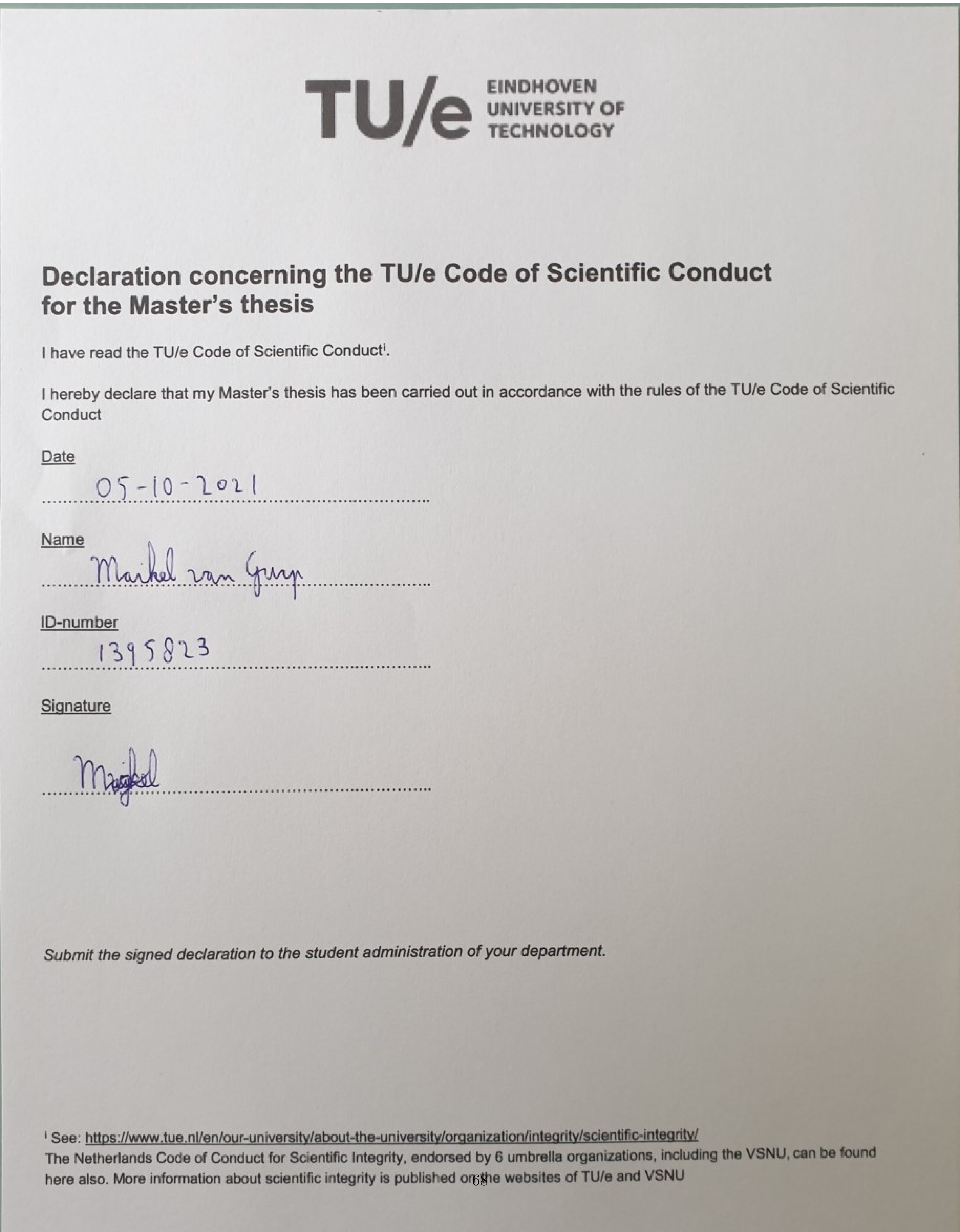

TU/e EINDHOVEN UNIVERSITY OF TECHNOLOGY

Declaration concerning the TU/e Code of Scientific Conduct for the Master's thesis

I have read the TU/e Code of Scientific Conduct[i].

I hereby declare that my Master's thesis has been carried out in accordance with the rules of the TU/e Code of Scientific Conduct

Date

05-10-2021

Name

Maikel van Gurp

ID-number

1395823

Signature

Submit the signed declaration to the student administration of your department.

---

[i] See: https://www.tue.nl/en/our-university/about-the-university/organization/integrity/scientific-integrity/
The Netherlands Code of Conduct for Scientific Integrity, endorsed by 6 umbrella organizations, including the VSNU, can be found here also. More information about scientific integrity is published on the websites of TU/e and VSNU